UNIVERSITY OF OKLAHOMA

GRADUATE COLLEGE

OBSERVING SYSTEM SIMULATION EXPERIMENTS ON ASSIMILATION OF MULTISTATIC PASSIVE RADAR NETWORK OBSERVATIONS INTO THE WARN-ON FORECAST SYSTEM TO IMPROVE SHORT-TERM PREDICTION OF THUNDERSTORM HAZARDS

A THESIS

SUBMITTED TO THE GRADUATE FACULTY

in partial fulfillment of the requirements for the

Degree of

MASTER OF SCIENCE IN METEOROLOGY

By

ANGELA JEANE MOSE
Norman, Oklahoma
2022

OBSERVING SYSTEM SIMULATION EXPERIMENTS ON ASSIMILATION OF MULTISTATIC PASSIVE RADAR NETWORK OBSERVATIONS INTO THE WARN-ON FORECAST SYSTEM TO IMPROVE SHORT-TERM PREDICTION OF THUNDERSTORM HAZARDS

A THESIS APPROVED FOR THE
SCHOOL OF METEOROLOGY

BY THE COMMITTEE CONSISTING OF

Dr. Patrick Skinner, Chair

Dr. David Bodine

Dr. Robert Palmer

Dr. Xuguang Wang

Acknowledgements

I want to send a huge thank you to my advisor, Pat Skinner, for his constant support and understanding throughout this entire project. I would not have made it to this point without his help. Additionally, I want to thank Kent Knopfmeier for taking time to help debug while running the Warn-On Forecast System for the experiments. My thanks also extends to Nicholas Cooper for helping me finally understand how to loop code, rather than running the same code 4,000 times. Finally, none of this would have been possible with the love and support from my family and friends, as well as the support from my colleagues and mentors at NWS Rapid City. The past two and a half years were tough, but I was able to keep at it with the support from everyone listed above.

Funding for this research was provided by the NOAA/Office of Oceanic and Atmospheric Research under NOAA–University of Oklahoma Cooperative Agreement NA21OAR4320204, U.S. Department of Commerce, the CIWRO Director Discretionary Research Fund, and the Warn-on-Forecast project.

Table of Contents

Acknowledgements **iv**

List Of Tables **vii**

List Of Figures **viii**

Abstract **xviii**

1 Introduction **1**

2 Background **3**
2.1 The Warn-On Forecast System . . . 3
2.2 Bistatic Receivers . . . 12
2.3 Observing System Simulation Experiments . . . 16

3 Event Background **19**

4 Experimental Design **28**
4.1 Truth Run . . . 28
4.2 Experiments . . . 34
4.2.1 Multistatic Experiment . . . 37
4.2.2 WSR-88D Only Experiment . . . 41

5 Data and Analysis **42**
5.1 Assimilated Data . . . 42
5.2 Analysis Plans and Data Issues . . . 48
5.3 Multistatic vs Truth Run . . . 53
5.3.1 Reflectivity Analysis . . . 53
5.3.1.1 Ensemble Analyses . . . 53
5.3.1.2 Ensemble Forecasts . . . 70
5.3.2 Max Vertical Velocity Analysis . . . 85
5.3.2.1 Ensemble Analyses . . . 85
5.3.2.2 Ensemble Forecasts . . . 99
5.4 Multistatic Density vs WSR-88D Only . . . 106
5.4.1 Reflectivity Analysis . . . 106
5.4.1.1 Ensemble Analyses . . . 106
5.4.1.2 Ensemble Forecasts . . . 119

5.4.2 Max Vertical Velocity Analysis 137
5.4.2.1 Ensemble Analyses 137
5.4.2.2 Ensemble Forecasts 149
5.5 Probability Analysis 155

6 Discussion **167**

7 Conclusion **175**

Reference List **181**

List Of Tables

5.1 Ensemble analyses correlation coefficients for the Multistatic vs Truth Run reflectivity. WoFS members are labeled in the left-most column. . 55
5.2 Ensemble analyses r^2 values for the Multistatic vs Truth Run reflectivity. WoFS members are labeled in the left-most column. 56
5.3 Member average corrrelation coefficients and r^2 values for all ensemble analyses of the Multistatic vs Truth Run reflectivity. WoFS members are labeled in the left-most column, followed by correlation coefficients, and then r^2 values. 57

List Of Figures

2.1 Planetary boundary layer (PBL), shortwave radiation, and longwave radiation schemes for each of the 18 WoFS members (adapted from Skinner et al. (2018), their Table 1). PBL options are the Yonsei University (YSU), Mellor-Yamada-Janjić (MYJ), and Mellor-Yamada-Nakanashi-Niino (MYNN) schemes. These are paired with the Dudhia, Rapid Radiative Transfer Model (RRTM) or the Rapid Radiative Transfer Model for GCMs (RRTMG) radiation parameterization schemes for shortwave and longwave radiation. 4

2.2 This figure (adapated from Snyder and Zhang (2003)) is a visual representation of the update step within the Analysis Step of the EnKF. a) The black dots are forecast values of radial velocity and vertical velocity for an ensemble comprised of 50 members. The thin arrows on the x- and y-axes represent the ensemble mean value for radial velocity and vertical velocity, which is about 9 ms^{-1}. The thicker black arrow along the y-axis represents a example radial velocity value of 14 ms^{-1}, with the accompanying curve showing the uncertainty in the observation. b) The black dots represent the updated ensemble values after considering the 14 ms^{-1} example radial velocity value. Grey dots are from the forecast in a). 7

2.3 Simplified schematic of the cyclic process utilized by the EnKF. The Analysis Step and the Forecast Step are labeled on the figure. 8

2.4 Schematic (adapted from Skinner et al. (2018)) displaying how WoFS is run and when data assimilation occurs. The frequency and length of top of the hour and half hour forecasts are shown. For this specific experiment, WoFS was run out to 0300 UTC. 10

2.5 Adapted from Guerra et al. (2022), showing the probability of detection for WoFS thunderstorm objects binned by the number of DA cycles at forecast initialization. The blue line shows POD for thunderstorms with 30 minutes of Relative Object Age (ROA), or two DA cycles prior to forecast initialization. The yellow line shows the POD for thunderstorms with 30-60 minute ROA, or two-four DA cycles. The green line shows POD of thunderstorms with more than 60 minutes ROA, or more than four DA cycles. The shaded intervals around each line is the 90% confidence interval. 13

2.6 Picture of a bistatic receiver from Byrd et al. (2019). This specific system is mounted on the roof of the Radar Innovation Laboratory at the University of Oklahoma in Norman, Oklahoma. 14

2.7 A simplified outline of the typical process used in creating OSSEs. The first three steps are related to conducting an idealized simulation, with the remaining steps being specific to OSSE creation. 17

3.1 Storm reports from the Storm Prediction Center for 7 May 2020. 20
3.2 Reflectivity swath of the 7 May 2020 hail-producing supercell over northern Texas. This image was created in GR2Analyst Version 3, using the 0.9° base reflectivity from KFDR. The swath was generated from 2100 UTC on 7 May until 0200 UTC on 8 May. Images were generated for every 2-3 volume scans, which was about every 10-15 minutes. 21
3.3 Enhanced Risk issued by the Storm Prediction Center at 2000 UTC on 7 May 2020. 22
3.4 A reference of the Oklahoma and Texas counties. The bold, yellow counties are those directly impacted by the 7 May 2020 supercell. NWS radar identifiers are in purple with purple dots at their locations. The selected radar, KFDR, is indicated with a red diamond. Image generated with GR2Analyst Version 3. 23
3.5 Ensemble, grid-scale probability of composite reflectivity being >40 dBZ for the 2000 UTC WoFS forecast on 7 May 2020. The swath of probabilities in northern Texas depict the forecast track of the supercell. This image was taken from the WoFS viewer page. 24
3.6 As in Figure 3.5, but for the 2100 UTC forecast on 7 May 2020. This image was taken from the WoFS viewer page. 25
3.7 As in Figure 3.5, but for the 2200 UTC forecast on 7 May 2020. This image was taken from the WoFS viewer page. 26

4.1 The nested grids used to downscale and create the Truth Run is shown. The thin, black line shows the 3-km grid, which is the same as the WoFS run for 7 May 2020. The thick black line shows the 1.5-km domain, and the thick purple line shows the 250-m truth run domain. 29
4.2 Reflectivity comparison for (a) the Truth Run at 2320 UTC and (b) the 2000 UTC WoFS Member 12 forecast valid at 2320 UTC. Reflectivity in dBZ. 31
4.3 As in Fig. 4.2, but for 0000 UTC on 8 May 2020. 32
4.4 Layout for the receivers for the Multistatic experiment. North/South distance from the transmitter is on the y-axis and East/West distance from the transmitter is on the x-axis. The transmitter is located at (0,0) along with a receiver, which creates the emulated WSR-88D. Five other receivers are placed around the transmitter at (-40, 0), (40,0), (-50,-35), (0,-40), and (50,-35) to obtain different viewing angles of the storm. . . 35

4.5 Truth Run reflectivity (dBZ) contour filled with the locations of the multistatic network receivers. Receivers are shown as blue stars and the transmitter is the purple diamond. Time steps chosen were (a) 2215 UTC, (b) 2230 UTC, (c) 2245 UTC, and (d) 2300 UTC. 39
4.6 Truth Run reflectivity (dBZ) contour filled with the locations of the multistatic network receivers. Receivers are shown as blue stars and the transmitter is the purple diamond. Time steps chosen were (a) 2330 UTC, (b) 0000 UTC, (c) 0030 UTC, and (d) 0100 UTC. 40

5.1 2230 UTC assimilated 0.5° radial velocity (ms^{-1}) observations for (a) transmitting radar, and assimilated 0.5° bistatic velocity (ms^{-1}) for (b) receiver 2, (c) receiver 3, (d) receiver 4, (e) receiver 5, and (f) receiver 6. Receiver locations are represented by blue stars, while the transmitter location is represented by the purple diamond. Images are zoomed in for detail. 45
5.2 2230 UTC assimilated reflectivity observations in dBZ at 1 km. Transmitter location shown with the purple diamond. 46
5.3 2230 UTC Truth Run reflectivity in dBZ. 47
5.4 2200 UTC assimilated reflectivity observations in dBZ for all elevations. Transmitter location shown with the purple diamond. 51
5.5 As in Figure 5.4, but only for the 1 km elevation. 52
5.6 Correlation Coefficients for each member for the ensemble analyses from 2215 (blue), 2230 (orange), 2245 (purple), 2300 (green), and 2330 (yellow) UTC. 54
5.7 Member average correlation coefficient for ensemble analyses of the Multistatic vs Truth Run reflectivity for all initializations. 58
5.8 (a) Interpolated Truth Run reflectivity (dBZ) at 2215 UTC on 7 May 2020. For the 2215 UTC ensemble analysis, the best performing member (b) Member 3, CC of 0.754, the median performing member (c) Member 15, CC of 0.534 (median: 0.532), and the worst performing member (d) Member 2, CC of 0.082 reflectivity is plotted. 59
5.9 (a) Interpolated Truth Run reflectivity (dBZ) at 2230 UTC on 7 May 2020. For the 2230 UTC ensemble analysis, the best performing member (b) Member 5, CC of 0.967, the median performing member (c) Member 16, CC of 0.9413 (median: 0.9418), and the worst performing member (d) Member 4, CC of 0.918 reflectivity is plotted. 61
5.10 (a) Interpolated Truth Run reflectivity (dBZ) at 2245 UTC on 7 May 2020. For the 2245 UTC ensemble analysis, the best performing member (b) Member 16, CC of 0.888, the median performing member (c) Member 14, CC of 0.845 (median: 0.849), and the worst performing member (d) Member 2, CC of 0.785 reflectivity is plotted. 63

5.11 2245 UTC ensemble analyses Truth Run reflectivity minus Multistatic member reflectivity for the 2 best performing members: (a) Member 16, CC of 0.888 and (b) Member 9, CC of 0.880, as well as the 2 worst performing members: (c) Member 10, CC of 0.821 and (d) Member 2, CC of 0.785. All reflectivity differences are in dBZ. 64
5.12 (a) Interpolated Truth Run reflectivity (dBZ) at 2300 UTC on 7 May 2020. For the 2300 UTC ensemble analysis, the best performing member (b) Member 17, CC of 0.984, the median performing member (c) Member 15, CC of 0.963 (median: 0.962), and the worst performing member (d) Member 2, CC of 0.306 reflectivity is plotted. 66
5.13 2300 UTC ensemble analyses Truth Run reflectivity minus Multistatic member reflectivity for the 2 best performing members: (a) Member 17, CC of 0.984 and (b) Member 3, CC of 0.978, as well as the 2 worst performing members: (c) Member 14, CC of 0.902 and (d) Member 2, CC of 0.306. All reflectivity differences are in dBZ. 67
5.14 (a) Interpolated Truth Run reflectivity (dBZ) at 2330 UTC on 7 May 2020. For the 2330 UTC ensemble analysis, the best performing member (b) Member 1, CC of 0.975, the median performing member (c) Member 4, CC of 0.923 (median: 0.929), and the worst performing member (d) Member 9, CC of 0.367 reflectivity is plotted. 69
5.15 Average correlation coefficient for each member for each forecast: 2200 (blue), 2215 (orange), 2230 (purple), 2245 (green), 2300 (yellow), and 2330 UTC (red). 71
5.16 (a) Interpolated Truth Run reflectivity (dBZ) at 2200 UTC on 7 May 2020. For the 2200 UTC ensemble analysis, the best performing member (b) Member 11, CC of 0.694, the average performing member (c) Member 14, CC of 0.479 (average: 0.466), and the worst performing member (d) Member 2, CC of 0.053 reflectivity is plotted. 72
5.17 (a) Interpolated Truth Run reflectivity (dBZ) at 0200 UTC on 8 May 2020. For the 2200 UTC ensemble forecast at 0200 UTC, an accurate analysis of the storm in (b) Member 14, an example of the line of storms in (c) Member 17, and an example of a member without a storm in (d) Member 7 is plotted. 73
5.18 (a) Interpolated Truth Run reflectivity (dBZ) at 2245 UTC on 7 May 2020. For the 2215 UTC ensemble forecast at 2245 UTC, the best performing member (b) Member 13, CC of 0.787, the median performing member (c) Member 16, CC of 0.624 (median: 0.618), and the worst performing member (d) Member 2, CC of -0.261 reflectivity is plotted. . 75
5.19 (a) Interpolated Truth Run reflectivity (dBZ) at 0130 UTC on 7 May 2020. For the 2215 UTC ensemble forecast at 0130 UTC, the best performing member (b) Member 9, CC of 0.457, the median performing member (c) Member 10, CC of -0.034 (median: -0.032), and the worst performing member (d) Member 8, CC of -0.026 reflectivity is plotted. . 76

5.20 (a) Interpolated Truth Run reflectivity (dBZ) at 2330 UTC on 7 May 2020. For the 2230 UTC ensemble forecast at 2330 UTC, the best performing member (b) Member 5, CC of 0.461, a less accurate member that still maintains the left-mover (c) Member 14, CC of 0.020, and a less accurate member that dissipates the left-mover completely (d) Member 6, CC of -0.354 reflectivity is plotted. 78
5.21 (a) Interpolated Truth Run reflectivity (dBZ) at 2330 UTC on 7 May 2020. For the 2245 UTC ensemble forecast at 2330 UTC, the best looking member (b) Member 6, CC of 0.656, a less accurate member that barely maintains the left-mover (c) Member 10, CC of -0.176, and a member that does not accurately predict the Truth Run (d) Member 2, CC of -0.027 reflectivity is plotted. 80
5.22 (a) Interpolated Truth Run reflectivity (dBZ) at 2330 UTC on 7 May 2020. For the 2300 UTC ensemble forecast at 2330 UTC, the best performing member (b) Member 1, CC of 0.952, the median performing member (c) Member 11, CC of 0.772 (median: 0.761), and the worst performing member (d) Member 9, CC of 0.318 reflectivity is plotted. . 82
5.23 (a) Interpolated Truth Run reflectivity (dBZ) at 0000 UTC on 8 May 2020. For the 2330 UTC ensemble forecast at 0000 UTC, the best performing member (b) Member 16, CC of 0.777, the median performing member (c) Member 11, CC of 0.114 (median: 0.111), and the worst performing member (d) Member 2, CC of 0.018 reflectivity is plotted. . 84
5.24 Correlation Coefficients for each member for the ensemble analyses from 2215 (blue), 2230 (orange), 2245 (purple), 2300 (green), and 2330 (yellow) UTC. 87
5.25 (a) Interpolated Truth Run MVV (ms^{-1}) at 2215 UTC on 7 May 2020. For the 2215 UTC ensemble analysis, the best performing member (b) Member 7, CC of 0.405, the median performing member (c) Member 4, CC of -0.057 (median: -0.041), and the worst performing member (d) Member 11, CC of 0.010 MVV is plotted. 89
5.26 (a) Interpolated Truth Run MVV (ms^{-1}) at 2230 UTC on 7 May 2020. For the 2230 UTC ensemble analysis, the best performing member (b) Member 18, CC of -0.543, the median performing member (c) Member 13, CC of 0.112 (median: 0.116), and the worst performing member (d) Member 4, CC of 0.018 MVV is plotted. 91
5.27 (a) Interpolated Truth Run MVV (ms^{-1}) at 2245 UTC on 7 May 2020. For the 2245 UTC ensemble analysis, the best performing member (b) Member 8, CC of 0.536, the median performing member (c) Member 7, CC of 0.282 (median: 0.284), and the worst performing member (d) Member 13, CC of -0.009 MVV is plotted. 93

5.28 (a) Interpolated Truth Run MVV (ms^{-1}) at 2300 UTC on 7 May 2020. For the 2300 UTC ensemble analysis, the best performing member (b) Member 2, CC of 0.604, the median performing member (c) Member 14, CC of 0.227 (median: 0.229), and the worst performing member (d) Member 1, CC of 0.018 MVV is plotted. 95
5.29 2300 UTC Truth Run MVV minus the 2300 UTC ensemble analysis Multistatic MVV for (a) Member 2 and (b) Member 1. All differences are in ms^{-1}. 97
5.30 (a) Interpolated Truth Run MVV (ms^{-1}) at 2330 UTC on 7 May 2020. For the 2330 UTC ensemble analysis, the best performing member (b) Member 7, CC of 0.804, the median performing member (c) Member 17, CC of -0.019 (median: -0.033), and the worst performing member (d) Member 6, CC of -0.009 MVV is plotted. 98
5.31 Average correlation coefficient for each member for each forecast: 2200 (blue), 2215 (orange), 2230 (purple), 2245 (green), 2300 (yellow), and 2330 UTC (red). 100
5.32 (a) Interpolated Truth Run MVV (ms^{-1}) at 0000 UTC on 7 May 2020. MVV is plotted for the 2215 UTC ensemble forecast at 0000 UTC for (b) Member 5 with a southern displacement, (c) Member 11 with a southern displacement, and (d) Member 17 with a southern displacement. 101
5.33 (a) Interpolated Truth Run MVV (ms^{-1}) at 0000 UTC on 7 May 2020. MVV is plotted for the 2230 UTC ensemble forecast at 0000 UTC for (b) Member 4 with a southwestern displacement, (c) Member 11 with a southern displacement, and (d) Member 17 with a southwestern displacement. 102
5.34 (a) Interpolated Truth Run MVV (ms^{-1}) at 0000 UTC on 7 May 2020. MVV is plotted for the 2300 UTC ensemble forecast at 0000 UTC for (b) Member 2 with a southeastern displacement, (c) Member 12 with a southern displacement, and (d) Member 15 with a southern displacement. 104
5.35 (a) Interpolated Truth Run MVV (ms^{-1}) at 0000 UTC on 7 May 2020. MVV is plotted for the 2330 UTC ensemble forecast at 0000 UTC for (b) Member 1 with a southeastern displacement, (c) Member 13 with a southeastern displacement, and (d) Member 18 with a southeastern displacement. 105
5.36 Multistatic vs WSR-88D Only correlation coefficient for each member for the ensemble analyses of the 2200 (red), 2215 (blue), 2230 (orange), 2245 (purple), 2300 (green), and 2330 UTC (yellow) forecast runs. . . . 107
5.37 (a) Multistatic reflectivity (dBZ) for the highest correlation member, Member 6, (b) Multistatic reflectivity for the lowest correlation member, Member 17, (c) WSR-88D Only reflectivity for the highest correlation member, Member 6, and (d) WSR-88D Only Reflectivity for the lowest correlation member, Member 17. 109

5.38 (a) Multistatic reflectivity (dBZ) for the highest correlation member, Member 6, (b) Multistatic reflectivity for a representative member, Member 5, (c) WSR-88D Only reflectivity for the highest correlation member, Member 6, and (d) WSR-88D Only Reflectivity for a representative member, Member 5. 111
5.39 (a) Multistatic reflectivity (dBZ) for the highest correlation member, Member 2, (b) Multistatic reflectivity for the lowest correlation member, Member 13, (c) WSR-88D Only reflectivity for the highest correlation member, Member 2, and (d) WSR-88D Only Reflectivity for the lowest correlation member, Member 13. 113
5.40 (a) Multistatic reflectivity (dBZ) for the highest correlation member, Member 2, (b) Multistatic reflectivity for the lowest correlation member, Member 14, (c) WSR-88D Only reflectivity for the highest correlation member, Member 2, and (d) WSR-88D Only Reflectivity for the lowest correlation member, Member 14. 115
5.41 2300 UTC ensemble analysis correlation coefficient for the Multistatic vs Truth Run (purple) experiment plotted against the WSR-88D Only vs Truth Run (blue) ensemble analysis correlation coefficient. The correlation value above the bars is for the Multistatic vs Truth Run experiment and the correlation values closest to the x-axis are for the WSR-88D Only vs Truth Run experiment. Multistatic average correlation coefficient is 0.925 and the WSR-88D Only average correlation coefficient is 0.923 for this analysis. 117
5.42 (a) Multistatic reflectivity (dBZ) for the highest correlation member, Member 9, (b) Multistatic reflectivity for the lowest correlation member, Member 11, (c) WSR-88D Only reflectivity for the highest correlation member, Member 9, and (d) WSR-88D Only Reflectivity for the lowest correlation member, Member 11. 118
5.43 Average correlation coefficient for each member for each forecast: 2200 (blue), 2215 (orange), 2230 (purple), 2245 (green), 2300 (yellow), and 2330 UTC (red). 121
5.44 Member average correlation coefficient for the Multistatic vs Truth Run (purple) experiment plotted against the WSR-88D Only vs Truth Run (blue) member average correlation coefficient for the 2215 UTC forecast. The average value is plotted nearest the top of the bar for the Multistatic vs Truth Run experiment and nearest the x-axis for the WSR-88D Only vs Truth Run experiment. 122
5.45 Interpolated Truth Run reflectivity (dBZ) at (a) 0010 UTC and (b) 0200 UTC. 123

5.46 Reflectivity difference (dBZ) for the 2215 UTC forecast at 0010 UTC for (a) Truth Run minus Multistatic reflectivity Member 14 and (b) Truth Run minus WSR-88D Only Member 14 is plotted. Reflectivity difference (dBZ) for the 2215 UTC forecast at 0200 UTC for (c) Truth Run minus Multistatic reflectivity Member 7 and (d) Truth Run minus WSR-88D Only reflectivity Member 7 is plotted. Storms are cut off due to reaching the Truth Run boundary, as shown in Figure 4.1. 124
5.47 Reflectivity (dBZ) for (a) Multistatic Member 14 at 0010 UTC, (b) Multistatic Member 7 at 0200 UTC, (c) WSR-88D Only Member 14 at 0010 UTC, and (d) WSR-88D Only Member 7 at 0200 UTC is plotted. Storms are cut off due to reaching the Truth Run boundary, as shown in Figure 4.1. 125
5.48 Interpolated Truth Run reflectivity (dBZ) at (a) 2315 UTC and (b) 0000 UTC. 127
5.49 Reflectivity (dBZ) for (a) Multistatic Member 6 at 2315 UTC, (b) Multistatic Member 14 at 0000 UTC, (c) WSR-88D Only Member 6 at 2315 UTC, and (d) WSR-88D Only Member 14 at 0000 UTC is plotted. . . 128
5.50 2345 UTC Interpolated Truth Run reflectivity in dBZ. 130
5.51 Reflectivity (dBZ) for (a) Multistatic Member 13 at 2315 UTC, (b) Multistatic Member 5 at 2345 UTC, (c) WSR-88D Only Member 13 at 2315 UTC, and (d) WSR-88D Only Member 5 at 2345 UTC is plotted. 131
5.52 Multistatic minus WSR-88D Only reflectivity for (a) Member 13 at 2315 UTC and (b) Member 5 at 2345 UTC. All reflectivity differences are in dBZ. 133
5.53 Member average correlation coefficient for the Multistatic vs Truth Run (purple) experiment plotted against the WSR-88D Only vs Truth Run (blue) member average correlation coefficient for the 2300 UTC forecast. The average value is plotted nearest the top of the bar for the Multistatic vs Truth Run experiment and nearest the x-axis for the WSR-88D Only vs Truth Run experiment. 134
5.54 Reflectivity (dBZ) at 0100 UTC for (a) Multistatic Member 17, (b) Multistatic Member 11, (c) WSR-88D Only Member 17, and (d) WSR-88D Only Member 11 is plotted. 136
5.55 Average correlation coefficient for each member for each forecast: 2200 (blue), 2215 (orange), 2230 (purple), 2245 (green), 2300 (yellow), and 2330 UTC (red). 138
5.56 Correlation coefficients for each WSR-88D Only member for the ensemble analyses from 2215 (blue), 2230 (orange), 2245 (purple), 2300 (green), and 2330 (yellow) UTC. 139

5.57 (a) Interpolated Truth Run MVV (ms^{-1}) at 2215 UTC on 7 May 2020. For the 2215 UTC WSR-88D Only ensemble analysis, the best performing member (b) Member 7, CC of 0.395, the median performing member (c) Member 4, CC of -0.072 (median: -0.056), and the worst performing member (d) Member 11, CC of -0.010 MVV is plotted. 140
5.58 (a) Interpolated Truth Run MVV (ms^{-1}) at 2230 UTC on 7 May 2020. For the 2230 UTC WSR-88D Only ensemble analysis, the best performing member (b) Member 18, CC of -0.539, the median performing member (c) Member 13, CC of 0.156 (median: 0.137), and the worst performing member (d) Member 4, CC of 0.038 MVV is plotted. 142
5.59 (a) Interpolated Truth Run MVV (ms^{-1}) at 2245 UTC on 7 May 2020. For the 2245 UTC WSR-88D Only ensemble analysis for (b) Member 8, CC of 0.528, (c) Member 7, CC of 0.285 (median: 0.302), and (d) Member 13, CC of 0.106 MVV is plotted. 144
5.60 (a) Interpolated Truth Run MVV (ms^{-1}) at 2300 UTC on 7 May 2020. For the 2300 UTC WSR-88D Only ensemble analysis for (b) Member 2, CC of 0.616, (c) Member 14, CC of 0.281 (median: 0.283), and (d) Member 1, CC of 0.069 MVV is plotted. 146
5.61 (a) Interpolated Truth Run MVV (ms^{-1}) at 2330 UTC on 7 May 2020. For the 2330 UTC WSR-88D Only ensemble analysis for (b) Member 7, CC of 0.789, (c) Member 17, CC of -0.055 (median: -0.050), and (d) Member 6, CC of 0.067 MVV is plotted. 148
5.62 (a) Interpolated Truth Run MVV (ms^{-1}) at 0000 UTC on 7 May 2020. MVV is plotted for the 2215 UTC ensemble forecast at 0000 UTC for the WSR-88D Only experiment (b) Member 5 with a southern displacement, (c) Member 11 with a southern displacement, and (d) Member 17 with a southern displacement. 150
5.63 (a) Interpolated Truth Run MVV (ms^{-1}) at 0000 UTC on 7 May 2020. MVV is plotted for the 2230 UTC ensemble forecast at 0000 UTC for the WSR-88D Only experiment (b) Member 4 with a southern displacement, (c) Member 11 with a southern displacement, and (d) Member 17 with a southern displacement. 151
5.64 (a) Interpolated Truth Run MVV (ms^{-1}) at 0000 UTC on 7 May 2020. MVV is plotted for the 2300 UTC ensemble forecast at 0000 UTC for the WSR-88D Only experiment (b) Member 2 with a southeastern displacement, (c) Member 12 with a southeastern displacement, and (d) Member 15 with a southeastern displacement. 153
5.65 (a) Interpolated Truth Run MVV (ms^{-1}) at 0000 UTC on 7 May 2020. MVV is plotted for the 2330 UTC ensemble forecast at 0000 UTC for (b) Member 1 with a southeastern displacement, (c) Member 13 with a eastern displacement, and (d) Member 18 with a southeastern displacement. 154

5.66 Probability of 2 to 5 km updraft helicity exceeding 60 m^2s^{-2} using a 9 km diameter neighborhood for the 2200 UTC forecast for (a) the Multistatic experiment and (b) the WSR-88D Only experiment. The 0200 UTC time step is used to show the probability swath for the entire forecast, corresponding to the Truth Run time. 156
5.67 As in Figure 5.66, but for the 2215 UTC forecast. 158
5.68 As in Figure 5.66, but for the 2230 UTC forecast. 160
5.69 As in Figure 5.66, but for the 2245 UTC forecast. 162
5.70 As in Figure 5.67, but for the 2300 UTC forecast. 164
5.71 As in Figure 5.66, but for the 2330 UTC forecast. 166

Abstract

The Warn-on-Forecast System (WoFS) assimilates radar and satellite observations to produce initial conditions for short-term forecasts of individual convective storms. The accuracy of the WoFS analysis is a function of the quality and number of observations assimilated. For example, Doppler radar velocity data provide useful information on the observed wind field; however, it only provides velocity observations radial to the radar beam. Recently a network of low-cost multistatic, passive radar receivers have been developed for use with the WSR-88D network. The passive radar network allows for sampling of bistatic velocities across a wide region and provides a more accurate depiction of the three-dimensional wind field in and around thunderstorms as they initiate, mature, and dissipate. Assimilation of multistatic, passive radar network observations into WoFS has the potential to improve storm-scale analyses and short-term forecasts.

This study uses Observing System Simulation Experiments (OSSEs) to assess the implications of assimilating multistatic network observations into WoFS. An OSSE was designed for a non-tornadic, hail-producing supercell that impacted northern Texas on 7 May 2020. A truth run is generated by downscaling a single real-time WoFS member forecast to 250-m horizontal grid spacing. Multistatic network observations, using six passive receivers and an emulated WSR-88D, are then created from the truth run and assimilated into the remaining WoFS members to assess the impact of these observations on the quality of WoFS analyses and forecasts of the supercell, particularly early in the storm's life cycle. The multistatic network and the WSR-88D simulations are compared to the truth run via subjective comparisons and statistical methods. Preliminary analyses reveal minimal differences in forecast quality between the Multistatic experiment and the WSR-88D experiment; however, statistical results suggest that the WSR-88D simulation produces a slightly better forecast with higher correlation to the truth run.

Chapter 1

Introduction

Convection Allowing Models (CAMs) are beneficial to National Weather Service (NWS) forecasters across all forecast offices in the United States. However, many of these models are not run at sufficient times nor with sufficient temporal resolution for forecasting severe weather as it evolves. CAMs such as the High Resolution Rapid Refresh (HRRR; Dowell et al. (2022)) model are run every hour, for 12 hours, with data output every hour. This update rate is often insufficient for accurately forecasting convection as it initiates and matures. Over the past several years, development on a new type of CAM has been underway, one that updates more frequently with higher temporal resolution. The Warn-On Forecast System (WoFS) is a Convection Allow Ensemble (CAE) with 18 members. WoFS is typically run on severe weather days and produces 6-hour forecasts every half hour that output data every 5 minutes.

The goal of WoFS is to allow for a new paradigm of forecasting, changing the typical forecasting approach of warn-on detection to warn-on forecast (Stensrud et al. 2009, 2013). NWS forecasters currently warn storms based on tends in radar, satellite, and other forms of meteorological data. However, WoFS attempts to provide forecasters with short-term (0-6 hour) guidance that allows forecasters to better anticipate when and where severe weather will occur. If WoFS is able to accurately analyze ongoing storms, it is likely to provide an accurate short-term forecast of those storms (Guerra et al. 2022). Forecasters could then use WoFS guidance to issues warnings on the storm well before it reaches peak intensity and provide the public with increased lead time to

protect their livelihood and property. To do this, WoFS has many unique features that allow it to stand apart from other CAMs and CAEs, which will be discussed in the following sections. Some of these differences include assimilating current radar, satellite, surface observations, and other meteorological data every 15 minutes to continually update the first guess. However, it is important to note that WoFS is not perfect, and it does not perform well before there is a storm in the assimilated observations. These shortcomings need to be addressed before the reality of a warn-on forecast paradigm can be attained.

Chapter 2

Background

2.1 The Warn-On Forecast System

The Warn-On Forecast System (WoFS) is a rapidly-cycled, 18-member, storm-scale, convection allowing ensemble that aims to provide watch-to-warning guidance for National Weather Service (NWS) forecasters of convective weather threats (Wheatley et al. 2015; Jones et al. 2016). The overarching goal of WoFS is to improve the prediction of convective hazards during timescales between convective watches being issued and the first warnings. To do this, WoFS produces forecasts twice per hour that are run out to 3 or 6 hours (Wheatley et al. 2015; Jones et al. 2016). The frequency of WoFS forecasts provides rapid updates to NWS forecasters that can accurately depict the current state of the atmosphere, as well as how it may evolve over the next few hours (Guerra et al. 2022). WoFS produces forecasts with 3-km horizontal grid spacing that spans a 900x900 km domain. Additionally, WoFS uses 51 vertical levels between the surface and 10 hPa (Wheatley et al. 2015; Jones et al. 2016; Kerr et al. 2021). For each of the 18 WoFS members, a different combination of physical parameterization schemes for planetary boundary layer, shortwave radiation, and longwave radiation are used to add spread to the members. The combinations of physical parameterizations schemes for each WoFS member are shown in Figure 2.1.

In particular, to get the best representation of the current atmospheric state, Ensemble Kalman Filter (EnKF) techniques are frequently used for convective-scale radar

Member	PBL	Shortwave radiation	Longwave radiation
1	YSU	Dudhia	RRTM
2	YSU	RRTMG	RRTMG
3	MYJ	Dudhia	RRTM
4	MYJ	RRTMG	RRTMG
5	MYNN	Dudhia	RRTM
6	MYNN	RRTMG	RRTMG
7	YSU	Dudhia	RRTM
8	YSU	RRTMG	RRTMG
9	MYJ	Dudhia	RRTM
10	MYJ	RRTMG	RRTMG
11	MYNN	Dudhia	RRTM
12	MYNN	RRTMG	RRTMG
13	YSU	Dudhia	RRTM
14	YSU	RRTMG	RRTMG
15	MYJ	Dudhia	RRTM
16	MYJ	RRTMG	RRTMG
17	MYNN	Dudhia	RRTM
18	MYNN	RRTMG	RRTMG

Figure 2.1: Planetary boundary layer (PBL), shortwave radiation, and longwave radiation schemes for each of the 18 WoFS members (adapted from Skinner et al. (2018), their Table 1). PBL options are the Yonsei University (YSU), Mellor-Yamada-Janjić (MYJ), and Mellor-Yamada-Nakanashi-Niino (MYNN) schemes. These are paired with the Dudhia, Rapid Radiative Transfer Model (RRTM) or the Rapid Radiative Transfer Model for GCMs (RRTMG) radiation parameterization schemes for shortwave and longwave radiation.

assimilation, as they can assimilate Weather Surveillance Radar-1988 Doppler (WSR-88D) radar reflectivity and radial velocity, satellite cloud water path observations, automated surface observing station (ASOS) data, and mesonet data (when available) every 15 minutes, which is approximately four times more often than the High Resolution Rapid Refresh (HRRR) model and the High Resolution Rapid Refresh Data Assimilation System (HRRRDAS) (Wheatley et al. 2015; Jones et al. 2016; Kerr et al. 2021). The HRRRDAS is a 36-member, convection-allowing data assimilation system that provides initial and boundary conditions for WoFS. The hourly data assimilation (DA) is run over the continental United States (CONUS) and uses 3-km horizontal grid spacing (Dowell et al. 2022). More frequent DA in WoFS can create an accurate analysis, forecast, and estimate of uncertainty for individual convective storms. Using information from observations to accurately estimate storm-scale structures in the model initial conditions assists in the spin-up of convection if the storm is not presently resolved within the ensemble. It has been found that WoFS is likely to produce an accurate prediction of individual storms out to three hours of lead time if an accurate analysis is produced; however, predictions for storms that are not accurately analyzed is far less accurate (Guerra et al. 2022). Therefore, one of the best ways to improve WoFS quality is by expediting the spin-up of storms in WoFS by using more frequent DA, potentially more frequently than every 15 minutes (Guerra et al. 2022).

The high-frequency DA needed for WoFS is provided by an EnKF (Snyder and Zhang 2003; Houtekamer and Zhang 2016). A 36 member ensemble is used with an EnKF to produce the initial conditions for WoFS. The EnKF uses flow dependent, background error covariances provided by the ensemble with observations to update the ensemble mean towards the observations. WoFS uses the Gridpoint Statistical Interpolation software, as described in Kleist et al. (2009) and Jones et al. (2020) for assimilation. EnKF DA methods are relatively simple to implement and is a common

choice when assimilating observations onto a convection-allowing grid (e.g., Hitchcock et al. (2016); Snyder and Zhang (2003)) because it produces accurate analyses of the true state of convective storms (e.g., Snyder and Zhang (2003); Wheatley et al. (2015)).

There are two steps within the EnKF: The Analysis Step and the Forecast Step. During the Analysis Step, observations and radar data are processed serially. The ensemble mean from the previous forecast step is calculated and then updated according to observations and ensemble background error covariances. The difference of each member from the ensemble mean is used to update each member. These calculations create a new ensemble analysis, which represents the best estimate of the current atmospheric state and is used to initialize the next forecast step (Snyder and Zhang 2003).

To visualize the EnKF updating the ensemble mean towards the observations, it is helpful to look at Figure 2.2 (adapated from Snyder and Zhang (2003)). It is important to note that the updated ensemble has changed radial velocity observations and vertical velocity as well, indicating that the EnKF is spreading observed information to unobserved variables. Once the ensemble is updated, members are forecast forward until the next DA cycle, which is considered the Forecast Step (Snyder and Zhang 2003). Upon completion of the Forecast Step, the next DA cycle begins, and the Analysis Step starts again and follows the same process (Figure 2.3).

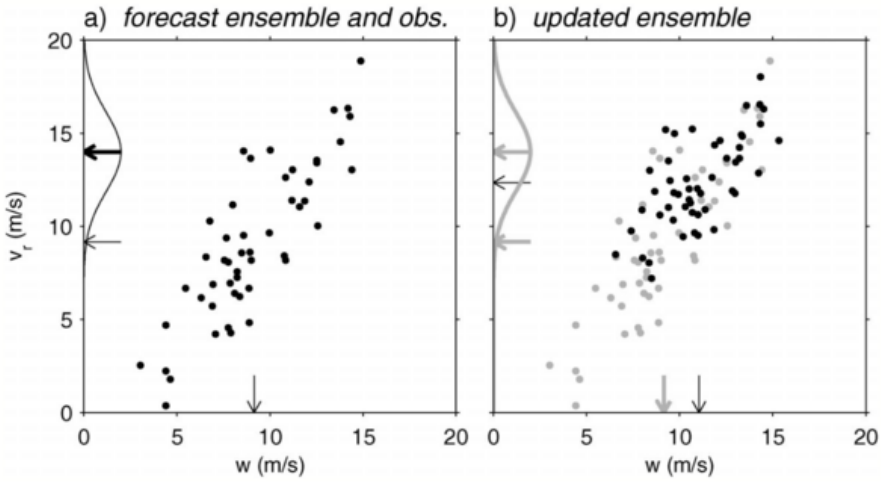

Figure 2.2: This figure (adapated from Snyder and Zhang (2003)) is a visual representation of the update step within the Analysis Step of the EnKF. a) The black dots are forecast values of radial velocity and vertical velocity for an ensemble comprised of 50 members. The thin arrows on the x- and y-axes represent the ensemble mean value for radial velocity and vertical velocity, which is about 9 ms^{-1}. The thicker black arrow along the y-axis represents a example radial velocity value of 14 ms^{-1}, with the accompanying curve showing the uncertainty in the observation. b) The black dots represent the updated ensemble values after considering the 14 ms^{-1} example radial velocity value. Grey dots are from the forecast in a).

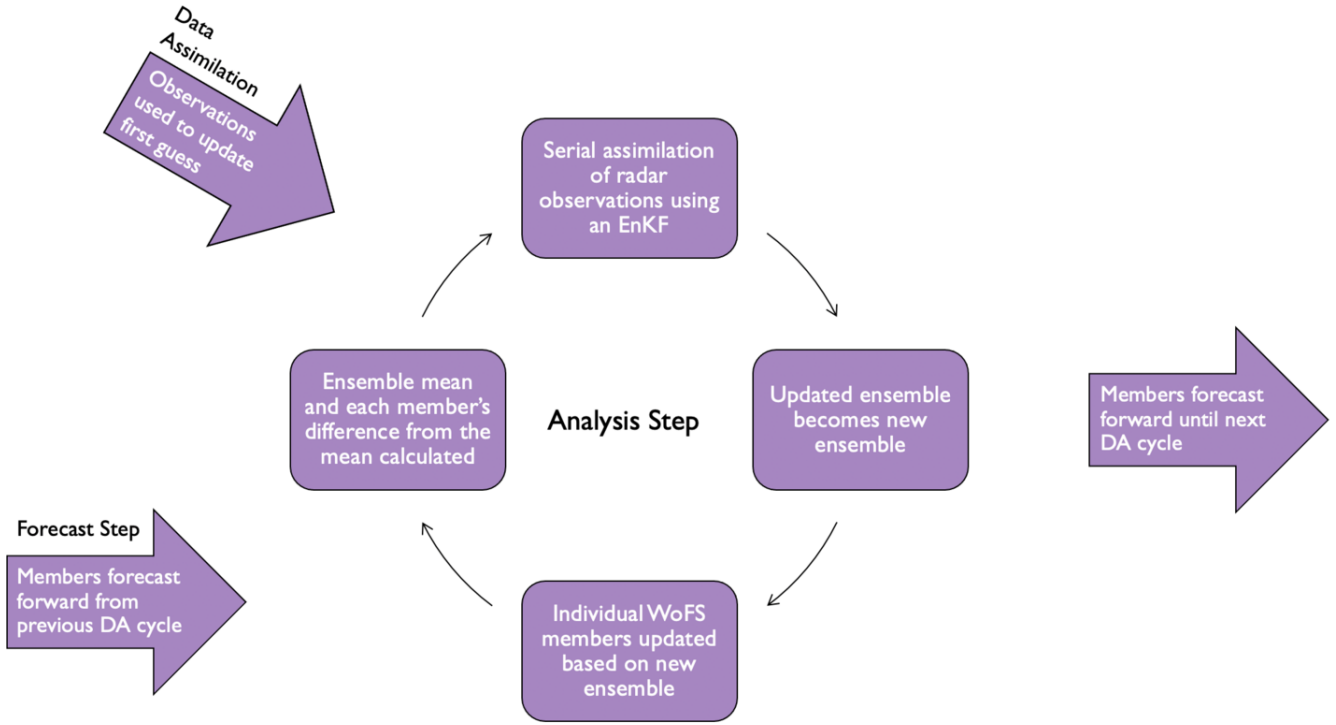

Figure 2.3: Simplified schematic of the cyclic process utilized by the EnKF. The Analysis Step and the Forecast Step are labeled on the figure.

The 1-hr forecast from the HRRRDAS is used as initial conditions (ICs) for the WoFS ensemble. ASOS data, satellite cloud water path observations, radar reflectivity and radial velocity, and mesonet data (if available) are assimilated using the EnKF and the ensemble analysis is used for forecast initialization at the top of each hour beginning after 5 data assimilation cycles (Figure 2.4). Forecasts at the top of the hour are run out 6 hours. While this forecast is running, observations and radar data continue to be assimilated every 15 minutes within the DA system, preparing for the next forecast initialization. In the DA system, observations are continually being used to update the ensemble towards the newest observations, which then produces the first guess for the next model run time. On the half hour, a second forecast is produced by the forecast system and runs out 3 hours. DA within the DA system continues to update the ensemble towards the observations every 15 minutes, then produces another first guess and forecast at the top of the hour. This process continues throughout the designated run period and produces a new first guess and forecast every 30 minutes. Each successive forecast has two additional DA cycles compared to the previous forecast, which helps WoFS better match the observations as time progresses. Resulting from continuous cycled DA, WoFS forecasts could be run every 15 minutes, which means only one additional DA cycle per each new run time. The updated ensemble one DA cycle after the previous model initialization would become the first guess for the 15-minute forecast.

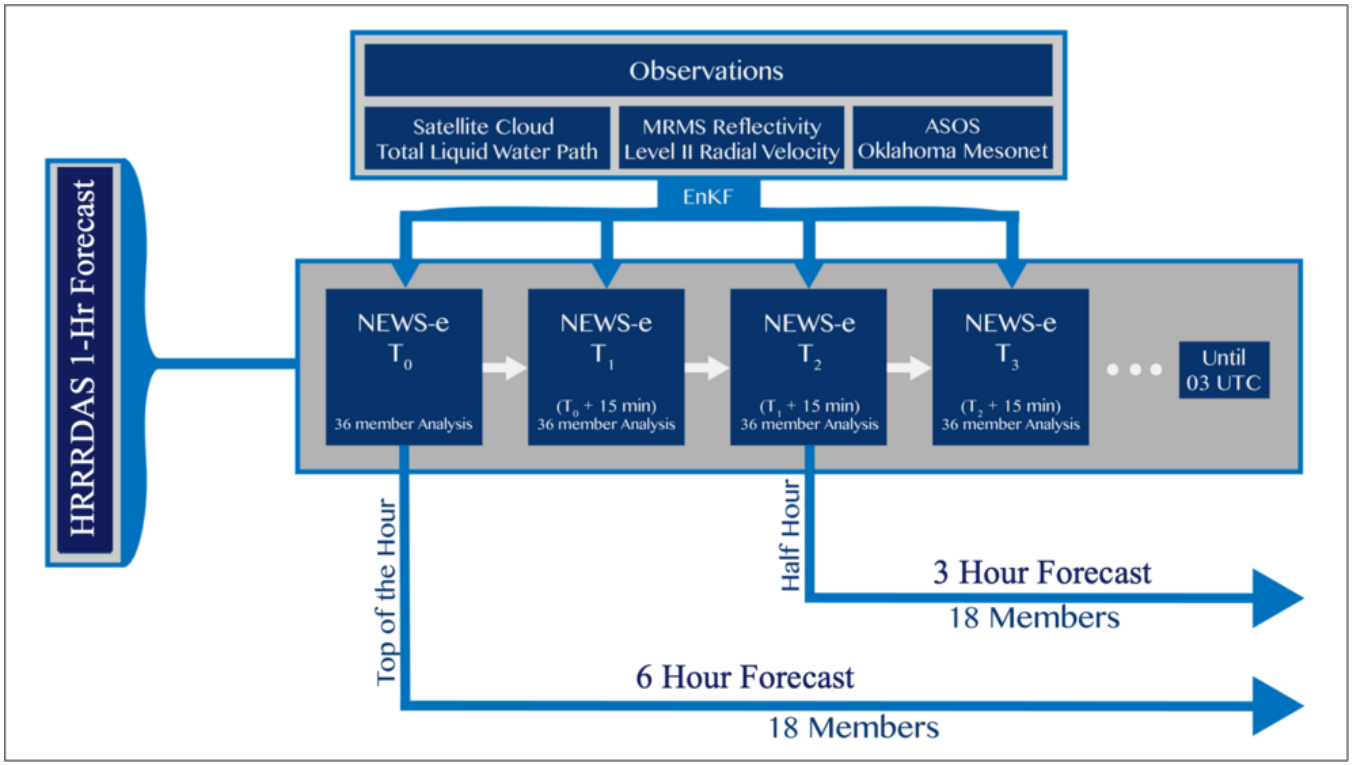

Figure 2.4: Schematic (adapted from Skinner et al. (2018)) displaying how WoFS is run and when data assimilation occurs. The frequency and length of top of the hour and half hour forecasts are shown. For this specific experiment, WoFS was run out to 0300 UTC.

While WoFS is capable of improving the prediction of storms and their associated hazards, it is not without fault. Namely, WoFS performs poorly before and around convective initiation (CI) and typically takes 4-6 assimilation cycles to produce an accurate ensemble analysis of a storm (Guerra et al. 2022). Wheatley et al. (2015) states that the basis of WoFS is assimilating radar data in order to accurately analyze ongoing storms. Therefore, it is logical that WoFS will not perform as well before CI due to the lack of radar observations available for assimilation. If WoFS can accurately predict the mesoscale environment, then it is able to produce accurate forecasts of individual storms once they are spun-up in the system through DA, which is shown by Guerra et al. (2022). Therefore, it is desirable to spin-up a storm in WoFS quicker. Stensrud et al. (2009) suggested that radar is a good way to accurately represent ongoing convection within a model, and Coniglio et al. (2016) found that radar DA is essential to improving the prediction of convection, assuming background features are resolved well. Stratman et al. (2020) found that more frequent DA cycles produce accurate analyses more quickly and accurate forecasts with longer lead-time. Guerra et al. (2022) found that probability of detection (POD) of thunderstorm objects increases with an increase of radar data DA cycles (Figure 2.5). There is a distinct increase in POD for lead-times out to 3 hours after four or more DA cycles, with forecast initialized after only two DA cycles producing a much lower POD. While POD is not the only factor to consider when looking at how well WoFS forecasts perform, it demonstrates that there is a direct relationship between ingesting more data and improved WoFS forecasts. Given this information, assimilating additional radar data around CI should enable WoFS to predict convection more accurately, sooner, and with longer lead-times. However, the amount of radar data available across the CONUS in real time is relatively static and it would be difficult to establish new WSR-88D sites with the intentions of receiving

and ingesting more data. Therefore, to get this additional radar data other methods must be considered.

2.2 Bistatic Receivers

One cost-effective solution to the problem of radar data available across the CONUS being static is using multiple, bistatic radar receiver systems in conjunction with a single transmitting WSR-88D (Figure 2.6). Bistatic receivers are passive, fixed-beam radar receivers that allow for multiple-look angles into storms of interest, all while being remotely located from a transmitting radar (Wurman et al. 1993; Wurman 1994; de Elía and Zawadzki 2001). Bistatic receivers are equipped with a small, wide field of view antenna that collects energy scattered into space. These systems are small and compact, consisting only of a fixed antenna, radio frequency front end, transceiver, small processing computer and a weather proofed low-noise amplifier (Byrd et al. 2019). When a radar transmits a pulse, the beam of energy interacts with the environment and scatters off hydrometeors within a storm. Some of this energy is returned to the transmitting radar, but the rest is scattered into space. Bistatic receivers detect the scattered energy from a different location and angle to the scatterer as the transmitting radar, which allows the bistatic velocity to be calculated. The retrieval of the three-dimensional wind field around a target storm is possible using a multiple-Doppler synthesis between the radial velocity measured by the transmitting radar and bistatic velocity (Wurman 1994). To obtain the three-dimensional wind field, the receivers must first be synchronized and cohered, specifically the time the pulse is received must be known to separate data into ranges. Cohering is needed to make Doppler estimations. Following synchronization, bistatic velocities are calculated and localized in Cartesian coordinates. Velocity data are filtered using the Signal-to-Noise Ratio and bistatic

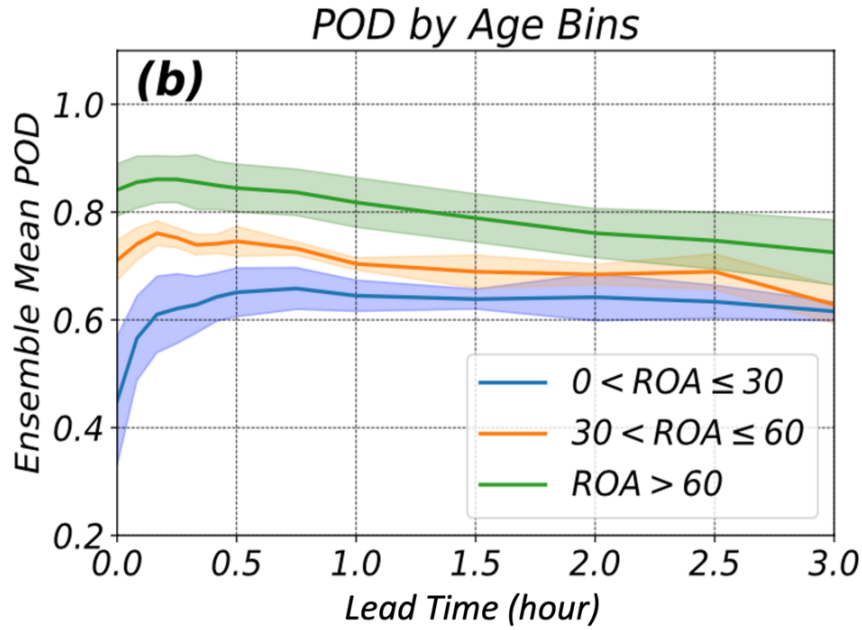

Figure 2.5: Adapted from Guerra et al. (2022), showing the probability of detection for WoFS thunderstorm objects binned by the number of DA cycles at forecast initialization. The blue line shows POD for thunderstorms with 30 minutes of Relative Object Age (ROA), or two DA cycles prior to forecast initialization. The yellow line shows the POD for thunderstorms with 30-60 minute ROA, or two-four DA cycles. The green line shows POD of thunderstorms with more than 60 minutes ROA, or more than four DA cycles. The shaded intervals around each line is the 90% confidence interval.

Figure 2.6: Picture of a bistatic receiver from Byrd et al. (2019). This specific system is mounted on the roof of the Radar Innovation Laboratory at the University of Oklahoma in Norman, Oklahoma.

angle before being interpolated onto a uniform grid. Once this process is completed, the three-dimensional wind-field retrievals can be produced (Byrd et al. 2019).

In previous versions of these receivers, frequency and timing coherence were achieved using GPS signals (Wurman et al. 1993). The GPS systems used in previous iterations were expensive, not flexible, and required hardward modifications to the transmitter. Recent work from Byrd et al. (2019) utilized direct-path signal monitoring that assumes line-of-sight and requires time-stamped pointing angle information from the transmitting radar, which is significantly cheaper than the previous GPS systems. All together, these systems cost around $7,000 to construct (Byrd et al. 2019). While $7,000 may

appear a significant cost, especially if several of these systems were built and implemented, these systems are about 0.2% of the cost of a WSR-88D, which was around $3.5 million in 1994 (Wurman 1994; Wurman et al. 1993). In addition to their low cost, bistatic receivers are useful in field campaigns, and they can be used in conjunction with almost any transmitting radar (Byrd et al. 2019).

Challenges do exist with bistatic systems, including sidelobes and low sensitivity (Byrd et al. 2019; de Elía and Zawadzki 2001; Emmerson 2022; Wurman 1994; Wurman et al. 1993). Bistatic receiver sidelobes are caused by radiation scattered by the main transmitting radar beam and its sidelobes arriving to the receiver simultaneously, with the highest contamination occurring along the baseline between the transmitting radar and the bistatic receiver (de Elía and Zawadzki 2001). These sidelobes are more intense than those associated with WSR-88Ds, and this issue is commonly noted across different bistatic systems (Byrd et al. 2019; de Elía and Zawadzki 2001; Wurman 1994; Wurman et al. 1993). One solution presnted to improve sidelobe contaimination is to add more receivers and create a larger Multistatic Radar Network (Wurman 1994); however, this may not actually work well. A Multistatic Radar Network consists of one transmitting radar and multiple bistatic receivers and can reduce the contamination of sidelobes (Wurman et al. 1993). The low sensitivity is not as impactful to the bistatic receiver observations since the primary goal of bistatic receivers is to measure Doppler velocity and not power (Emmerson 2022); however, returns in light precipitation are lost. Therefore, the radial velocity observations are able to be estimated with a Signal-to-Noise Ratio of 0 dB. Despite some of the issues with bistatic receivers, the benefits outweigh the drawbacks, and these systems are a viable option to increase the amount of radar data available for specific events (Wurman 1994).

2.3 Observing System Simulation Experiments

Testing the impact of bistatic radar data in a numerical weather prediction model may be completed in multiple ways. One option is conducting Observing System Simulation Experiments (OSSEs), which are often used to quantify the impacts of assimilating data from novel observing systems (Snyder and Zhang 2003; Tong and Xue 2005; Potvin et al. 2012; Potvin and Wicker 2013). The concept behind OSSEs is relatively simple: create a truth simulation, then create emulated observations from the truth simulation and assimilate them into several experimental simulations, and finally compare the experimental runs to the truth run and diagnose any improvement or degradation of the forecast. A truth run for convective storm OSSEs is typically generated using an idealized model and uses a representative sounding to create the truth run environment. A thermal bubble is introduced to initiate convection and the model then runs out a specified number of hours. The truth simulation for an OSSE is essentially a control run that the experiments are compared to. Synthetic observations are generated from the truth simulation and assimilated into the experimental runs. Then these experimental runs are integrated forward until the desired run time is reached. Once this is complete, comparisons between the truth run and the experimental runs can begin. A simplified schematic of this process is shown in Figure 2.7.

OSSEs are often grouped into two categories with slightly different setups: a perfect model OSSE and an imperfect model OSSE, and each has unique strengths and weaknesses. Using a perfect model OSSE ensures that the only differences between the truth run and subsequent experiments is the assimilation of synthetic observations, allowing their impact to be isolated. Studies by Potvin et al. (2012); Potvin and Wicker (2013); Tong and Xue (2005); Yussouf and Stensrud (2010) all used perfect model OSSEs with identical configurations between the truth and experimental simulations. Perfect

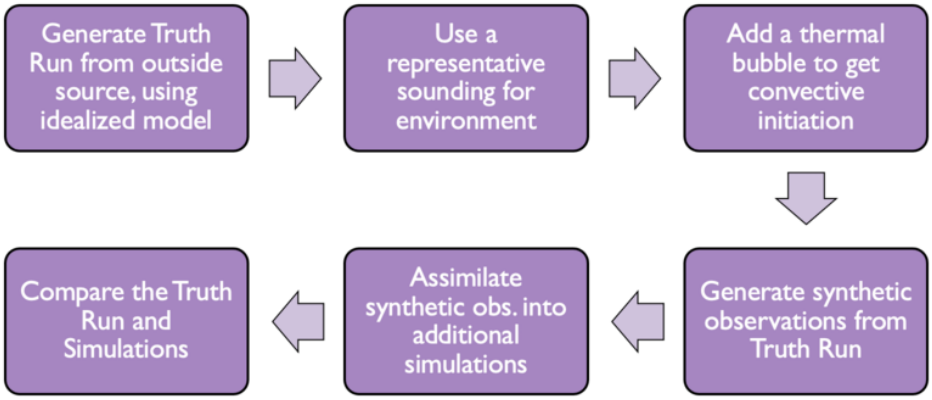

Figure 2.7: A simplified outline of the typical process used in creating OSSEs. The first three steps are related to conducting an idealized simulation, with the remaining steps being specific to OSSE creation.

model OSSEs may be run across a diverse suite of convective modeling scenarios, such as Tong and Xue (2005) that applied a free-slip to the bottom boundary of the model, assumed perfect observational operators, and assumed that the prediction model was perfect. Similarly, Yussouf and Stensrud (2010) assumed the model was perfect and the environment was perfectly represented, as well as made the experimental domain grid spacing and the truth run grid spacing identical. Potvin et al. (2012) used a stationary grid with flat surfaces and other error sources set to the simplest setting. Finally, Potvin and Wicker (2013) applied specific soundings and thermal bubbles for convective initiation and other simplified setting. Despite the repeatable results from these studies, it is important to note that any conclusions from a perfect model OSSE will likely be degraded when applied to real-time scenarios owing to the presence of model error (Potvin and Wicker 2013). Perfect OSSEs are typically too optimistic, as a result of removing as much outside error sources as possible (Stratman et al. 2020). Due to this limitation, a perfect model OSSE is often not realistic, and the real-time model error will far outweigh the impacts of the assimilated observations seen in the

perfect model OSSE. Therefore, any positive impact from the observations would not be noticeable in a real-time forecast.

Imperfect OSSEs use different model configurations between the truth simulation and the experimental simulations to create a more realistic test of observation impact. Imperfect OSSEs are run similarly to perfect model OSSEs but include a few differences. Similar to the perfect model OSSE, the truth run is used to create synthetic observations that act as the base state for the experimental run. Then the new data are assimilated into these experimental runs, and they are run out to the specified times. Once the experimental simulations are done, they can be compared to the truth simulation. However, for imperfect OSSEs, different model configurations are used between the truth run and the experimental runs. Therefore, model error will be present in the experimental runs, in addition to the impacts from the assimilated synthetic observations. As a result of model error being included in the experiments, it makes it easier to determine whether the observations are having a large enough impact that they will be useful for improvement in a realistic forecast. Therefore, imperfect OSSEs have the potential to be more beneficial for real-time applications.

Chapter 3

Event Background

On 7 May 2020, a large, hail-producing supercell tracked across northern Texas dropping significant severe hail (>2 inches) throughout its life cycle (Figures 3.1 and 3.2). The Storm Prediction Center (SPC) issued a Slight Risk for severe weather across all of central Oklahoma, most of northern Texas, and the eastern Texas Panhandle at 1200 UTC on 7 May 2020. At 2000 UTC on 7 May, SPC upgraded to an Enhanced Risk for southwestern Oklahoma and the southeast corner of the Texas Panhandle, which is where this specific supercell would eventually track (Figure 3.3). This storm initiated at 2130 UTC on 7 May 2022 in Hall County, Texas, and reached maturity about 45 minutes later at 2215 UTC (for Texas counties, see Figure 3.4). At 2224 UTC, the supercell began to split while located over Childress County, Texas, and completed this split at 2251 UTC. The left split moved into Greer County, Oklahoma, while the right split took a hard right turn towards Hardeman County, Texas. The left split continued its northeasterly path until it began to weaken at 2349 UTC over northeastern Kiowa County, Oklahoma. The right split, and dominant storm, continued tracking southeasterly, straddling the Oklahoma/Texas border, dropping significant severe hail across Hardeman and Wilbarger County, Texas. By 0017 UTC on 8 May, the supercell was within Wilbarger County, Texas, continuing its southeastward progression. The hail core moved into portions of northeastern Baylor County, Texas, and northwestern portions of Archer County, Texas, from 0047 UTC until 0110 UTC and continued to drop significant severe hail throughout Archer County, before finally exiting the county

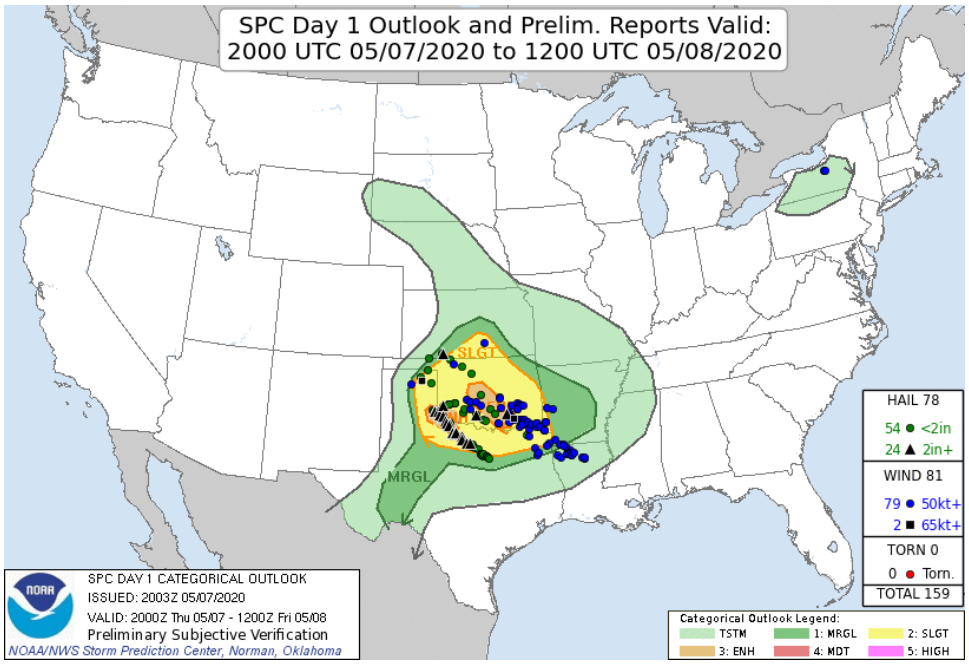

Figure 3.1: Storm reports from the Storm Prediction Center for 7 May 2020.

at 0158 UTC. The supercell continued to drop hail throughout the rest of its life cycle, until dissipating over southern Tarrant County and northern Johnson County, Texas, around 0400 UTC. There were 22 reports of 2-inch or larger hail along the path of this supercell, as well as several other reports of severe hail (>1 inch). The smaller hail reports occurred closer to when the storm dissipated (Storm Prediction Center, Figure 3.1). The 0.9° base reflectivity swath of this storm shows the path it took from 2100 UTC until 0200 UTC, which included most of the life cycle (Figure 3.2). Note that the 0.5° base reflectivity was not used due to the Supplemental Adaptive Intra-Volume Low-Level Scans, or SAILS, resulting in an incorrect double hook signature for some of the images. This was caused by SAILS adding an additional 0.5° scan for every volume, resulting in GR2Analyst Version 3 showing both 0.5° scans for a single frame.

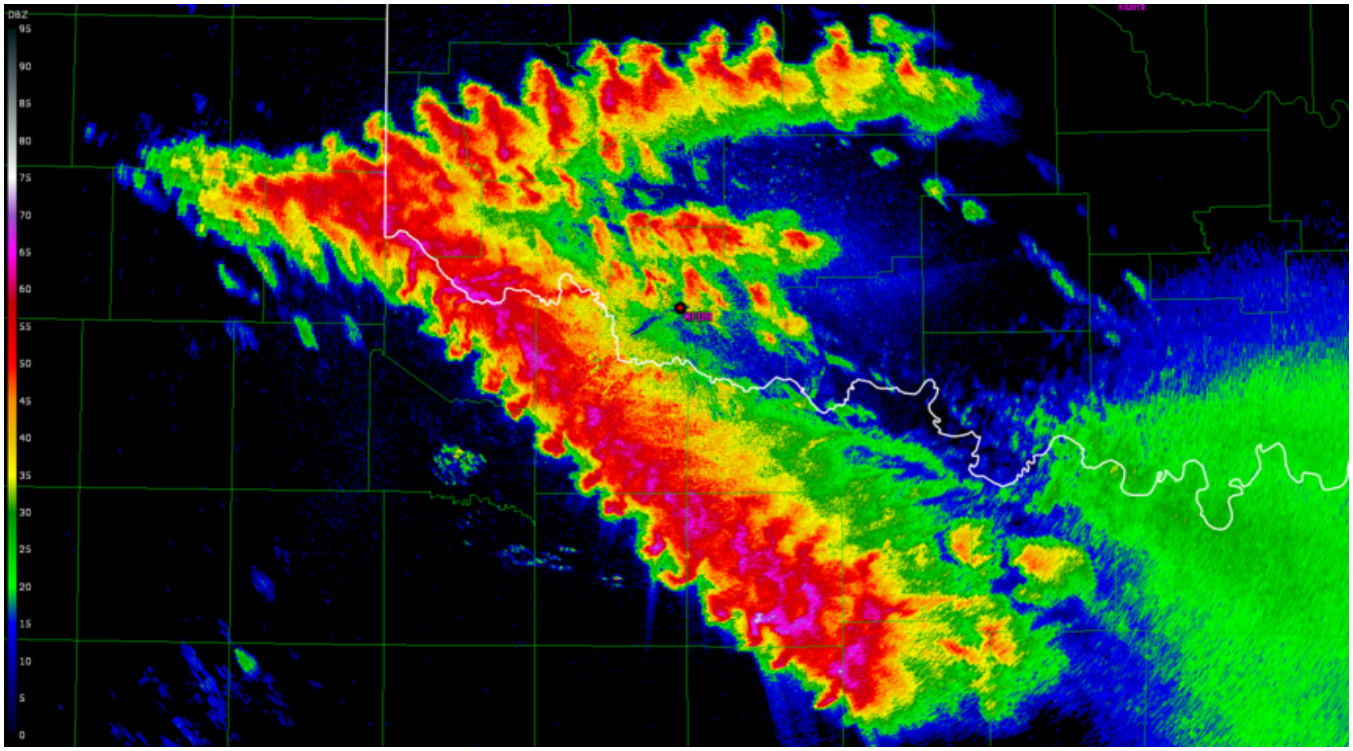

Figure 3.2: Reflectivity swath of the 7 May 2020 hail-producing supercell over northern Texas. This image was created in GR2Analyst Version 3, using the 0.9° base reflectivity from KFDR. The swath was generated from 2100 UTC on 7 May until 0200 UTC on 8 May. Images were generated for every 2-3 volume scans, which was about every 10-15 minutes.

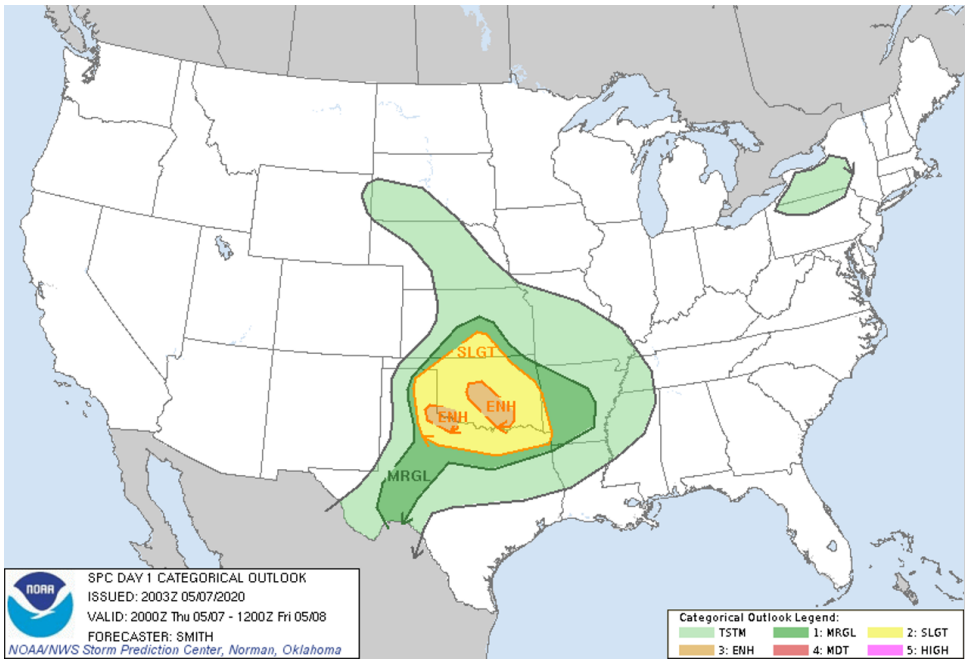

Figure 3.3: Enhanced Risk issued by the Storm Prediction Center at 2000 UTC on 7 May 2020.

The 7 May 2020 event is notable in that WoFS produced extremely accurate forecasts of the supercell this day. Despite being before CI, the 2000 UTC run accurately forecast the supercell's initiation, location, size, and track (Figure 3.5). Similarly, accurate forecasts were produced at 2100 and 2200 UTC, shortly before and shortly after convective initiation (Figures 3.6 and 3.7). All three forecasts leading up to, and shortly after, convective initiation show good agreement among the members of where a storm is going to occur, and how strong it would likely be, as indicated by high probabilities of composite reflectivity exceeding 40 dBZ. The 2000 UTC forecast accurately produced high probabilities along the track of the supercell, but the areal extent of the probability swath was wider with a lower maximum likelihood than the 2100 and 2200 UTC forecasts. This indicates that the cycled DA provides a more specific and confident forecast of the supercell track in the post-CI forecasts.

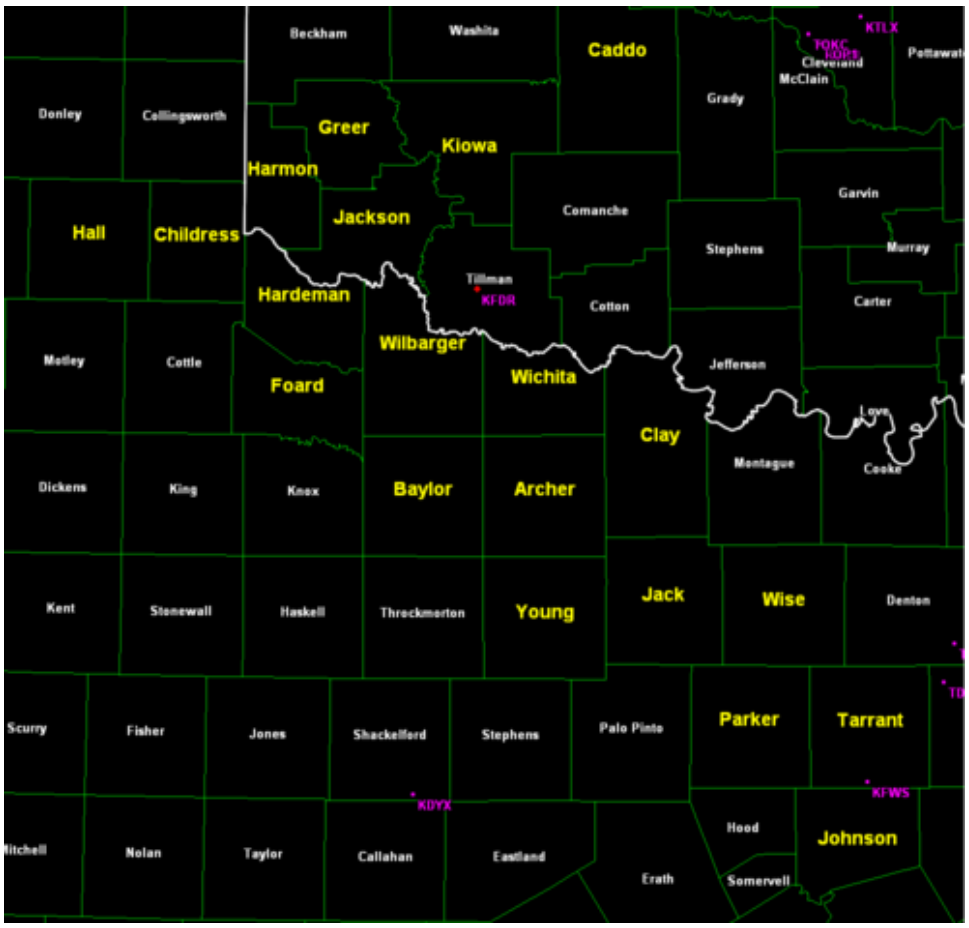

Figure 3.4: A reference of the Oklahoma and Texas counties. The bold, yellow counties are those directly impacted by the 7 May 2020 supercell. NWS radar identifiers are in purple with purple dots at their locations. The selected radar, KFDR, is indicated with a red diamond. Image generated with GR2Analyst Version 3.

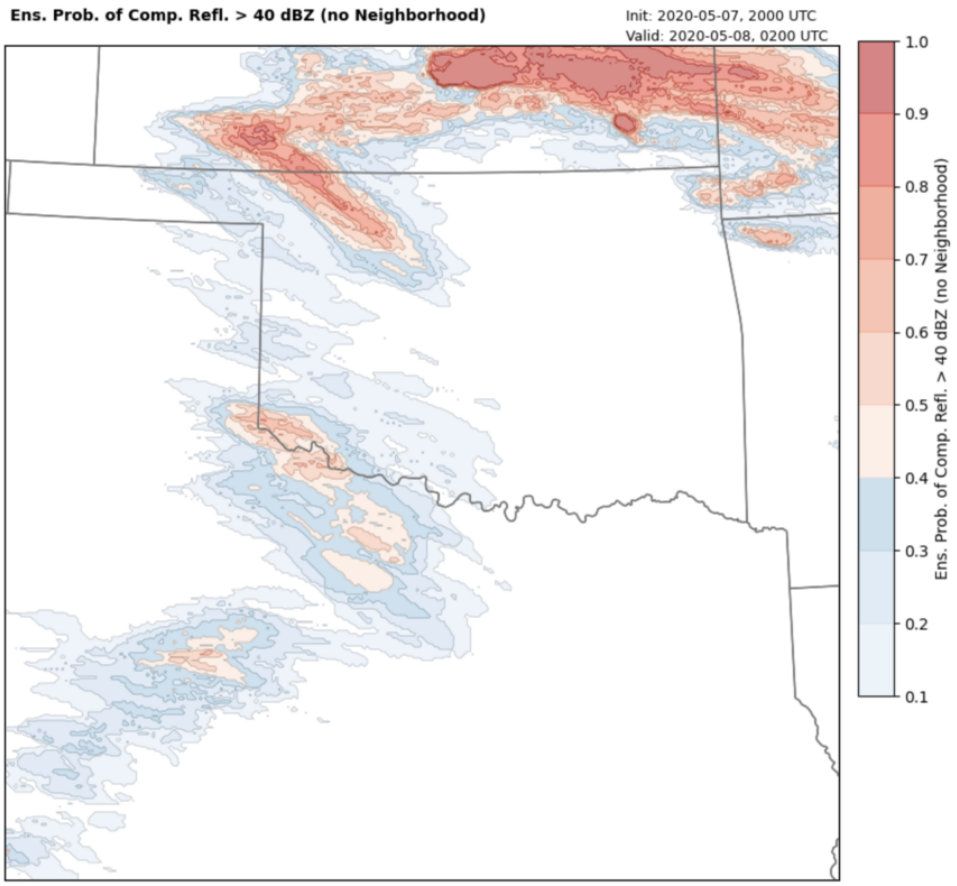

Figure 3.5: Ensemble, grid-scale probability of composite reflectivity being >40 dBZ for the 2000 UTC WoFS forecast on 7 May 2020. The swath of probabilities in northern Texas depict the forecast track of the supercell. This image was taken from the WoFS viewer page.

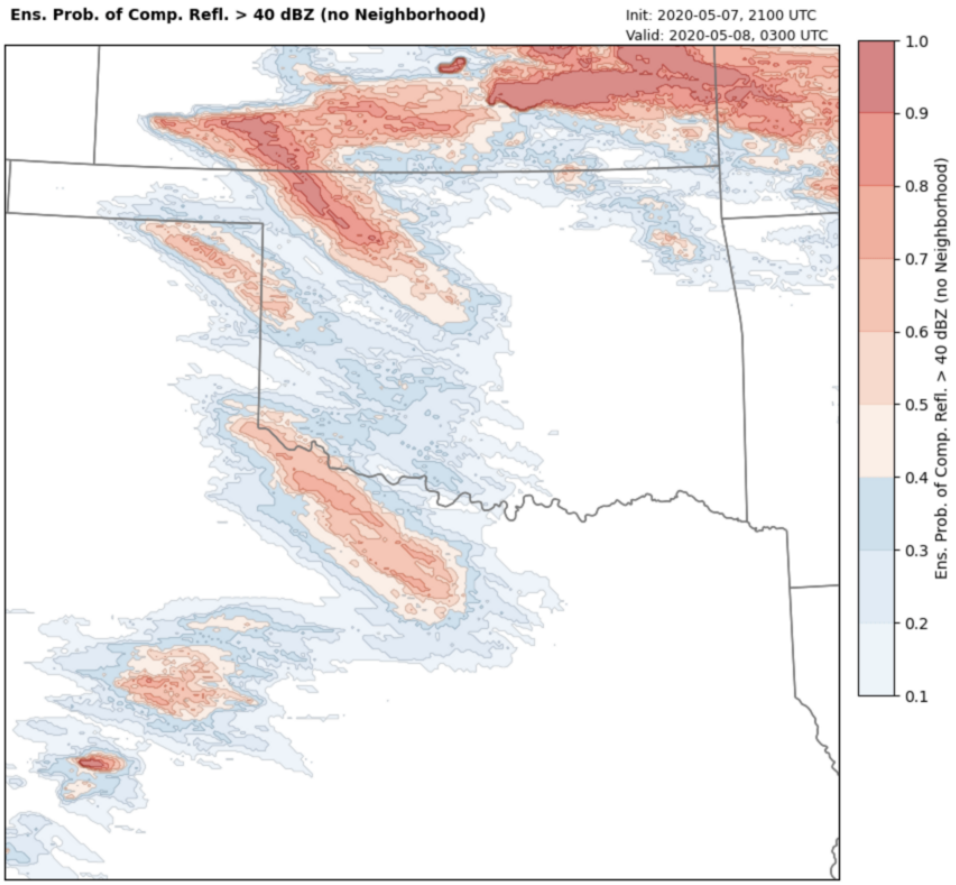

Figure 3.6: As in Figure 3.5, but for the 2100 UTC forecast on 7 May 2020. This image was taken from the WoFS viewer page.

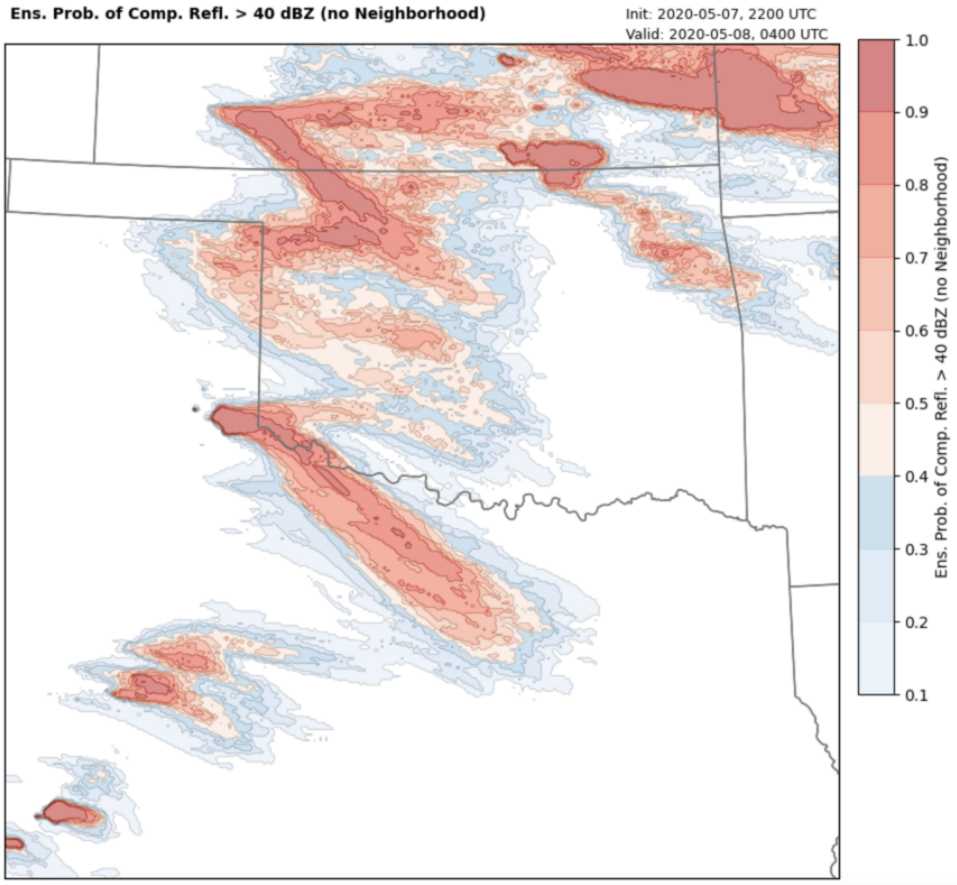

Figure 3.7: As in Figure 3.5, but for the 2200 UTC forecast on 7 May 2020. This image was taken from the WoFS viewer page.

The 7 May 2020 experiment was a high-impact event that was predicted extremely well by WoFS, even in the pre-CI forecasts. Additionally, this experiment had an isolated supercell with minimal surrounding reflectivity returns within the WoFS domain. These reasons motivate the selection of this experiment for the OSSE. The isolated supercell allows for the impacts of the multistatic network to be seen better than what might occur with a line of storms or other complexes. These additional storms would not allow for the multistatic network to be isolated because the storms would interact together and complicate the analysis of multistatic network impacts. Therefore, the isolated supercell on 7 May 2020 is an ideal candidate for the OSSE.

Chapter 4

Experimental Design

4.1 Truth Run

For the Truth Run, it was desirable to select a member from an earlier run of WoFS on 7 May 2020, to assess whether assimilating the multistatic network data could improve WoFS forecasts, particularly near the time of CI. Therefore, the 2000 UTC run was selected, as it was initialized over an hour and a half before storm initiation and matches the earlier desired run time. Of the 18 members for the 2000 UTC run on 7 May 2020, Member 12 displayed an accurate depiction of the life cycle, splitting, and hard right turn of the 7 May northern Texas supercell, despite initiating the storm nearly an hour after observed convection initiation. Additionally, Member 12 produced an isolated supercell with minimal convection near the storm or near the boundaries, allowing a high-resolution nest to be placed in the WoFS domain with no additional convection except for the target storm. For these reasons, Member 12 was selected as the Truth Run for this OSSE.

To create the Truth Run, Member 12 was downscaled from the original 3-km horizontal grid spacing to a grid spacing of 250-m to have sufficient resolution to create synthetic radar data with the same resolution as a WSR-88D, as well as to resolve finer scale features that would not be seen in the typical 3-km grid spacing of WoFS. The 250-m grid spacing does not cover the entire domain of a WoFS run, as this would require additional computational expenses not necessary for this project. The Truth

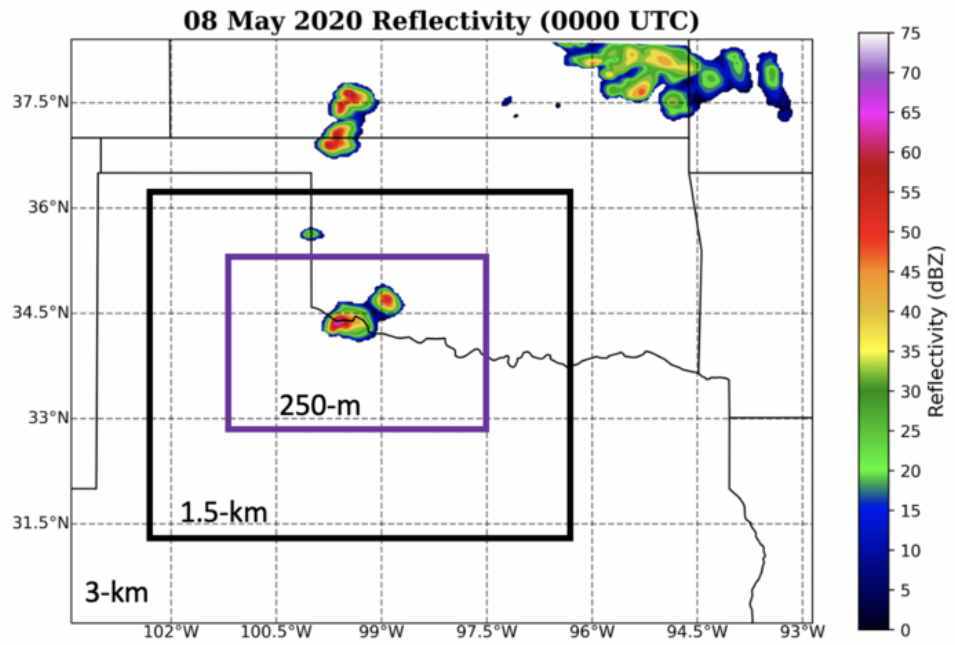

Figure 4.1: The nested grids used to downscale and create the Truth Run is shown. The thin, black line shows the 3-km grid, which is the same as the WoFS run for 7 May 2020. The thick black line shows the 1.5-km domain, and the thick purple line shows the 250-m truth run domain.

Run domain is a subset of the full WoFS domain and focuses only on the track of the northern Texas supercell. The 250-m grid spacing on a subset of the WoFS domain was achieved using nested gridding of 3-km to 1.5-km and down to 250-m. The specific location of each respective grid is show in Figure 4.1.

To create the Truth Run, the 3-km domain was initialized at 2000 UTC and received its initial and boundary conditions from the HRRRDAS. The 1.5-km domain uses the 3-km domain for initial and boundary conditions, but was initialized as 2200 UTC, rather than 2000 UTC. The later initialization for the 1.5 km domain was chosen because initializing the 1.5-km domain at 2000 UTC resulted in excessive spurious convection initiation around the boundary edges, which degraded the 1.5-km domain

storm, as well as the 250-m domain storm. Similarly, the 250-m domain was initialized at 2200 UTC and the initial and boundary conditions taken from the 1.5-km domain.

The Truth Run begins at 2200 UTC on 7 May and runs out 4 hours, until 0200 UTC on 8 May. The goal of this simulation was to capture the convection initiation, storm split, hard right turn, and the middle mature stage of the supercell. Data were output every 5 minutes for the Truth Run, resulting in a high spatial and temporal resolution depiction of the supercell. Additionally, the 250-m Truth Run allows for additional analysis of whether the experiments can resolve the finer-scale processes with the additional data. At 2320 UTC on 7 May, the Truth Run has a much higher resolution depiction of the storm as it begins to split (Figure 4.2). The WoFS member 12 has a smoother storm, with less detail and less elongation of the storm, particularly the left split. However, the position is similar between the two. Additionally, the Truth Run has some spurious convection to the west that is filtered out in the WoFS members. By 0000 UTC of 8 May, the Truth Run has a much more complex storm structure, with the dominant storm as well as the left split and an additional core of higher reflectivity between the right-split and the left-split (Figure 4.3). However, storm location remains similar between the Truth Run and the WoFS member. The WoFS member has a stronger storm at this time than what is depicted in the Truth Run, while the 2320 UTC storms match intensity well. It is obvious that the Truth Run is depicting more smaller scale structures than the WoFS member, but this is expected given the grid spacing difference.

Using a downscaled WoFS members as the Truth Run is different than the typical approach of using an idealized simulation. While using a separate model for a truth run is a viable option, it would produce a truth run in an idealized simulation with a homogeneous environment. The homogeneous environment allows for forced convective initiation through the use of a warm bubble or other means, no terrain influences,

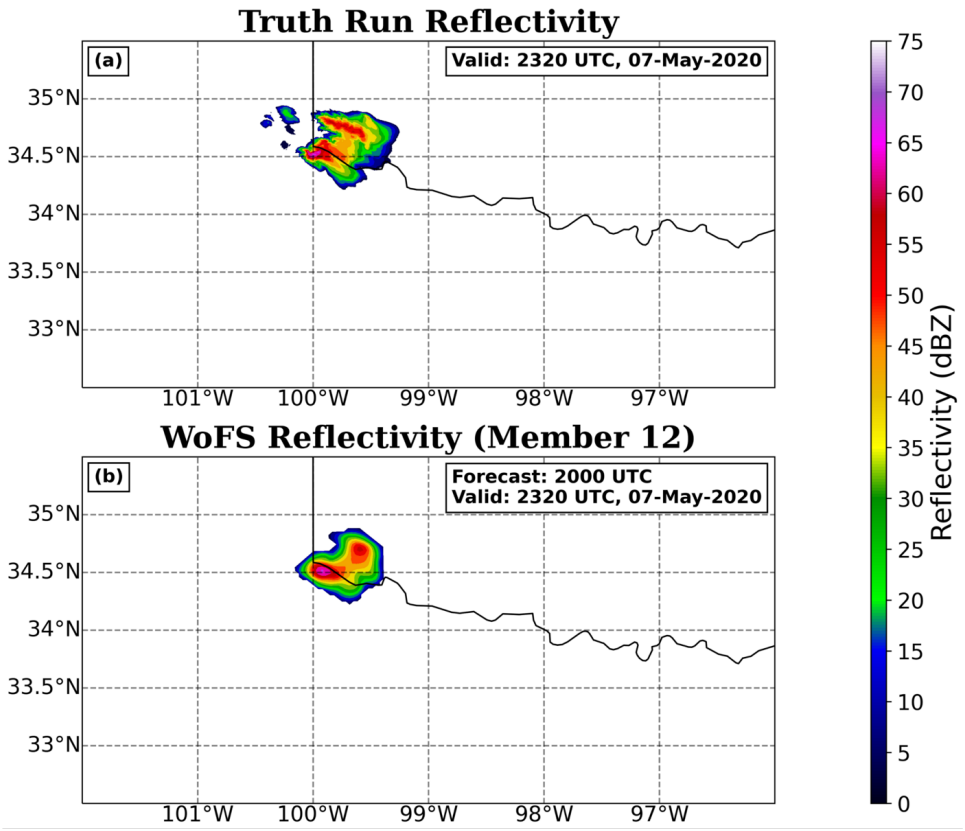

Figure 4.2: Reflectivity comparison for (a) the Truth Run at 2320 UTC and (b) the 2000 UTC WoFS Member 12 forecast valid at 2320 UTC. Reflectivity in dBZ.

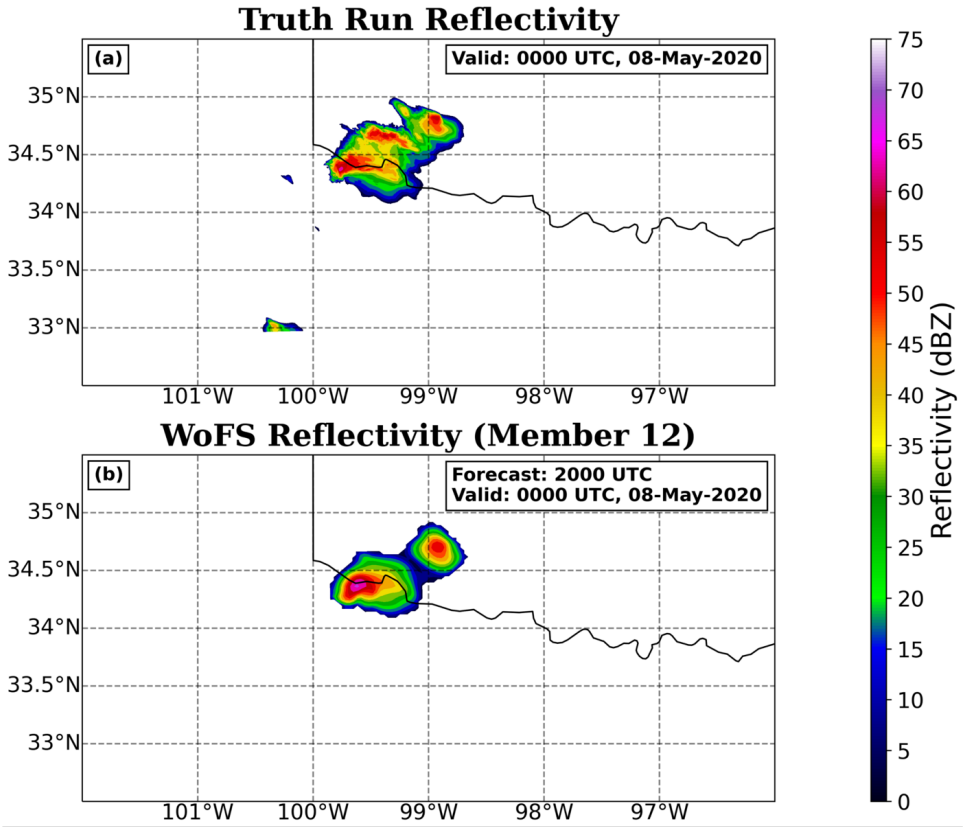

Figure 4.3: As in Fig. 4.2, but for 0000 UTC on 8 May 2020.

and no other potential error sources. This is a useful approach when attempting to minimize model error, but the results will not be as applicable to real-time runs of a model. However, using a WoFS member for the truth run allows for a heterogeneous environment. A heterogeneous environment allows for a truth run generated from a semi-operational numerical weather prediction system with realistic CI processes, the inclusion of terrain, surface fluxes, and other potential error sources that are more representative of the real atmosphere. Therefore, we expect any impacts identified from assimilation of multistatic network observations to be more likely to translate to real-time runs since a real-time system was used for the OSSE. Additionally, results from the OSSE would be more likely to translate into real world scenarios and will potentially provide a better understanding of the impacts of assimilating data from a multistatic network.

However, there is a complication with using the same model for both the Truth Run and the experimental runs. For this project, the Truth Run is derived from Member 12 of the 2000 UTC 7 May 2020 WoFS forecast. Therefore, if Member 12 was left in the ensemble, the experimental runs would likely produce an identical forecast, compared to the Truth Run, for Member 12. To avoid this error, Member 12 was removed from the experimental runs. Therefore, the experimental runs for this OSSE were run with 35 EnKF members, rather than the usual 36 members. This allowed for Member 12 in the experimental runs to have a different configuration than that of the 2000 UTC 7 May WoFS run. This also prevented the possibility of a perfectly matched forecast from Member 12 in the experimental runs.

4.2 Experiments

Previous research shows that assimilating additional radar data improves the spin up of convection in WoFS, as well as improves the evolution of the storm in the subsequent forecasts (Guerra et al. 2022; Stratman et al. 2020; Kerr et al. 2021). As a result, this research uses a simulated, multistatic network of passive receivers to create additional radar data. The OSSE experiments are designed to test if assimilating additional radar data from a multistatic network allows for WoFS to spin-up convection quicker and produce more accurate analyses and forecasts.

An imperfect OSSE is used to test the impacts of assimilating multistatic velocity data using a simulated, network of 5 passive receivers (hereafter referred to as the Multistatic experiment). To create the required transmitting radar, an emulated WSR-88D site near the location of the Frederick radar (KFDR) is created and surrounded by the network of 5 passive receivers (Figure 4.4). A second experiment is produced, which only assimilates the emulated KFDR radar data and is referred to as the WSR-88D Only experiment throughout the remainder of the manuscript. The WSR-88D Only experiment is used to simulate what WoFS would have produced this day if it had only assimilated radar reflectivity and radial velocity. The goal is to compare these two experiments to each other, and the Truth Run, to determine if the Multistatic experiment outperforms the WSR-88D Only experiment, which would indicate that assimilation of multistatic Doppler velocity observations are improving WoFS forecasts.

For both the Multistatic and WSR-88D Only experiment, six separate forecasts are produced at 2200, 2215, 2230, 2245, 2300, and 2330 UTC on 7 May. The 15-minute forecasts were added to isolate differences between the experiments during the spin-up of convection, as well as to determine if the Multistatic experiment provides any additional lead-time that the WSR-88D Only experiment does not. Each forecast runs

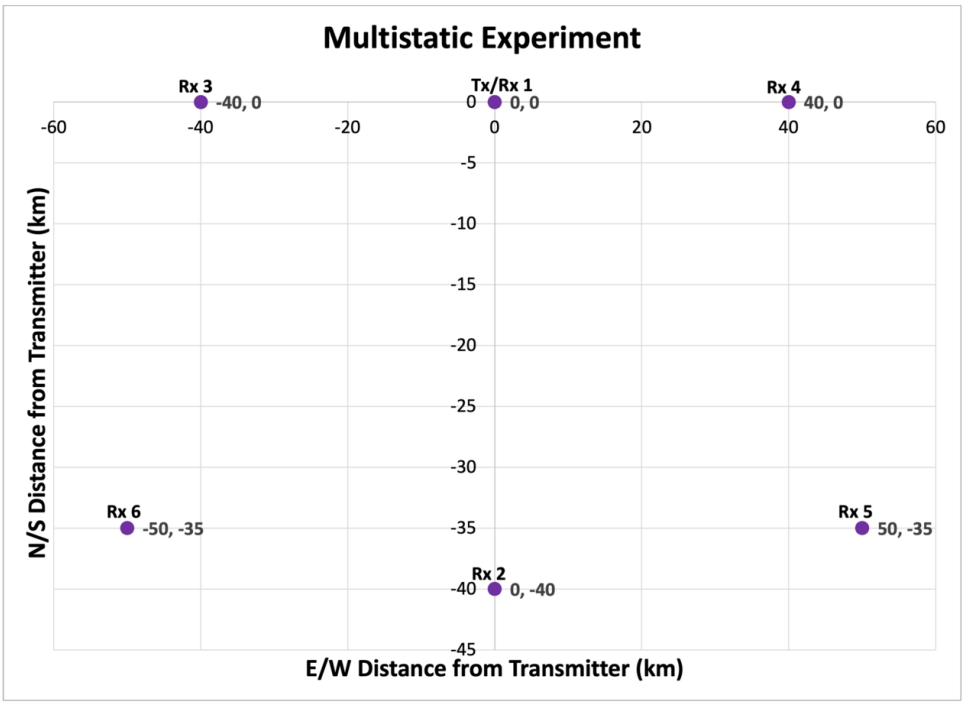

Figure 4.4: Layout for the receivers for the Multistatic experiment. North/South distance from the transmitter is on the y-axis and East/West distance from the transmitter is on the x-axis. The transmitter is located at (0,0) along with a receiver, which creates the emulated WSR-88D. Five other receivers are placed around the transmitter at (-40, 0), (40,0), (-50,-35), (0,-40), and (50,-35) to obtain different viewing angles of the storm.

out four hours, ending the run at 0200, 0215, 0230, 0245, 0300, and 0330 UTC on 8 May, respectively. It is important to note that the Truth Run is only run until 0200 UTC on 8 May. Therefore, each forecast is only analyzed through 0200 UTC on 8 May so that it can be compared with the Truth Run.

Each experimental experiment is produced with WoFS, using 3-km grid spacing that covers the area shown in Figure 4.1. On a typical day, WoFS would assimilate radar reflectivity and radial velocity, satellite cloud water path observations, ASOS data, and mesonet data (when available). However, for the Multistatic experiment only the emulated WSR-88D radar reflectivity and radial velocity, as well as the bistatic velocity from the multistatic network, are assimilated in order to isolate the impacts of the multistatic network and limit comparisons to the isolated, splitting supercell. For the WSR-88D Only experiment, only the emulated WSR-88D radar reflectivity and radial velocity data were assimilated. Data were assimilated every 15 minutes from 2200 UTC until 2330 UTC, resulting in 1, 2, 3, 4, 5, and 7 DA cycles for the 2200, 2215, 2230, 2245, 2300, and 2330 UTC forecasts, respectively. The WSR-88D Only experiment provides a comparison basis for the Multistatic experiment, with the WSR-88D Only experiment simulating something analogous to what WoFS would have produced with only the KFDR data that day.

The decision to not include all the possible data sources for WoFS derives from the desire to isolate the impacts of the multistatic network on WoFS forecasts. Additionally, had the other data sources been included in these experiments, the data would be archived data from 7 May 2020, rather than emulated data from the Truth Run. Using a combination of data sources from the observed event and Truth Run would have the potential to severely degrade WoFS analyses and forecasts. For example, had satellite cloud water path observations from 7 May 2020 been assimilated, there may have been observations in a location that did not match the location of the storms in the Truth

Run. As a result, the satellite observations could have forced the experimental runs to produce a storm that did not match the location of the supercell in the Truth Run. For these reasons we only assimilate the WSR-88D and multistatic network observations to isolate the impact of these data and improve comparisons.

4.2.1 Multistatic Experiment

The multistatic network consists of an emulated WSR-88D and a network of five passive receivers. To create these data, a bistatic radar emulator code developed by Emmerson (2022) is modified to work for a WoFS simulation. The radar emulator code initially used the Cloud Model 1 for inputs of meteorological variables but was changed to use WoFS for these inputs. An emulated KFDR radar is created with all the specifications of a WSR-88D, and the passive receiver data is emulated using this transmitting radar. The gate spacing for this emulator is 250 m and the domain is 120 km x 120 km x 17.5 km. A more detailed explanation of the radar emulator code can be found in Emmerson (2022).

For the multistatic network design, the five additional passive receivers were spaced around the emulated radar, producing a pentagon shape, with the top point being south of the radar (Figure 4.4). Receiver locations are relative to the transmitting radar, which was placed at the center of the Truth Run domain (Figure 4.1). Receivers 1, 2, 3, 4, 5, and 6, were placed at [0,0], [0,-40], [-40,0], [40,0], [50,-35], and [-50,-35], respectively (Figure 4.4). Receiver 1 (Rx 1) is collocated with the transmitter, creating the emulated KFDR radar, which is placed slightly further west than the location of the real KFDR. Data were emulated for the typical radar elevation angles for a non-SAILS, volume coverage pattern 11 (VCP 11): 0.5°, 0.9°, 1.3°, 1.8°, 2.4°, 3.1°, 4.0°, 5.1°, and 6.4°, with all data above 6.4° being cut off. The network design in Figure 4.4 provides sampling close to the storm throughout various stages of the storm from different look

angles (Figures 4.5 and 4.6). Therefore, this design was optimal for sampling all stages of storm evolution, as the goal is to sample the storm around convection initiation, maturation, the split, and the hard right turn. Assessing the WoFS analysis of this storm was one goal of this OSSE, as it is unknown whether assimilating multistatic network observations would allow WoFS to analyze the storm more accurately. If assimilating the multistatic network velocity observations improve the analysis of the storm, then it is expected that the subsequent forecasts would likely improve as well (Guerra et al. 2022). Improving earlier forecasts relative to convection initiation would allow for longer lead-time for predicting the severe thunderstorm, an ideal outcome of this experiment.

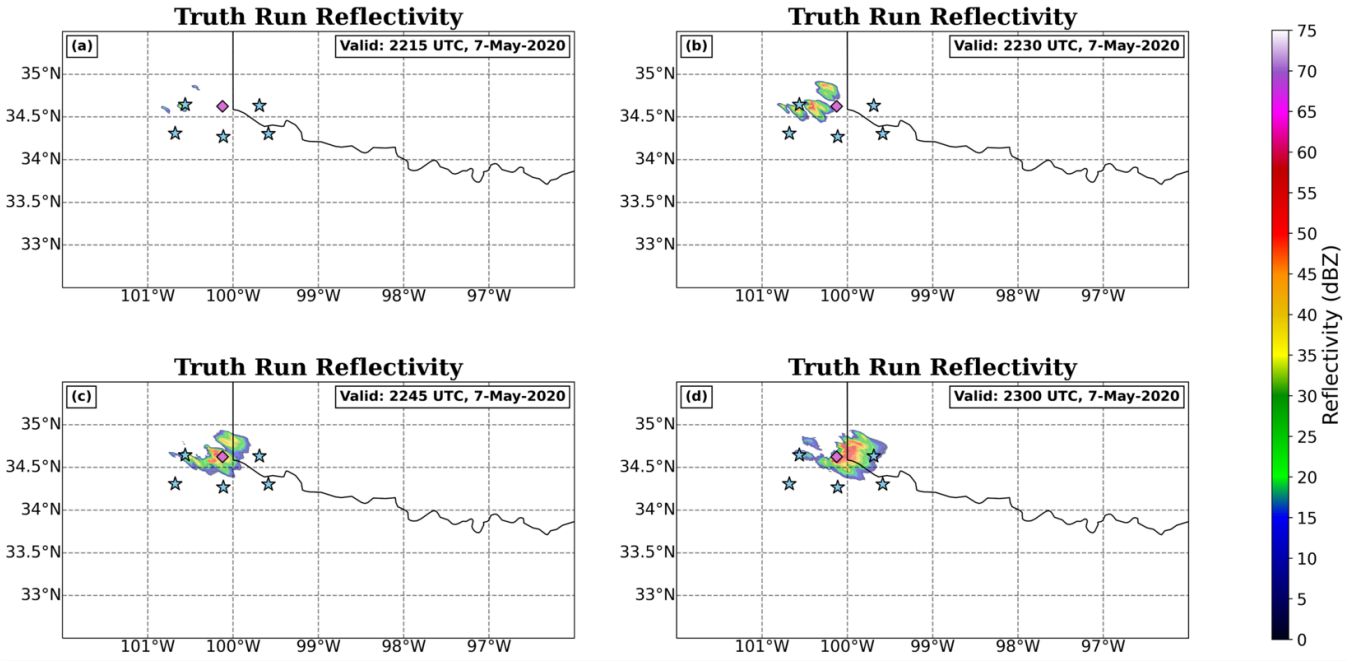

Figure 4.5: Truth Run reflectivity (dBZ) contour filled with the locations of the multistatic network receivers. Receivers are shown as blue stars and the transmitter is the purple diamond. Time steps chosen were (a) 2215 UTC, (b) 2230 UTC, (c) 2245 UTC, and (d) 2300 UTC.

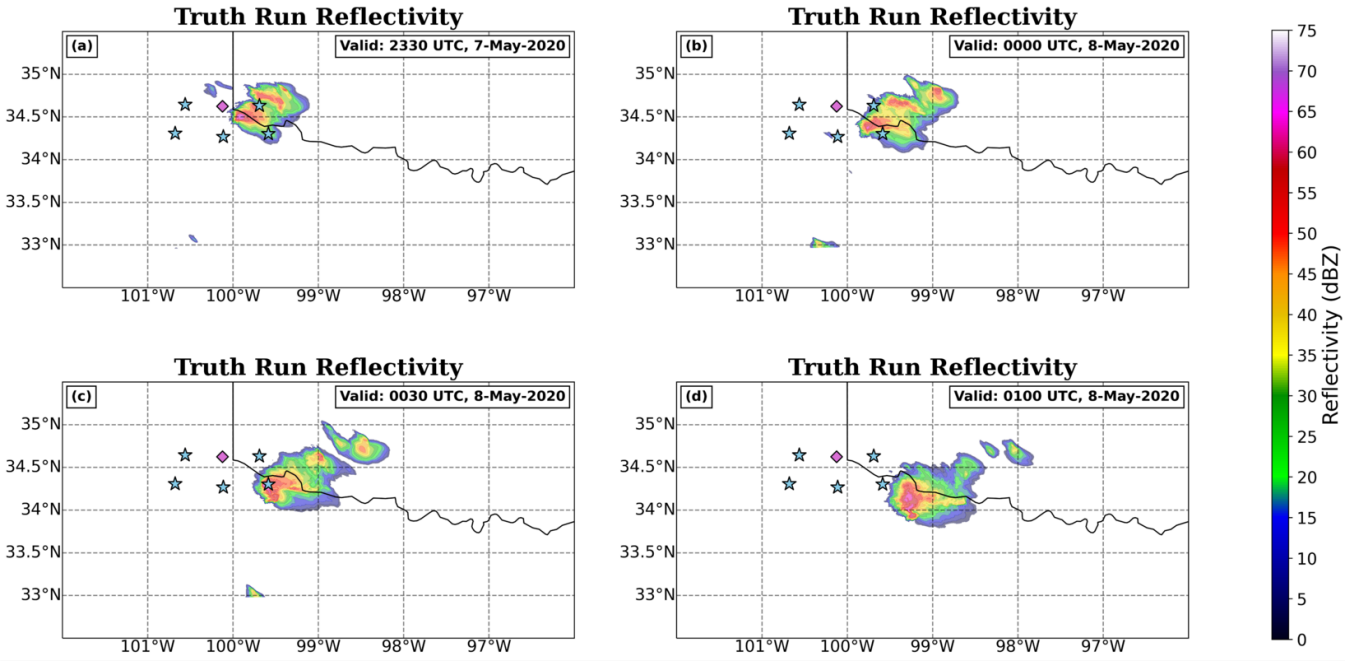

Figure 4.6: Truth Run reflectivity (dBZ) contour filled with the locations of the multistatic network receivers. Receivers are shown as blue stars and the transmitter is the purple diamond. Time steps chosen were (a) 2330 UTC, (b) 0000 UTC, (c) 0030 UTC, and (d) 0100 UTC.

4.2.2 WSR-88D Only Experiment

The WSR-88D Only experiment is similar to the Multistatic experiment; however, for this experiment, only data from the emulated KFDR WSR-88D are assimilated into WoFS. The WSR-88D Only experiment was designed as a control run, meaning that the Multistatic experiment could be compared to the WSR-88D Only experiment as a method of assessing the impact of assimilating bistatic velocity observations on WoFS analyses and forecasts. Comparing the Multistatic experiment to the Truth Run provides only one potential interpretation of results. The WSR-88D Only experiment creates a depiction similar to what the real-time WoFS would have produced on this day. Adding another comparison basis allows the impacts to be assessed based on whether the multistatic network improves the analyses and forecasts over what is produced from assimilated observations from a single WSR-88D, which is what forecasters would be dealing with in real time. Therefore, the WSR-88D Only experiment serves as a baseline performance of WoFS, although without the assimilation of the other observations, such as satellite cloud water path, on 7 May 2020.

Chapter 5

Data and Analysis

5.1 Assimilated Data

Not all the data produced by the multistatic network were assimilated into WoFS for these experiments. No reflectivity observations provided by the radar emulator were assimilated into the two OSSEs. Instead, the assimilated reflectivity values came directly from the interpolated Truth Run reflectivity field, which allows the only error source to be from interpolating the 250-m Truth Run to a coarser, 3-km grid spacing. Narrowing error sources to only interpolation errors provide a useful starting point for the OSSEs and isolates the impact of the multistatic network's bistatic velocity observations.

To interpolate the Truth Run simulated reflectivity, a Cressman objective analysis scheme is used with a 3-km radius of influence. Observations are generated in horizontal slices in 10 vertical levels from 1-10 km above ground level. All reflectivity values below 20 dBZ are thresholded out, with values below 15 dBZ set to 0. Any reflectivity value between 15 and 20 dBZ are set to NaN, or no observations generated for assimilation, which creates a halo around the observed storm and limits the suppression of ongoing storms. Additionally, assimilated 0 dBZ observations helps prevent spurious convection from developing within the OSSE. The process for reflectivity observation generation is identical to how reflectivity is processed for real-time WoFS runs (Wheatley et al. 2015;

Jones et al. 2020). This allows the OSSEs to match the real-time WoFS configuration for reflectivity assimilation.

Bistatic velocity observations were emulated from the Truth Run using a radar emulator code, modified to include the five receivers for the Multistatic experiment. Bistatic velocity radar volumes are assumed to be collected instantaneously and a non-SAILS, volume coverage pattern 11 (VCP11) is used to collect radar returns up to 6.4° for receivers, which adequately captures the low- to mid-levels of the supercell. To mitigate erroneous returns near the baseline between the passive receivers and the transmitting radar, any observations with bistatic angles of $< 35°$ or $> 145°$ are removed. In addition to this, bistatic velocities are removed wherever the reflectivity is less than 15 dBZ to diminish spurious convection within the OSSEs and remove bistatic velocities in regions of low power returns that are more likely to be erroneous. An observation error value of 3 ms^{-1} is applied to the bistatic velocity observations, which is identical to the error added for typical radial velocity observations. A Cressman scheme with a 3-km radius of influence is used to interpolate the bistatic velocities onto the conical surface of the elevation angles. In order to limit noisy observations around the edge of the storm, the Cressman-interpolated observations produced with less than 15 bistatic velocity observations are removed. The process for bistatic velocity observation processing is similar to the real-time WoFS radial velocity processing (Wheatley et al. 2015; Jones et al. 2020), but this process is harsher to limit the influence of noisy or erroneous observations. An example of the assimilated bistatic velocity observations after observation processing is shown in Figure 5.1, the assimilated reflectivity at 1 km after observation processing for the same time is shown in Figure 5.2, and the corresponding Truth Run reflectivity is shown in Figure 5.3. These bistatic radial velocity observations are for the 0.5° elevation angle at 2230 UTC. From this single elevation angle, it is shown that the multistatic network observations are providing additional

information to the OSSE that is different from what the transmitting radar shows for the same elevation angle at the same time. Each receiver has a different density of bistatic velocity observations, with receivers that are further away having fewer returns than closer receivers.

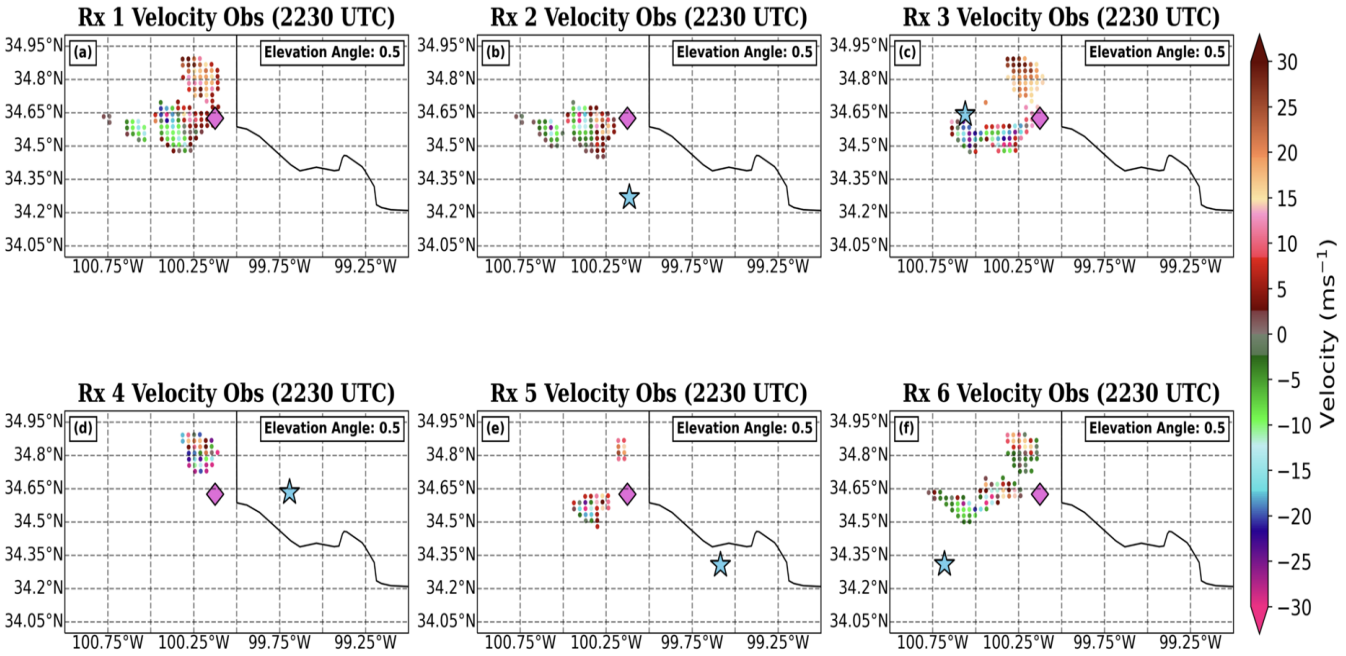

Figure 5.1: 2230 UTC assimilated 0.5° radial velocity (ms^{-1}) observations for (a) transmitting radar, and assimilated 0.5° bistatic velocity (ms^{-1}) for (b) receiver 2, (c) receiver 3, (d) receiver 4, (e) receiver 5, and (f) receiver 6. Receiver locations are represented by blue stars, while the transmitter location is represented by the purple diamond. Images are zoomed in for detail.

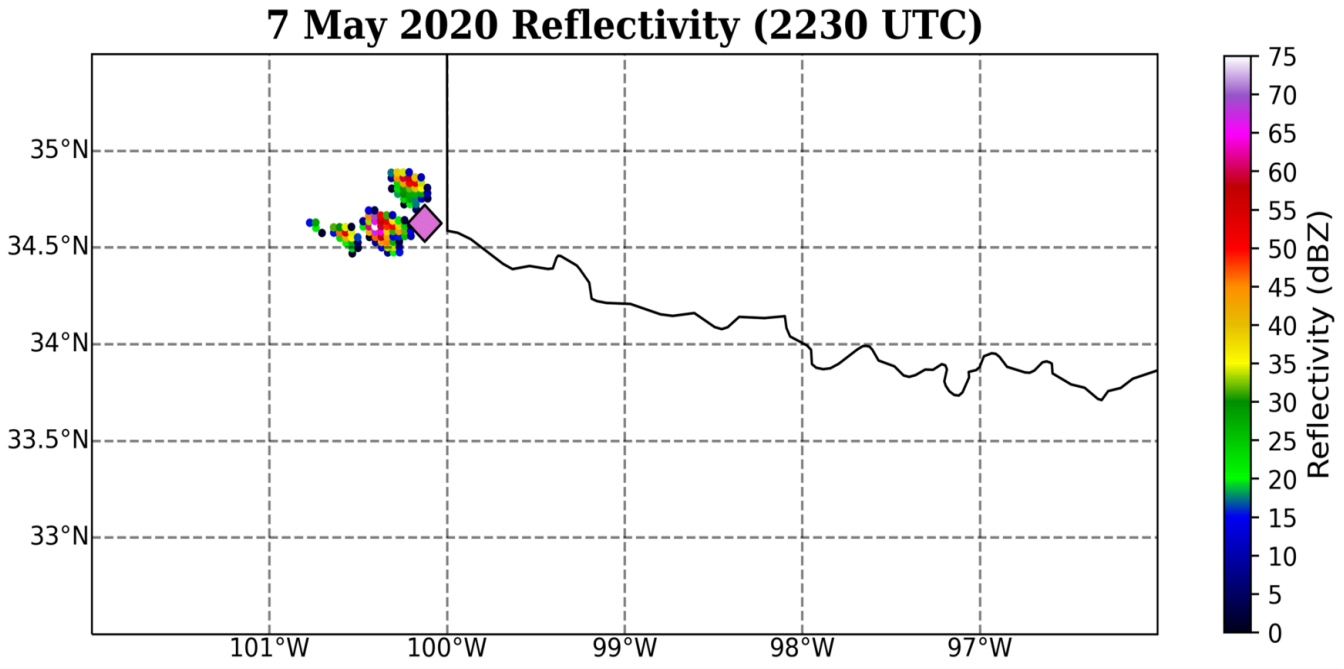

Figure 5.2: 2230 UTC assimilated reflectivity observations in dBZ at 1 km. Transmitter location shown with the purple diamond.

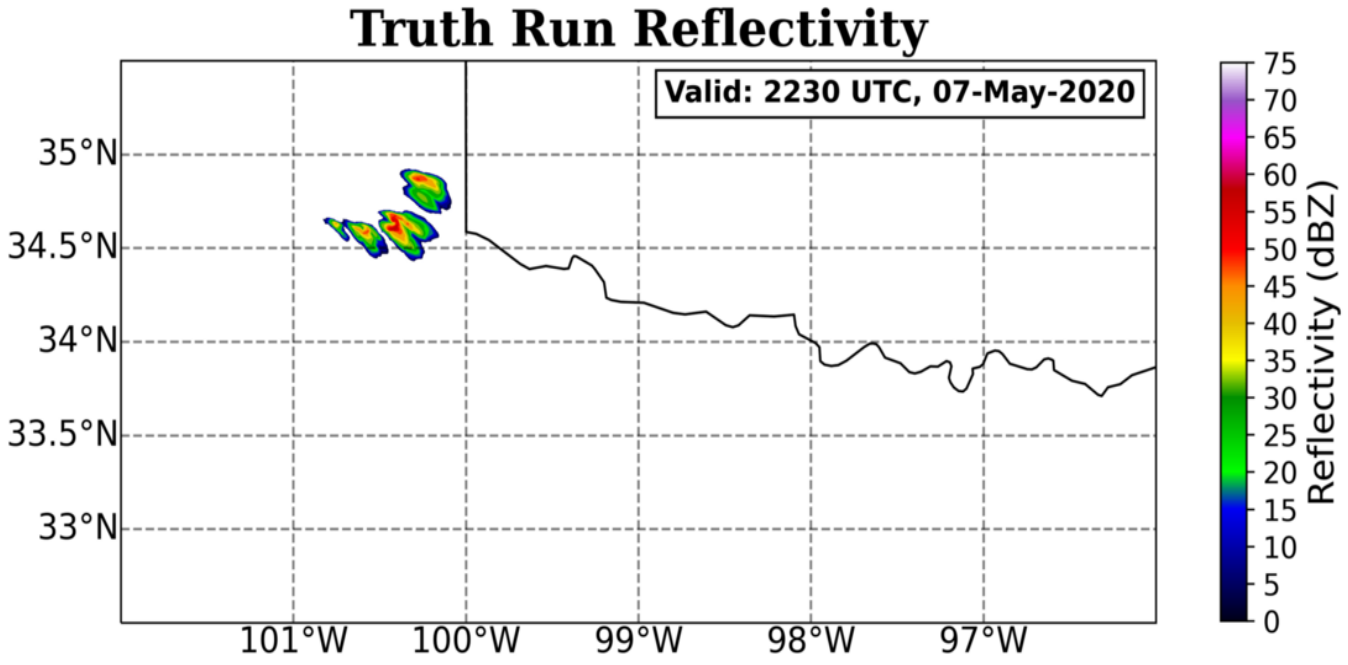

Figure 5.3: 2230 UTC Truth Run reflectivity in dBZ.

5.2 Analysis Plans and Data Issues

Three variables are analyzed for this experiment: radar reflectivity, maximum vertical velocity, and probability swaths of 2 to 5-km updraft helicity (Kain et al. 2008). Reflectivity analyses are conducted for the lowest level within the WoFS domain, while maximum vertical velocity is the maximum upward motion within a column. For the reflectivity and maximum vertical velocity analysis, special attention is paid to the ensemble analyses for each experiment, as this is time where the largest impact from assimilating observations from the multistatic network occurs. Subjective analysis and correlation coefficient analysis (CCA) are used for both radar reflectivity and maximum vertical velocity for two separate experiments: Multistatic vs Truth Run and Multistatic vs WSR-88D Only. Reflectivity and maximum vertical velocity analysis are additionally performed from forecast initialization until 0200 UTC on 8 May, regardless of when the model run ends. All valid times after 0200 UTC for forecasts are ignored because the Truth Run terminates at 0200 UTC. Subjective analysis of reflectivity and maximum vertical velocity in the experimental forecasts are compared to the raw, 250-m Truth Run, as well as the interpolated, 3-km Truth Run. CCA only compares the experimental run to the interpolated Truth Run, owing to the raw Truth Run having a different horizontal grid spacing than the experimental runs. The interpolated Truth Run is created using a nearest-neighbor interpolation method that fits the 250-m Truth Run to a 3-km grid, in order to facilitate comparison to the experimental runs.

For 2 to 5-km updraft helicity (UH) probability swath analysis, only subjective analysis is used, and all probability swaths are analyzed between forecast initialization and 0200 UTC on 8 May. UH is calculated by multiplying the vertical component of

relative vorticity and vertical velocity, then integrating over a desired layer (e.g., 2 to 5 km), as described in Kain et al. (2008).

A neighborhood of 9 km, 15 km, or 27 km diameters are available to use, with the 9 km neighborhood providing the least smoothing for UH swaths (Schwartz and Sobash 2017). Schwartz and Sobash (2017) and Roberts et al. (2019) discuss the neighborhood maximum ensemble probability (NMEP), which is a technique for spreading information in CAMs to produce more representative probabilistic forecasts. NMEP is calculated by assigning the maximum value within a specified neighborhood (9, 15, or 27 km diameter) to every grid point within that neighborhood. Once the maximum value filter has been applied, the grid point probability is calculated for the ensemble and smoothed using a Gaussian filter (Schwartz and Sobash 2017). Real-time WoFS produces a UH probability swath at the end of each forecast, which can be used to assess ensemble confidence in a strong mesocyclone occurring within the domain.

At the initialization of the 2200 UTC forecast, only one DA cycle has occurred, and no radial or bistatic observations are produced for assimilation. There are no returns for any receiver at any elevation angle. However, there is a small reflectivity return at this time as shown in Figure 5.4, which shows all reflectivity observations at all elevations. However, there are no reflectivity returns at 1 km (Figure 5.5). The 2200 UTC time is roughly the beginning of convection initiation within the Truth Run. The Truth Run reflectivity is only compared to the experimental reflectivity at the lowest level. Therefore, the higher-level reflectivity returns seen in Figure 5.4 do not appear in the low levels of the Truth Run (Figure 5.5), but they are still assimilated at 2200 UTC. As a result, an incipient storm is analyzed in the experimental domains. The Multistatic experiment and the WSR-88D Only experiment both assimilate the same reflectivity observations, but not bistatic velocity observations. Therefore, at 2200 UTC when only reflectivity observations are assimilated, the Multistatic experiment and the WSR-88D

Only experiment are identical. For this reason, the 2200 UTC forecast is ignored for the remainder of this thesis.

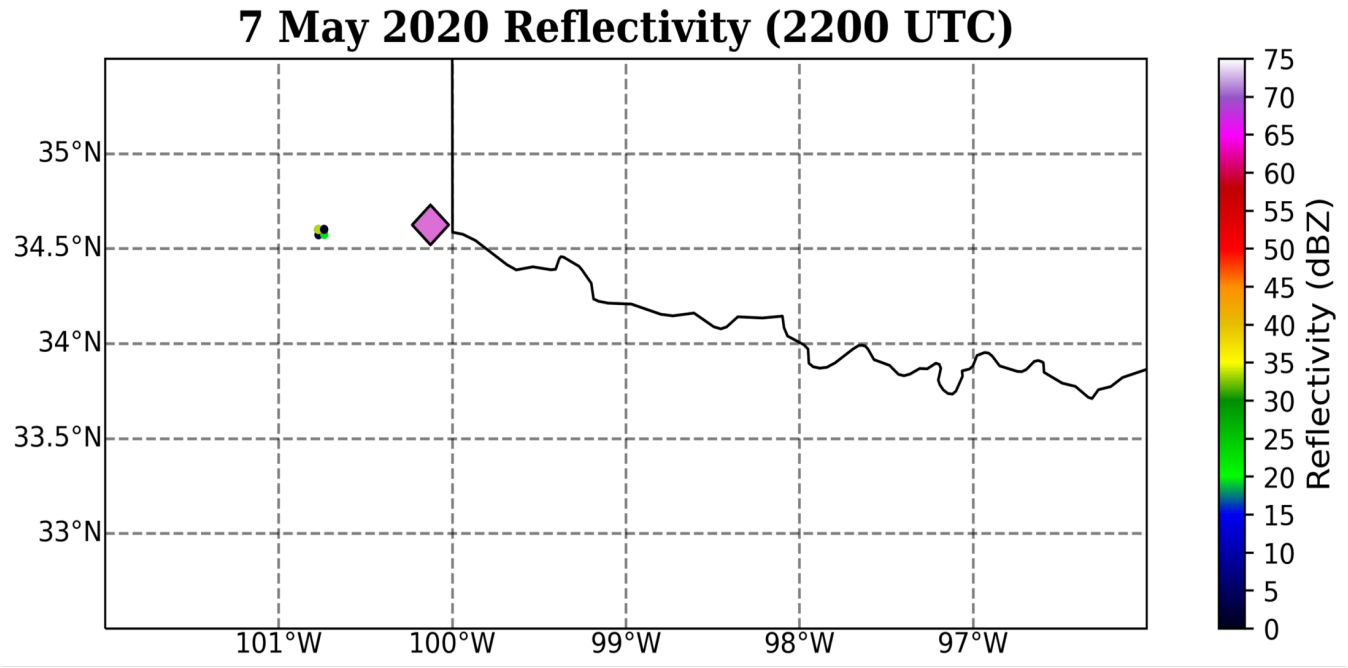

Figure 5.4: 2200 UTC assimilated reflectivity observations in dBZ for all elevations. Transmitter location shown with the purple diamond.

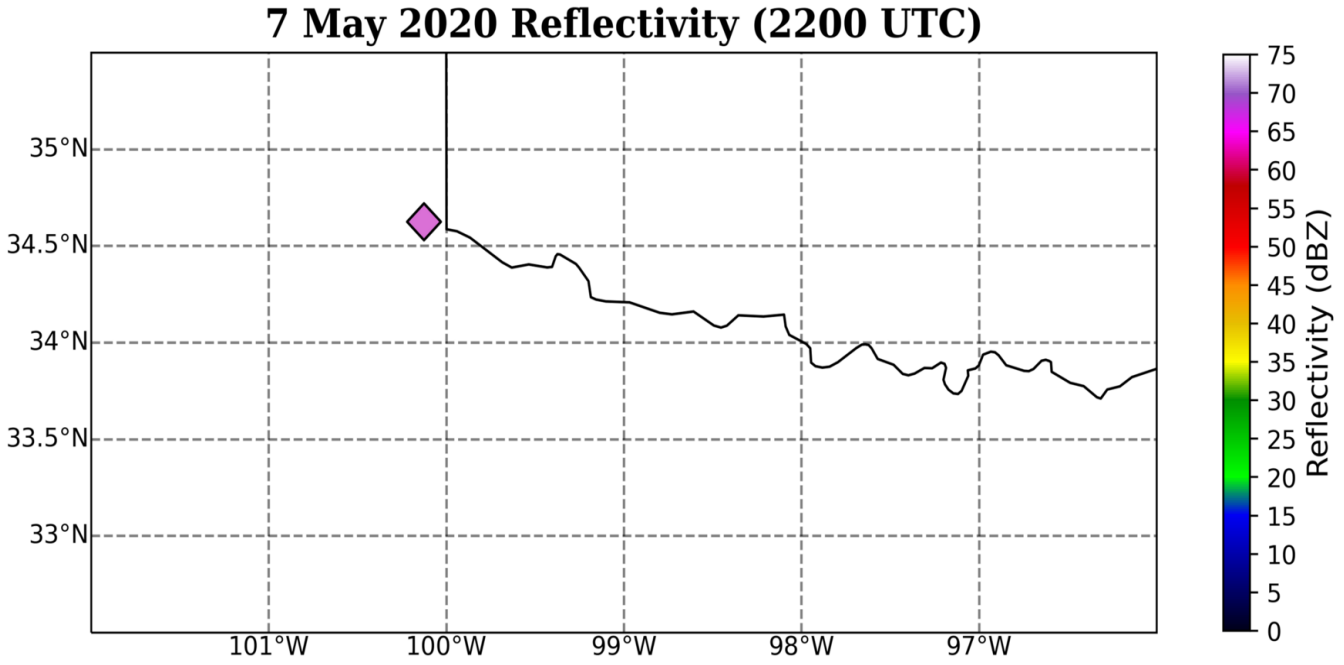

Figure 5.5: As in Figure 5.4, but only for the 1 km elevation.

5.3 Multistatic vs Truth Run

5.3.1 Reflectivity Analysis

5.3.1.1 Ensemble Analyses

A summary of all ensemble analyses CCs and r^2 values for every member for every initialization of the Multistatic experiment are shown in Tables 5.1 and 5.2, with a summary of the member average CCs and r^2 values in Table 5.3, and supplemental bar-graph representation for easier comparisons in Figures 5.6 and 5.7. The 2215 UTC analysis follows two DA cycles including the first non-zero bistatic velocity observations assimilated from the multistatic network. There are differences in the reflectivity fields of the Truth Run and Multistatic simulations in both subjective analysis (Figure 5.8) and in CCA for the 2215 UTC analysis. By this time, there are more extensive reflectivity returns in the Truth Run, which are analyzed in the Multistatic experiment. The Truth Run storm exhibits maximum reflectivity values around 35 dBZ with weaker returns in the Multistatic analysis of only around 10 dBZ in all members. Only a few members show reflectivity returns over 15 dBZ, but the returns are in the proper location when compared to the Truth Run. The highest correlation to the Truth Run is in Member 3, which has a CC value 0.754 and a r^2 value of 56.1%. Conversely, Member 2 is the least correlated member with a CC of 0.082 and a r^2 value of 0.7%, which suggests that the Multistatic member is not similar to the Truth Run at all. Member 3 is also not similar to the Truth Run, with the r^2 value of 56.1% (Figure 5.8). One important note in Figure 5.8, the Truth Run is the Interpolated Truth Run, so the returns are smoothed relative to the raw Truth Run because of the interpolation. Member 2 analyzes a larger area of reflectivity than either Member 3 or Member 15,

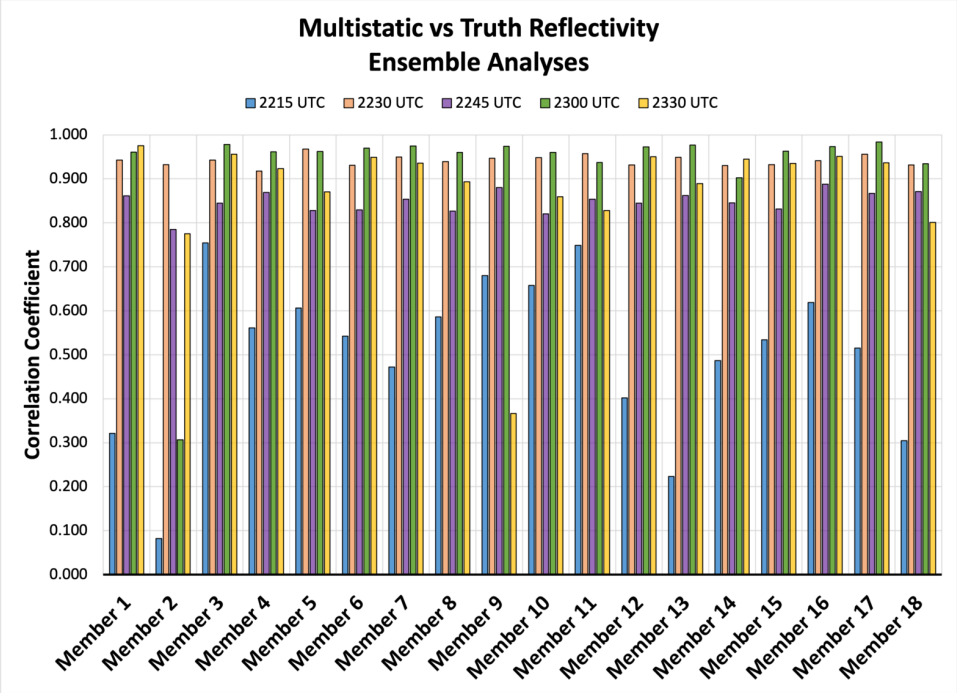

Figure 5.6: Correlation Coefficients for each member for the ensemble analyses from 2215 (blue), 2230 (orange), 2245 (purple), 2300 (green), and 2330 (yellow) UTC.

the member closest to the median CC value for the 2215 UTC analysis. Member 3 produces more compact returns in a location that matches the location of the Truth Run. The larger expanse of reflectivity values in the Multistatic members results from the Multistatic members not filtering out reflectivity values below 20 dBZ like the Truth Run. Therefore, the Multistatic storm may be more expansive than the Truth Run storm, but the cores of highest reflectivity are located in a nearly identical location to the Truth Run. Additionally, while the reflectivity in the Multistatic experiment is much weaker than the Truth Run at this time, this is expected as Guerra et al. (2022) found that it takes 4-6 DA cycles to properly spin up a storm and Snyder and Zhang (2003) found that the EnKF requires 7 DA cycles to properly spin up a storm.

	2215 UTC	**2230 UTC**	**2245 UTC**	**2300 UTC**	**2330 UTC**
Mem 1	0.321	0.942	0.861	0.961	0.975
Mem 2	0.082	0.932	0.785	0.306	0.775
Mem 3	0.754	0.942	0.844	0.978	0.956
Mem 4	0.561	0.918	0.869	0.961	0.923
Mem 5	0.606	0.967	0.828	0.962	0.871
Mem 6	0.543	0.931	0.829	0.970	0.949
Mem 7	0.472	0.949	0.854	0.975	0.936
Mem 8	0.586	0.939	0.827	0.960	0.893
Mem 9	0.680	0.947	0.880	0.974	0.367
Mem 10	0.658	0.948	0.821	0.960	0.860
Mem 11	0.749	0.957	0.854	0.937	0.828
Mem 12	0.402	0.931	0.845	0.973	0.951
Mem 13	0.223	0.949	0.862	0.977	0.889
Mem 14	0.487	0.930	0.845	0.902	0.945
Mem 15	0.534	0.932	0.832	0.963	0.935
Mem 16	0.619	0.941	0.888	0.973	0.951
Mem 17	0.515	0.956	0.867	0.984	0.936
Mem 18	0.304	0.932	0.871	0.934	0.801

Table 5.1: Ensemble analyses correlation coefficients for the Multistatic vs Truth Run reflectivity. WoFS members are labeled in the left-most column.

	2215 UTC	**2230 UTC**	**2245 UTC**	**2300 UTC**	**2330 UTC**
Mem 1	10.3%	88.8%	74.1%	92.3%	95.1%
Mem 2	0.7%	86.9%	61.5%	9.4%	60.1%
Mem 3	56.9%	88.8%	71.3%	95.6%	91.3%
Mem 4	31.5%	84.2%	75.5%	92.4%	85.3%
Mem 5	36.7%	93.6%	68.5%	92.5%	75.8%
Mem 6	29.4%	88.6%	68.7%	94.0%	90.0%
Mem 7	22.3%	90.2%	72.9%	95.0%	79.8%
Mem 8	34.3%	88.2%	68.4%	92.2%	79.8%
Mem 9	46.2%	89.7%	77.4%	94.9%	13.4%
Mem 10	43.3%	89.9%	67.3%	92.2%	73.9%
Mem 11	56.1%	91.6%	72.9%	87.8%	68.5%
Mem 12	16.2%	86.7%	71.3%	94.6%	90.4%
Mem 13	5.0%	90.0%	74.3%	95.4%	79.1%
Mem 14	23.7%	86.5%	71.4%	81.4%	89.3%
Mem 15	28.5%	87.0%	69.2%	92.6%	87.4%
Mem 16	38.3%	88.6%	78.8%	94.7%	90.5%
Mem 17	26.5%	91.4%	75.1%	96.8%	87.6%
Mem 18	9.3%	86.8%	75.9%	87.3%	64.1%

Table 5.2: Ensemble analyses r^2 values for the Multistatic vs Truth Run reflectivity. WoFS members are labeled in the left-most column.

	Average CC	**Average r^2**
Mem 1	0.812	65.9%
Mem 2	0.576	33.2%
Mem 3	0.895	80.1%
Mem 4	0.847	71.7%
Mem 5	0.847	71.7%
Mem 6	0.844	71.2%
Mem 7	0.837	70.1%
Mem 8	0.841	70.7%
Mem 9	0.770	59.2%
Mem 10	0.849	72.1%
Mem 11	0.865	74.8%
Mem 12	0.820	67.3%
Mem 13	0.780	60.8%
Mem 14	0.822	67.5%
Mem 15	0.839	70.4%
Mem 16	0.874	76.4%
Mem 17	0.852	72.5%
Mem 18	0.768	59.1%

Table 5.3: Member average corrrelation coefficients and r^2 values for all ensemble analyses of the Multistatic vs Truth Run reflectivity. WoFS members are labeled in the left-most column, followed by correlation coefficients, and then r^2 values.

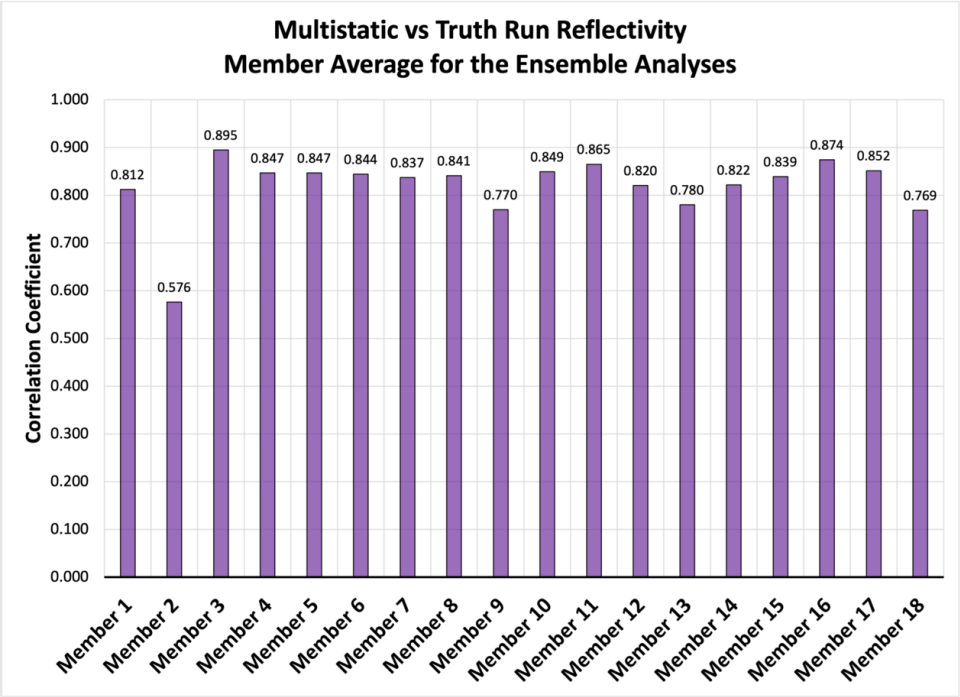

Figure 5.7: Member average correlation coefficient for ensemble analyses of the Multistatic vs Truth Run reflectivity for all initializations.

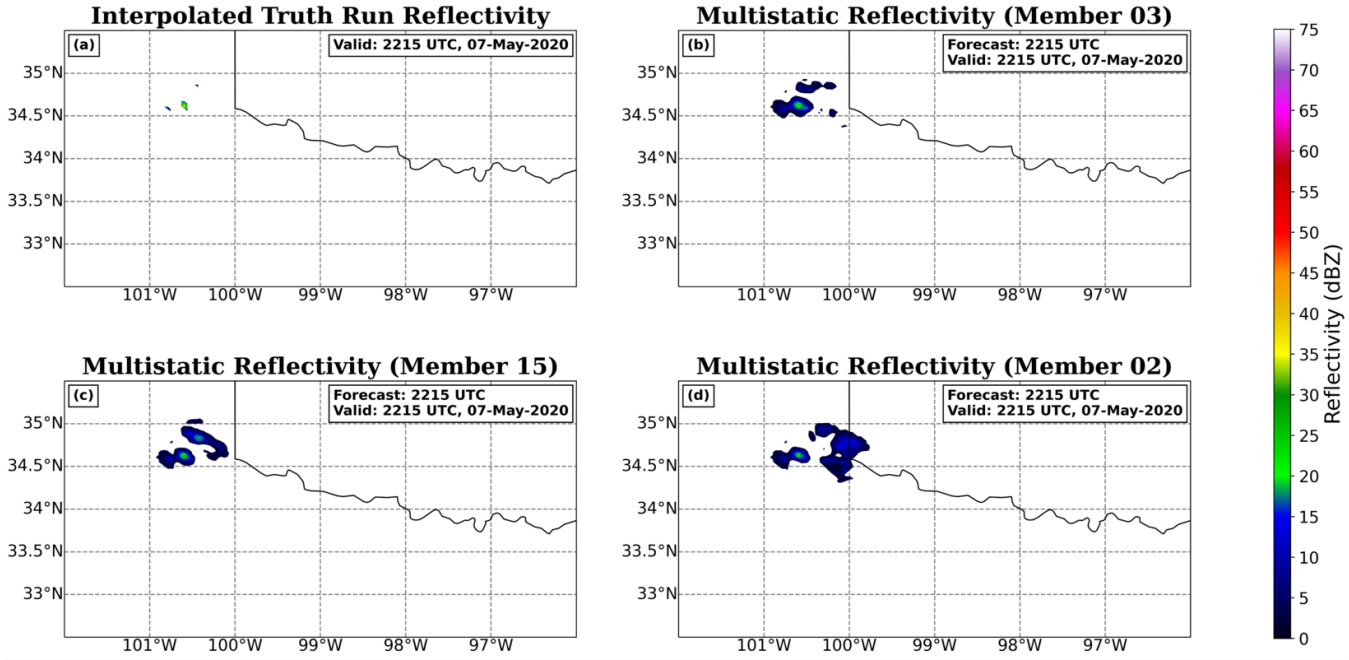

Figure 5.8: (a) Interpolated Truth Run reflectivity (dBZ) at 2215 UTC on 7 May 2020. For the 2215 UTC ensemble analysis, the best performing member (b) Member 3, CC of 0.754, the median performing member (c) Member 15, CC of 0.534 (median: 0.532), and the worst performing member (d) Member 2, CC of 0.082 reflectivity is plotted.

Three DA cycles are complete at the initialization of the 2230 UTC forecast and the Multistatic experiment is more strongly correlated with the Truth Run (Figure 5.6). Returning to Figure 5.1, many more observations are assimilated at this time across all receivers and all elevation angles than were assimilated for the 2215 UTC analysis. It is evident the multistatic network observations are having a larger impact on the analyses and the analyses are more accurate owing to additional DA cycles. Member 5 has the highest correlation to the Truth Run with a CC of 0.967 and a r^2 value of 93.6%. The lowest correlated member, Member 4, is only slight further behind with a CC of 0.918 and a r^2 value of 85.2%. Higher CC and r^2 values for this forecast show that the Multistatic members' reflectivity are similar to the Truth Run at this time, which is further supported by the subjective analysis. The reflectivity in the Multistatic members is slightly weaker than the Truth Run, which is true for most analyses. However, the Multistatic storms have a more round and continuous shape, while the Truth Run has three distinct reflectivity cores (Figure 5.9). The location of the Multistatic reflectivity is similar to that of the center reflectivity core in the Truth Run. The median member looks similar to the best member and the worst member, neglecting the regions of spurious reflectivity in the worst member. It is evident that after only 3 cycles, the data assimilation system is producing an accurate analysis of the storm at this time and is better suppressing the spurious convection.

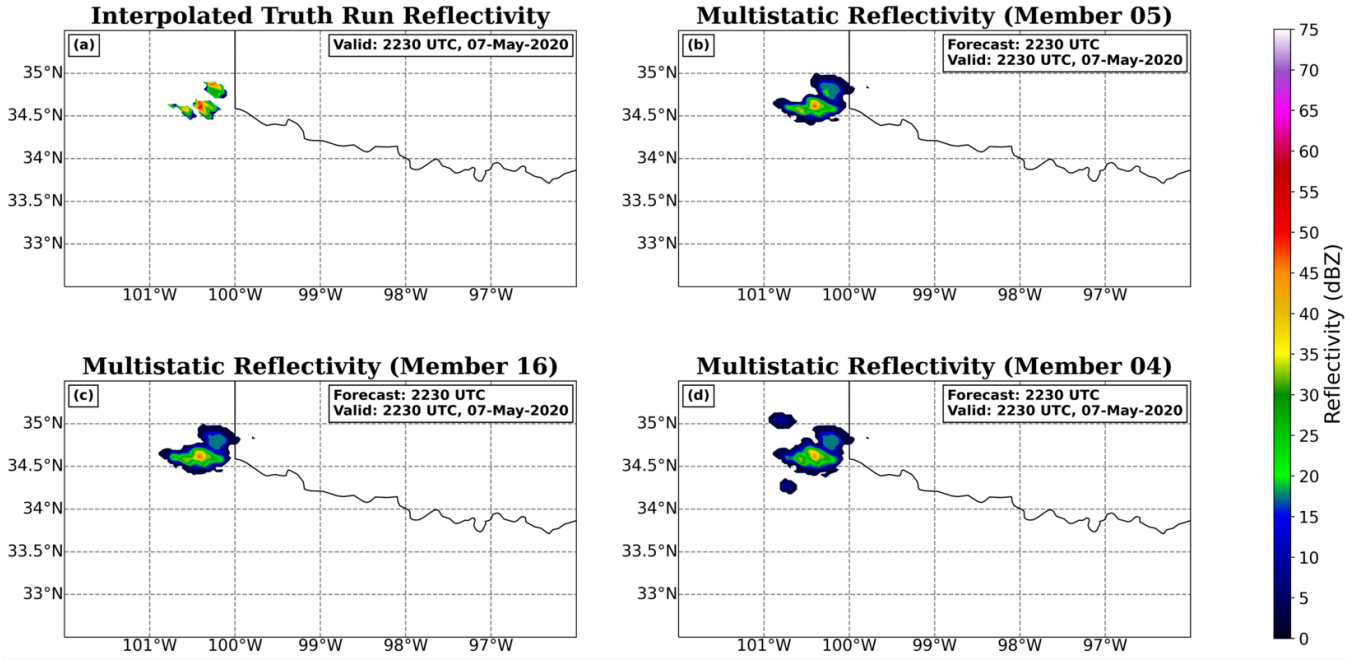

Figure 5.9: (a) Interpolated Truth Run reflectivity (dBZ) at 2230 UTC on 7 May 2020. For the 2230 UTC ensemble analysis, the best performing member (b) Member 5, CC of 0.967, the median performing member (c) Member 16, CC of 0.9413 (median: 0.9418), and the worst performing member (d) Member 4, CC of 0.918 reflectivity is plotted.

Interestingly, the CCs for the 2245 UTC ensemble analyses drops significantly for all members, despite including four DA cycles (Figure 5.6). The highest correlation occurs in Member 16 with a CC of 0.888 and a r^2 value of 77.4%. The lowest correlated member, Member 2, has a CC of 0.785 and a r^2 value of 61.5%. Therefore, the Multistatic members are less similar to the Truth Run at this time. Subjective analysis suggests that the CC drop results from an increase in the areal extent of the Multistatic reflectivity (Figure 5.10). This increased extent is caused by reflectivity values < 20 dBZ, which do not appear in the Truth Run. Additionally, Member 2 has some spurious convection to the south, which likely caused the lower CC. The difference in reflectivity values is difficult to see by only looking at the two reflectivity fields and comparing them, but it is easier to see with reflectivity difference plots between the Truth Run and the Multistatic experiment (Figure 5.11). The Multistatic reflectivity core and the Truth Run reflectivity core are well aligned at this time, but the Truth Run has an additional core to the north, along the Oklahoma and Texas Panhandle border. This northern storm appears as the positive values in Figure 5.11, while regions near the core of the primary storm have a value near zero, which shows that the Multistatic experiment and the Truth Run have similar reflectivity strengths for the developing target supercell. Only 6 of the 18 Multistatic members at this time have a r^2 value under 70%, which suggests that these members do not match the Truth Run as well as the other members (Table 5.2). However, the subjective analysis suggests that the lower-correlated members are driven by spurious reflectivity to the south of the main storm and an expansion of the low reflectivity field around the storm, but the primary storm matches the Truth Run well and these members produce accurate analyses of the primary storm.

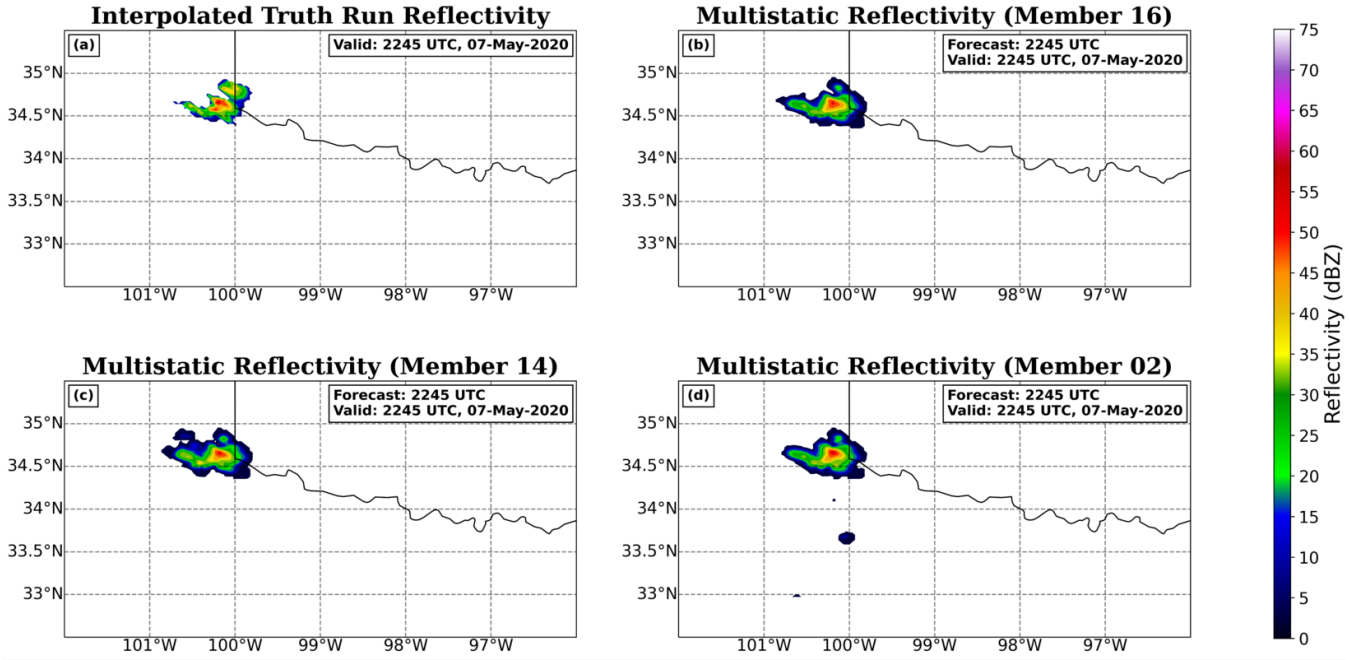

Figure 5.10: (a) Interpolated Truth Run reflectivity (dBZ) at 2245 UTC on 7 May 2020. For the 2245 UTC ensemble analysis, the best performing member (b) Member 16, CC of 0.888, the median performing member (c) Member 14, CC of 0.845 (median: 0.849), and the worst performing member (d) Member 2, CC of 0.785 reflectivity is plotted.

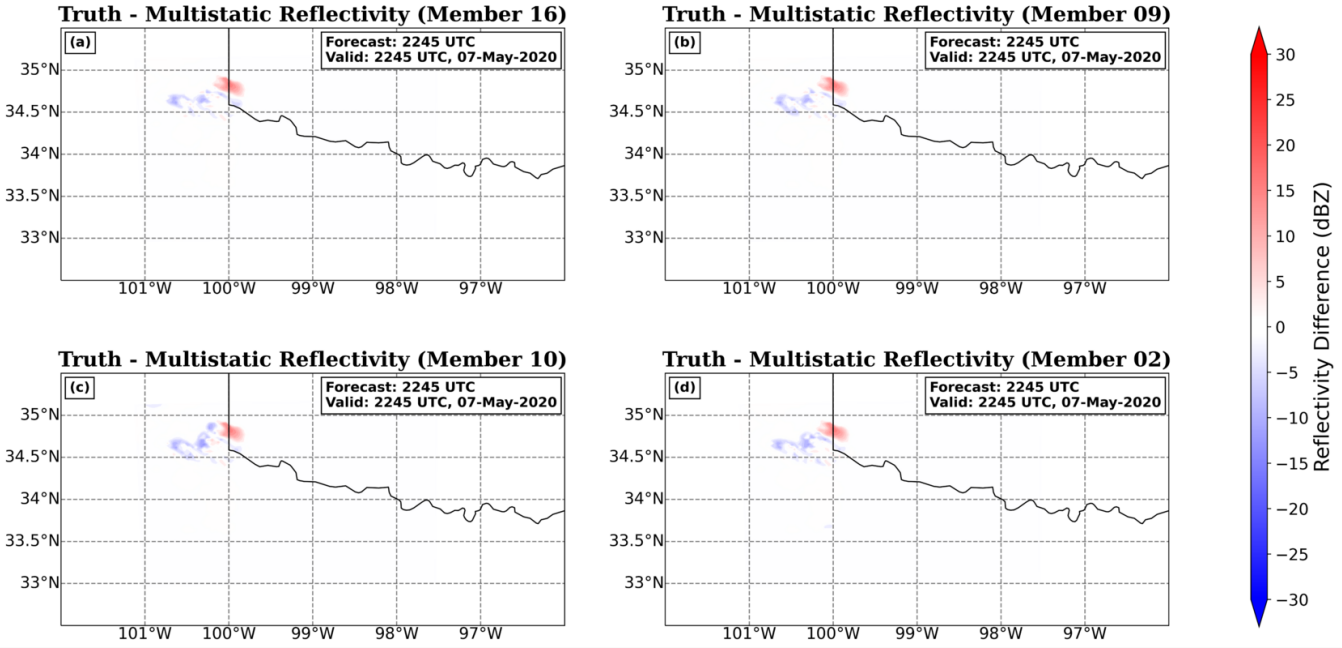

Figure 5.11: 2245 UTC ensemble analyses Truth Run reflectivity minus Multistatic member reflectivity for the 2 best performing members: (a) Member 16, CC of 0.888 and (b) Member 9, CC of 0.880, as well as the 2 worst performing members: (c) Member 10, CC of 0.821 and (d) Member 2, CC of 0.785. All reflectivity differences are in dBZ.

After 5 DA cycles, the 2300 UTC ensemble analyses continues to match the Truth Run closely in a majority of the members; however, a few members drop off significantly with their correlation to the Truth Run (Figure 5.6). The best correlated member is Member 17 with a CC of 0.984 and a r^2 value of 96.8%. However, Member 2 drops off significantly from the previous forecast. For the 2245 UTC forecast, Member 2 had a correlation of 0.785, but in the 2300 UTC forecast the CC drops to 0.306 (r^2 value of 9.4%). Despite this, Table 5.2 shows that a majority of members are over a r^2 values of 90%, with only four members falling below this threshold and only one member with a r^2 lower than 80%. In contrast, 13 of the 17 members have their highest correlation to the Truth Run for the 2300 UTC ensemble analyses. Therefore, this analysis is the most accurate analysis for the majority of members in terms of correlation between the Multistatic and Truth Run reflectivity fields. The skill of this analysis is further seen when examining the reflectivity field (Figure 5.12). The Multistatic members accurately analyze storm intensity and location. In fact, the poor CC for Member 2 appears to be caused by the spurious convection to the south, rather than the analysis of the main storm. The reflectivity differences between the Truth Run and the Multistatic members are relatively similar across all members, even Member 2 (Figure 5.13). However, Member 2 clearly shows the spurious convection to the south, indicated by stronger negative values. This spurious convection is not as prominent in the other members. One important note about this 2300 UTC ensemble analyses is that at the start of this forecast, the storm is beginning to split, which complicates the forecast significantly. However, the Multistatic experiment has its best ensemble analyses for the 2300 UTC initialization, even during a complex situation such as a splitting storm.

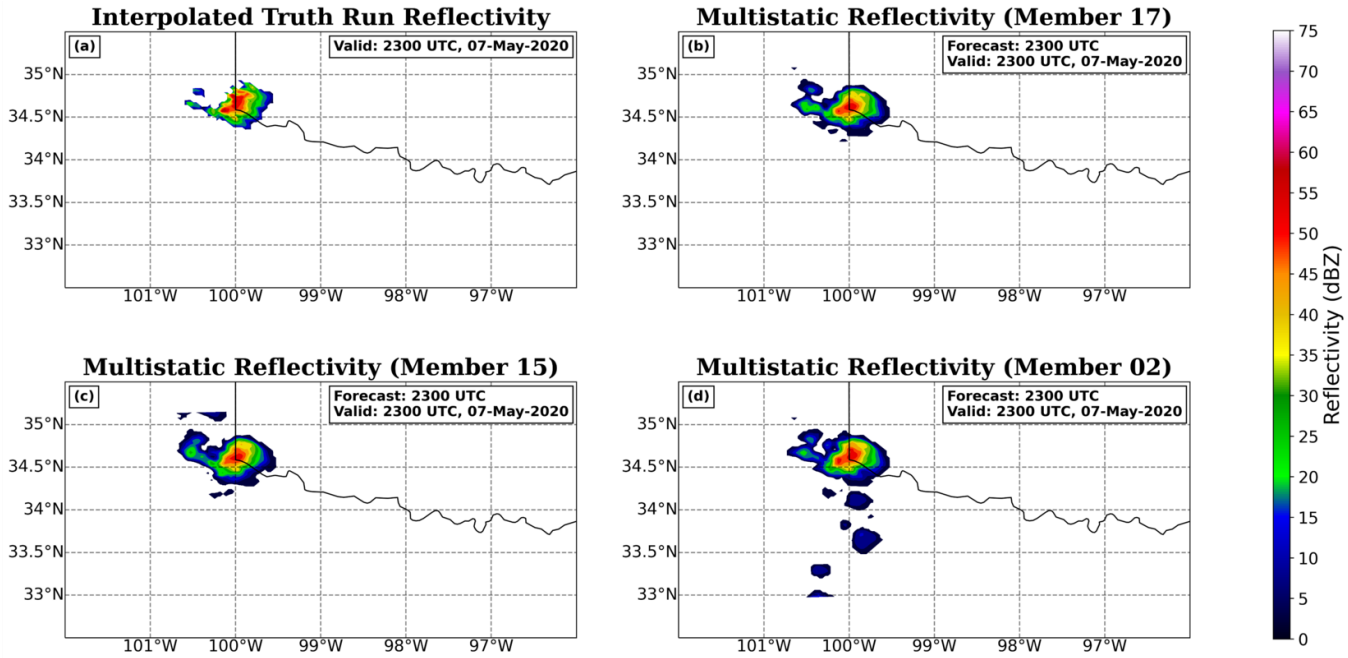

Figure 5.12: (a) Interpolated Truth Run reflectivity (dBZ) at 2300 UTC on 7 May 2020. For the 2300 UTC ensemble analysis, the best performing member (b) Member 17, CC of 0.984, the median performing member (c) Member 15, CC of 0.963 (median: 0.962), and the worst performing member (d) Member 2, CC of 0.306 reflectivity is plotted.

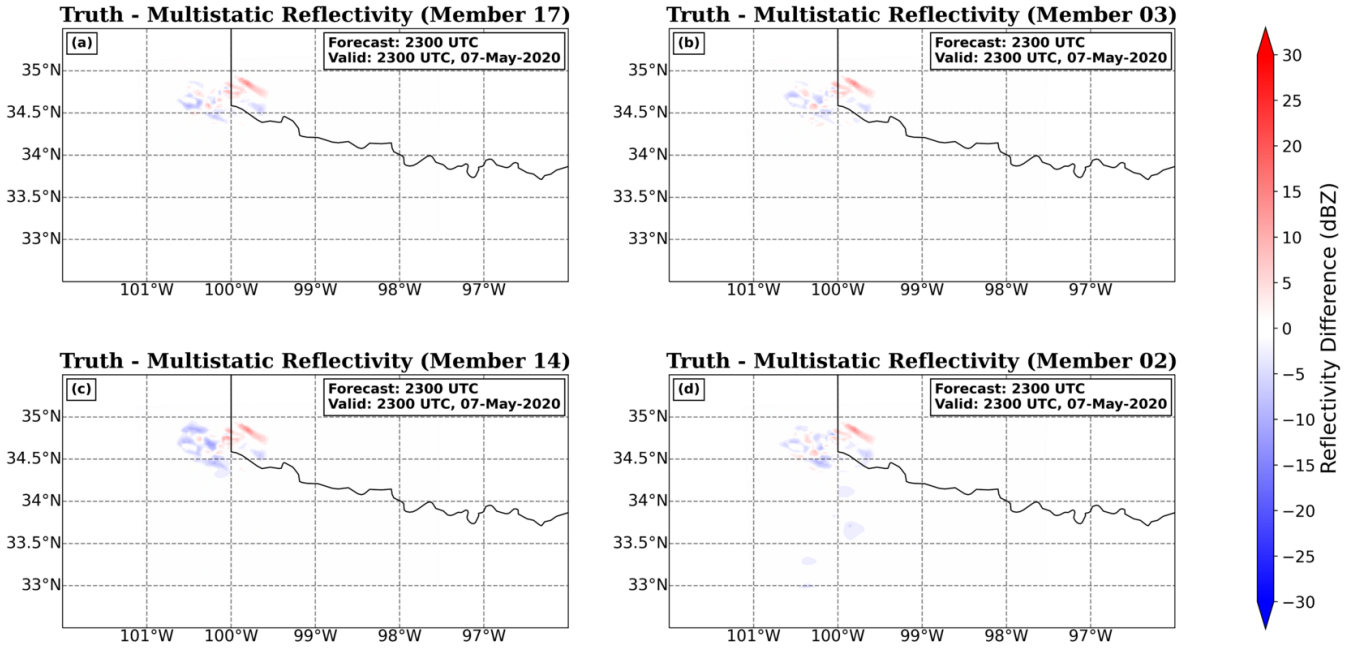

Figure 5.13: 2300 UTC ensemble analyses Truth Run reflectivity minus Multistatic member reflectivity for the 2 best performing members: (a) Member 17, CC of 0.984 and (b) Member 3, CC of 0.978, as well as the 2 worst performing members: (c) Member 14, CC of 0.902 and (d) Member 2, CC of 0.306. All reflectivity differences are in dBZ.

The 2330 UTC forecast initializes after the supercell has split and includes 7 DA cycles, the maximum number of DA cycles for forecasts initiated in this experiment. Due to this evolution, in the 2330 UTC ensemble analyses the Multistatic members are forced to properly analyze the left-split and right-split of the supercell. Reflectivity analysis shows that the Multistatic members accurately produce the split and the right-split matches the shape and location of the Truth Run's right-split. However, much like the 2300 UTC forecast, the right-split is weaker than the Truth Run. Additionally, the left-split in the Multistatic members is weaker than the left-split in the Truth Run, but the Multistatic members accurately analyze the shape and location of the left split. Member analyses reveal some spurious convection to the south of the dominant right-split, which does not appear in the Truth Run (Figure 5.14). Most members analyze some reflectivity returns west of the right-split, but these returns are weak. Member 9 is the lowest correlated member, with a CC of 0.367 and a r^2 value of 13.4%, which is significantly lower than the 0.974 correlation in the 2300 UTC ensemble analyses. In fact, a decrease in correlation from the 2300 UTC forecast to the 2330 UTC forecast occurs for 15 of the 18 members. However, Member 1 is the best correlated member with a CC of 0.975 and a r^2 value of 95.1%, which is up from 0.961 from the previous forecast. Only 5 of the 18 members are over the r^2 threshold of 90% with a majority falling between 70% and 90%, whereas for the 2300 UTC ensemble analyses a majority of the members were above the 90% threshold. The degradation of correlation between Multistatic members and the Truth Run from 2300 UTC to 2330 UTC is likely due to the complexity of the storm at this time.

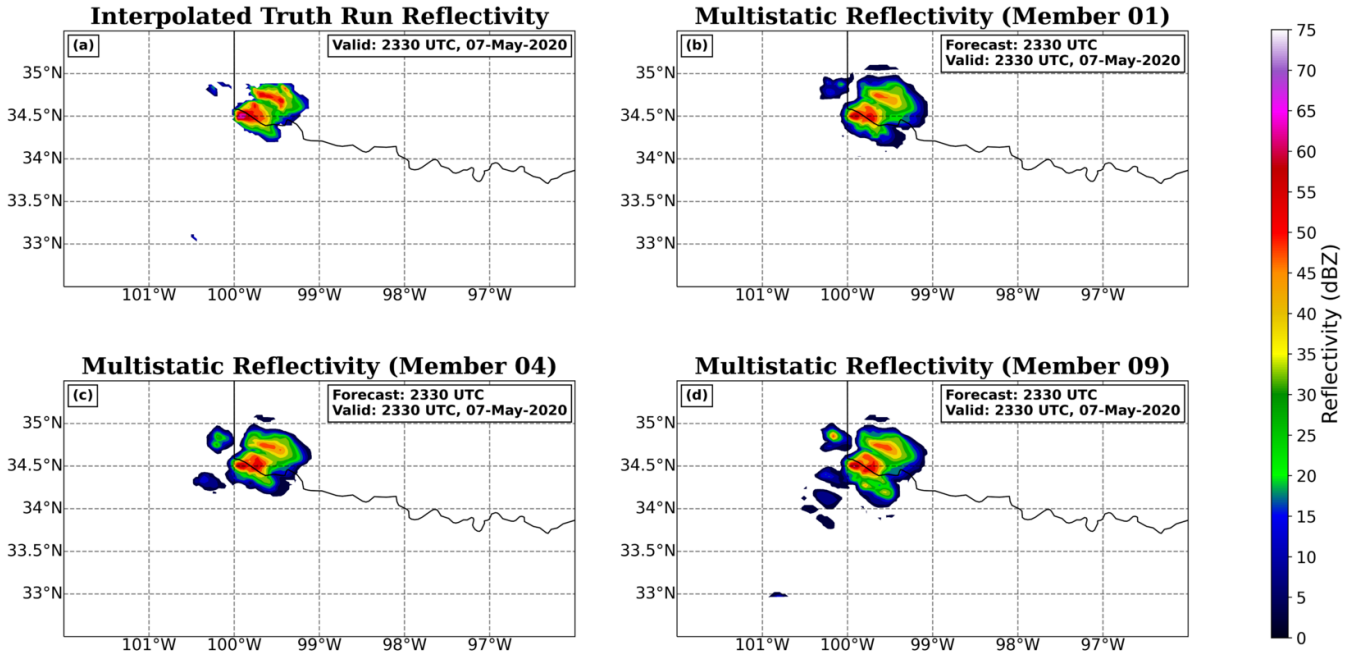

Figure 5.14: (a) Interpolated Truth Run reflectivity (dBZ) at 2330 UTC on 7 May 2020. For the 2330 UTC ensemble analysis, the best performing member (b) Member 1, CC of 0.975, the median performing member (c) Member 4, CC of 0.923 (median: 0.929), and the worst performing member (d) Member 9, CC of 0.367 reflectivity is plotted.

5.3.1.2 Ensemble Forecasts

The crucial time for the ensemble forecasts occurs from 2300 UTC until 0130 UTC, when the storm goes through the split. The storm begins to split at 2300 UTC and by 2330 UTC the storm is completely split with a dominant right-mover and a weaker left-mover (Figures 4.5 and 4.6). The left-mover remains in the domain until 0130 UTC when it dissipates completely in southwestern Oklahoma. The left-spit dissipates to weak reflectivity returns by 0115 UTC but does not completely dissipate until 0130 UTC. The Truth Run appears to have a secondary storm in between the dominant right-mover and the dissipating left-mover from 2350 UTC until 0115 UTC, which is likely a result of the 250-m grid spacing resolving reflectivity cores that are typically smoothed out with 3 km horizontal grid spacing.

A summary of the member average correlation coefficients for each forecast is shown in Figure 5.15. For the 2200 UTC forecast, there were no Doppler velocity observations assimilated, as discussed in previous sections. In conjunction with the lack of bistatic velocity observations and the minimal reflectivity observations, the Multistatic members struggle with the placement and initiation of the actual storm. All members have a storm in the domain at the lowest levels for the start of the 2200 UTC forecast, but there is no reflectivity returns at the lowest levels of the Truth Run (Figure 5.16). Additionally, all members struggle to resolve the storm by 2215 UTC, despite the Truth Run showing reflectivity returns in the lowest levels starting at 2210 UTC and having a more substantial storm by 2215 UTC. Throughout the forecast, the Multistatic members weaken the storm and Members 3, 7, and 16 completely dissipate the storm, even though the Truth Run continues to strengthen the storm. Members 1, 17, and 18 end up producing a line of storms, while Members 6, 11, and 14 strengthen the singular storm and produce an accurate track (Figure 5.17). Few members produce an accurate forecast, evident by the low member average CC values in Figure 5.15.

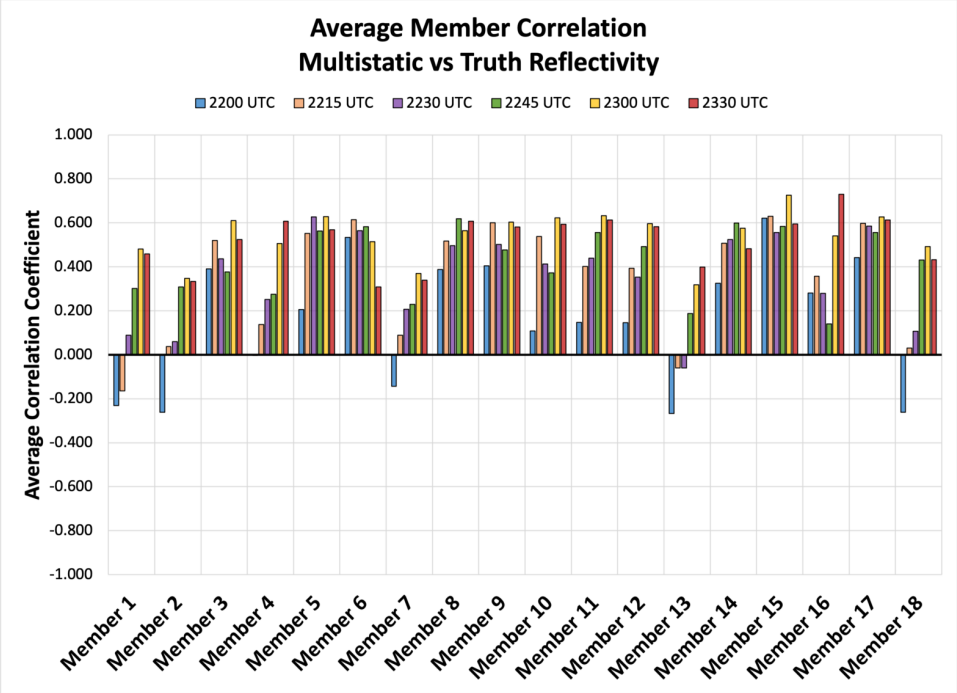

Figure 5.15: Average correlation coefficient for each member for each forecast: 2200 (blue), 2215 (orange), 2230 (purple), 2245 (green), 2300 (yellow), and 2330 UTC (red).

Despite this, there is only one DA cycle at this point and few observations are assimilated; therefore, it is not expected that WoFS will accurately produce a forecast with minimal observations and a poor analysis (Guerra et al. 2022).

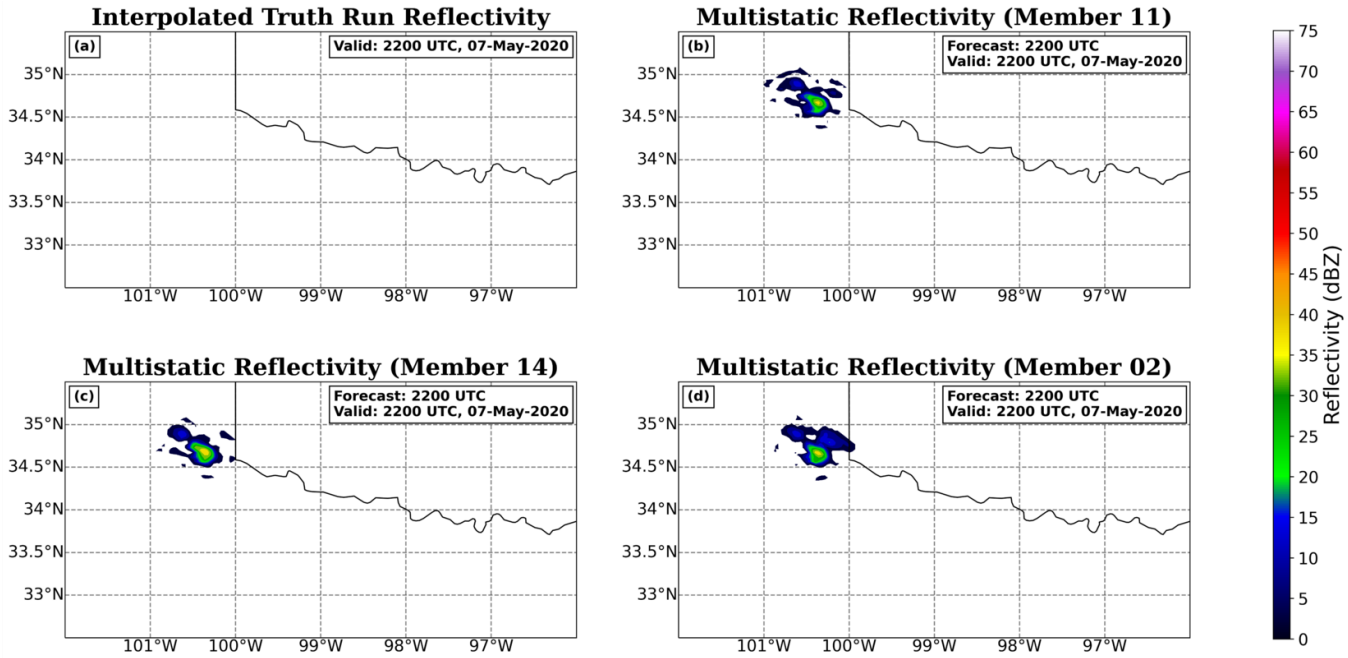

Figure 5.16: (a) Interpolated Truth Run reflectivity (dBZ) at 2200 UTC on 7 May 2020. For the 2200 UTC ensemble analysis, the best performing member (b) Member 11, CC of 0.694, the average performing member (c) Member 14, CC of 0.479 (average: 0.466), and the worst performing member (d) Member 2, CC of 0.053 reflectivity is plotted.

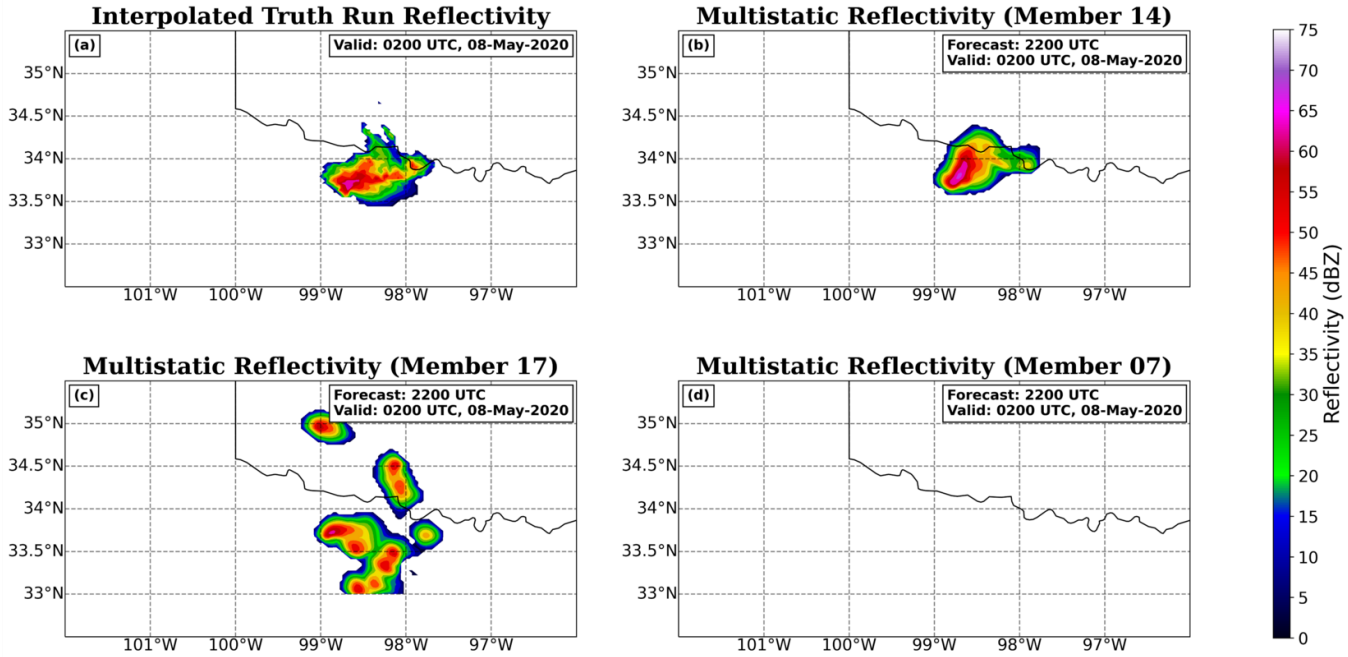

Figure 5.17: (a) Interpolated Truth Run reflectivity (dBZ) at 0200 UTC on 8 May 2020. For the 2200 UTC ensemble forecast at 0200 UTC, an accurate analysis of the storm in (b) Member 14, an example of the line of storms in (c) Member 17, and an example of a member without a storm in (d) Member 7 is plotted.

After 2 DA cycles, the Multistatic members begin to spin-up the storm and match the Truth Run more closely in the 2215 UTC ensemble analyses. Ideally, better initialization results in a better forecast, but this is only slightly supported by the subjective analysis and not overly supported by the CCA. However, this is expected as Guerra et al. (2022) found that storms with a Relative Object Age of 0 to 30 minutes have a lower probability of detection than storms with a larger Relative Object age (Figure 2.5). By 2245 UTC, all members have a single storm in the domain, but the intensity is much higher and more expansive than what the Truth Run shows (Figure 5.18). CCs begin to decrease dramatically around 2300 UTC when the storm begins to split and remain low until 0045 UTC when the left-mover starts to weaken. Following 0045 UTC, as the left-mover dissipates from the Truth Run domain, the CCs begin to rapidly increase once more. Some Multistatic members produce storms with a higher intensity than what is shown in the Truth Run, with several members exceeding 70 dBZ, while the Truth Run reaches about 65 dBZ at 0130 UTC (Figure 5.19). However, it is worth noting that the highest reflectivity value in the Interpolated Truth Run matches the highest reflectivity value in the raw Truth Run, but the extent of the highest reflectivity core is smaller in the Interpolated Truth Run than it is in the raw Truth Run. It is expected that the Multistatic experiment will not perfectly match the Truth Run after only 2 DA cycles, but the Multistatic experiment produces relatively accurately analyses and forecasts of the right-moving supercell despite having less than 4 DA cycles.

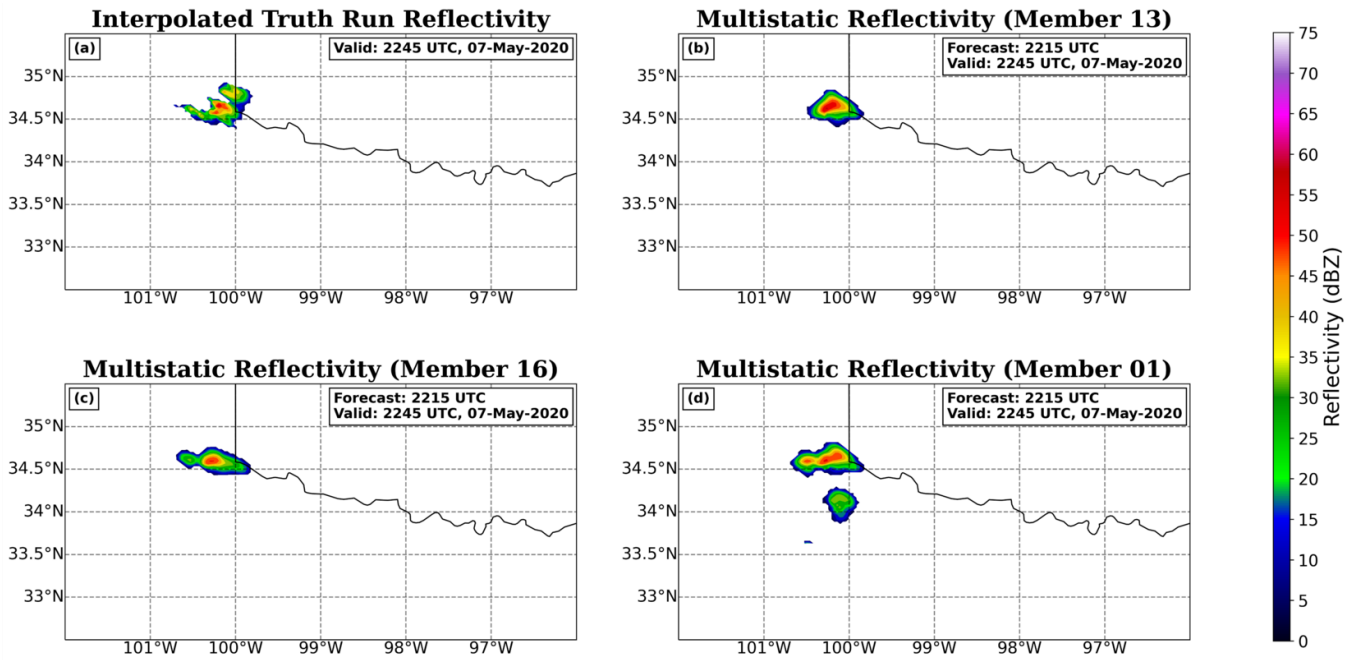

Figure 5.18: (a) Interpolated Truth Run reflectivity (dBZ) at 2245 UTC on 7 May 2020. For the 2215 UTC ensemble forecast at 2245 UTC, the best performing member (b) Member 13, CC of 0.787, the median performing member (c) Member 16, CC of 0.624 (median: 0.618), and the worst performing member (d) Member 2, CC of -0.261 reflectivity is plotted.

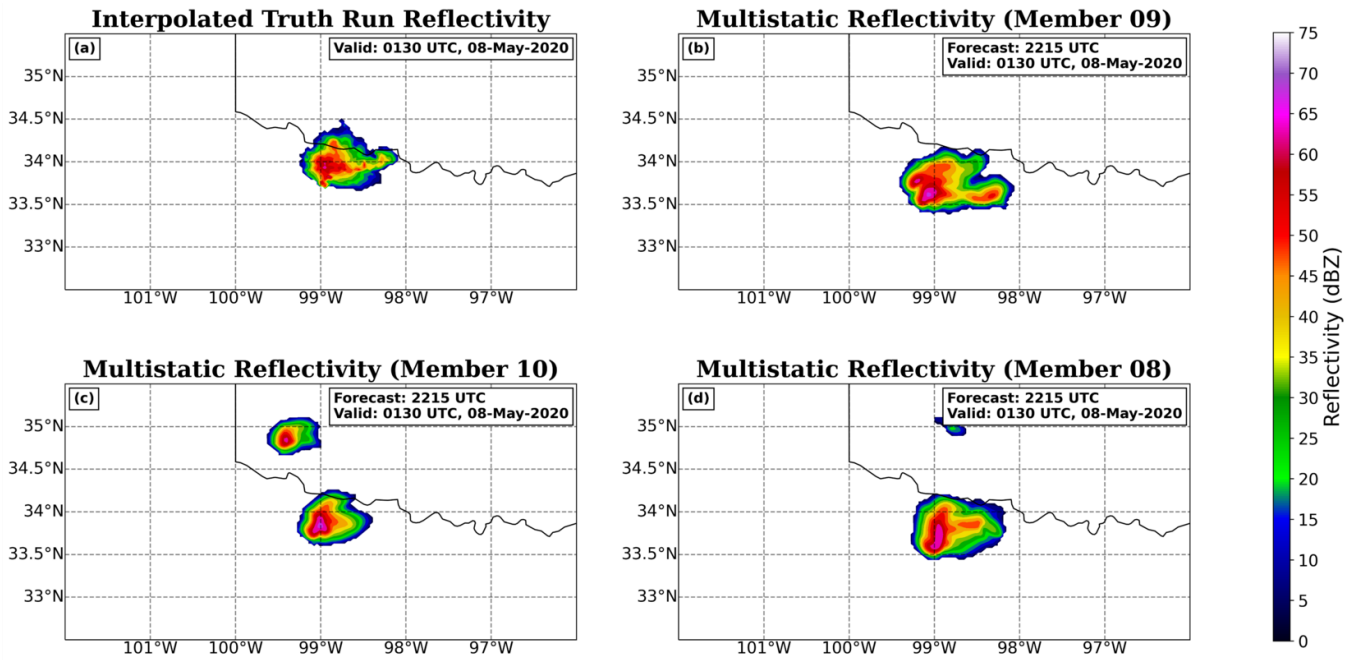

Figure 5.19: (a) Interpolated Truth Run reflectivity (dBZ) at 0130 UTC on 7 May 2020. For the 2215 UTC ensemble forecast at 0130 UTC, the best performing member (b) Member 9, CC of 0.457, the median performing member (c) Member 10, CC of -0.034 (median: -0.032), and the worst performing member (d) Member 8, CC of -0.026 reflectivity is plotted.

With the addition of another DA cycle for the 2230 UTC forecast, a stronger storm is present during the early forecast period in the Multistatic members that matches the intensity of the Truth Run better than the previous forecast. However, Members 7 and 16 hardly maintain any storm in the domain. Member 16 never predicts a splitting storm, and the only storm in the domain dissipates completely by 0045 UTC. Much like the 2215 UTC forecast, the splitting period from 2300 UTC until 0045 UTC features a strong decrease in CC values, but the CCs increase dramatically by 0045 UTC. Once again, the Multistatic forecast is not predicting the split accurately and many members dissipate the left-mover by 2330 UTC, whereas the Truth Run does not dissipate the left-mover until 0130 UTC (Figure 5.20). Ideally, the 2230 UTC forecast should predict the evolution of the split better than the 2215 UTC forecast owing to there being less time between the split and the initialization of the forecast, but this is not the case in this experiment. In fact, the strongest correlation during the period where there is a robust left-mover in the domain in the 2215 UTC forecast was 0.457, while it is only 0.410 in the 2230 UTC forecast. In addition to poorly predicting the evolution of the split, many Multistatic members dissipate the left-mover well before is dissipates in the Truth Run. Similar to the 2215 UTC forecast, the members improve drastically as the left-mover weakens starting at 0045 UTC and continues to produce accurate forecasts during the latter portion of the forecast period when the right-mover is the primary storm in the domain. Overall, the Multistatic members continue to predict dissipation of the left-mover by 2330 UTC, whereas dissipation of the left mover in the Truth Run does not occur until 0130 UTC. Assimilation of the multistatic network observations appears to suppress predictions of the left-mover, but keeps the dominant right-mover in the domain and produces accurate forecasts of the right-mover throughout the forecast.

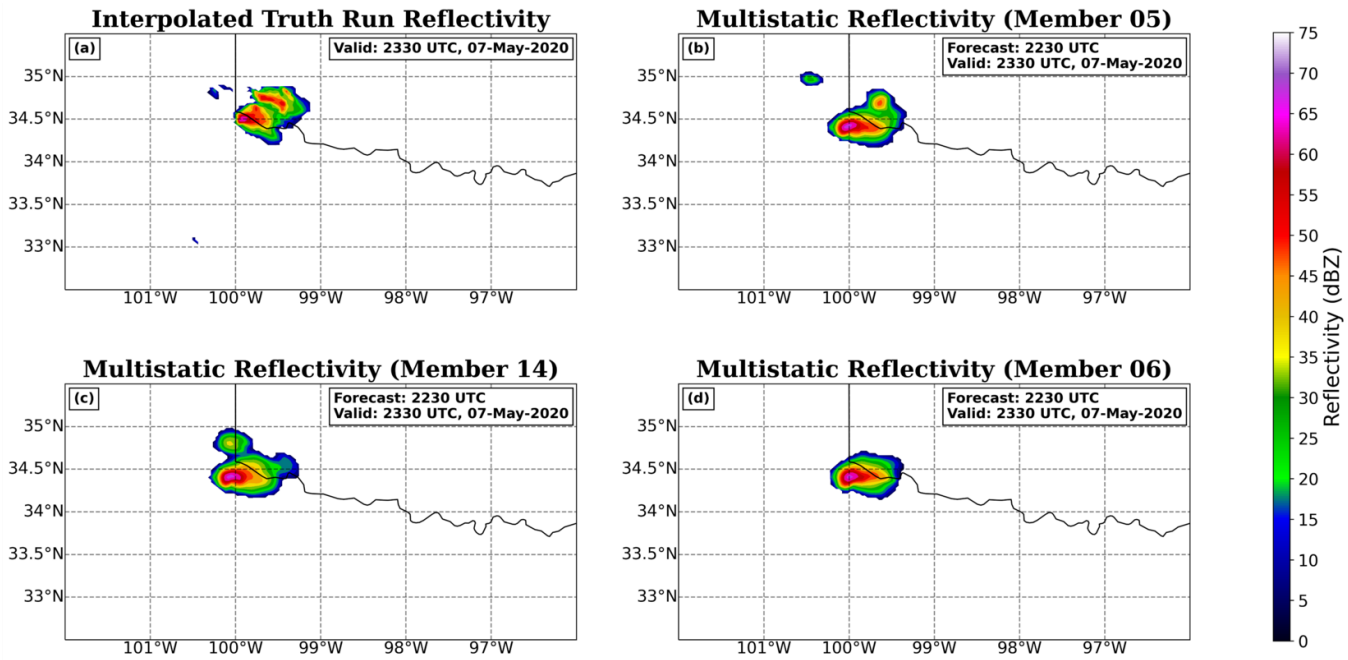

Figure 5.20: (a) Interpolated Truth Run reflectivity (dBZ) at 2330 UTC on 7 May 2020. For the 2230 UTC ensemble forecast at 2330 UTC, the best performing member (b) Member 5, CC of 0.461, a less accurate member that still maintains the left-mover (c) Member 14, CC of 0.020, and a less accurate member that dissipates the left-mover completely (d) Member 6, CC of -0.354 reflectivity is plotted.

After 4 DA cycles, the 2245 UTC forecast evolves similarly to the 2230 UTC forecast. Initially, the Multistatic members predict the Truth Run relatively accurately, but there is a strong decrease in CC values from 2300 UTC until 0045 UTC as the storm splits and the Truth Run maintains a left-mover while the Multistatic members predict dissipation (Figure 5.21). Similar to prior forecasts, the correlations improve significantly after 0045 UTC and remain relatively high throughout the remainder of the forecast. Once again, the maximum CC value during the 2345 UTC to 0045 UTC period, when there is a robust left-mover in the Truth Run and not the Multistatic members, is lower for the 2245 UTC forecast than it was for the 2230 UTC forecast. The maximum correlation during this period was 0.410 for the 2230 UTC forecast and is only 0.393 for the 2245 UTC forecast. Additionally, the Multistatic members predict dissipation of the left-mover much quicker than it dissipates in the Truth Run. The consistent degradation of the forecast during this period between successive forecasts is concerning because the forecast should be improving as initializations approach the time of the split. The most likely cause of this degradation is spurious convection around the dominant right-mover and the Multistatic members dissipating the left-mover a long time before the Truth Run. Therefore, the multistatic network no longer suppresses spurious convection as well in several members but continues to suppress the left-mover in a majority of the members. Additionally, each of these forecasts provides accurate prediction of the right-mover, which is the primary severe weather producer in the domain. This shows that the Multistatic experiments are accurately predicting the most important part of the forecast.

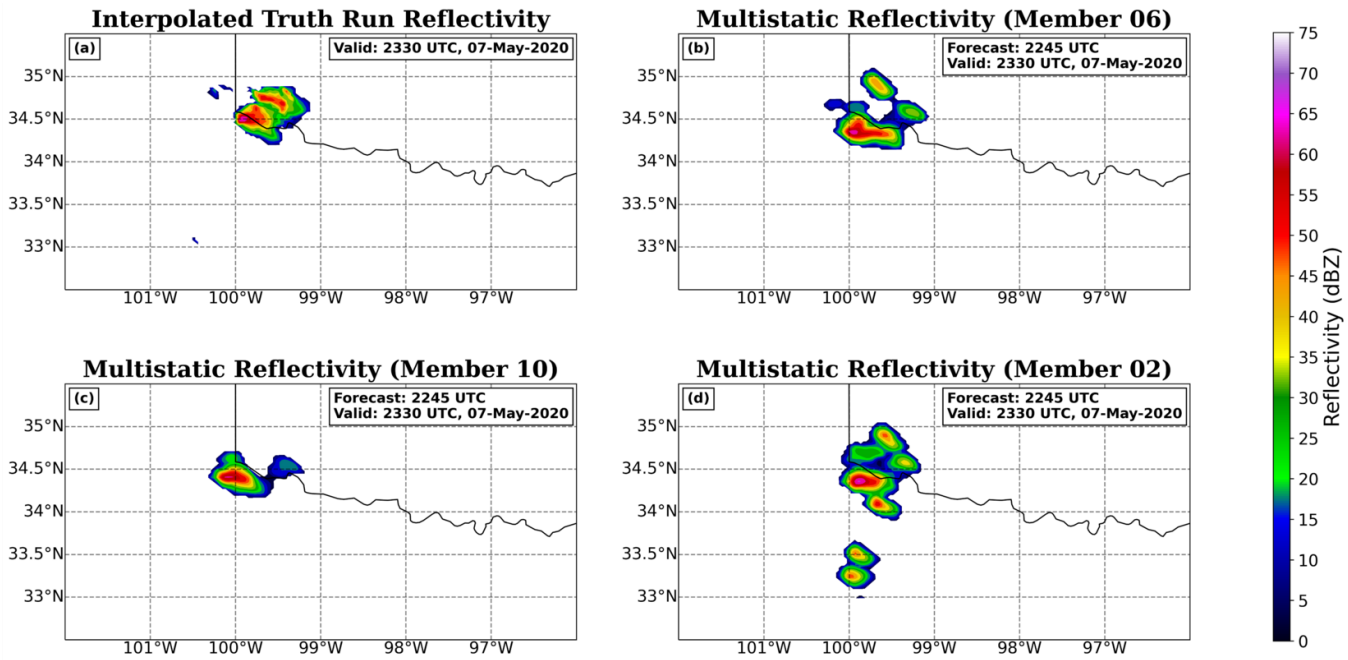

Figure 5.21: (a) Interpolated Truth Run reflectivity (dBZ) at 2330 UTC on 7 May 2020. For the 2245 UTC ensemble forecast at 2330 UTC, the best looking member (b) Member 6, CC of 0.656, a less accurate member that barely maintains the left-mover (c) Member 10, CC of -0.176, and a member that does not accurately predict the Truth Run (d) Member 2, CC of -0.027 reflectivity is plotted.

Following five DA cycles, the 2300 UTC analysis is the most accurate thus far for nearly every Multistatic member. However, by 2315 UTC more members produce areas of spurious reflectivity during the split but produce a more accurate prediction of the left-mover (Figure 5.22). The forecast of the right-mover is degraded at this time, and it is difficult to determine which parts of the storm are the dominant right-mover and the weaker left-mover. There are several cores of high reflectivity predicted in the Multistatic members that are not present in the Truth Run, further showing the degradation of this forecast. The assimilated bistatic velocity observations do not show any suspicious data resulting in the multiple cores present in the Multistatic experiments; however, all receivers have no returns along the baseline between the receiver and transmitter. The storm is complex at this time, which could be negatively impacting the Multistatic forecast and resulting in nosier storms by 2330 UTC. As a result, the period from 2345 UTC to 0045 UTC features the lowest CCs, but some members begin to improve their correlation to the Truth Run earlier at 0015 UTC, rather than 0040 or 0045 UTC in previous forecasts. This improvement results from the left-mover dissipating in the Truth Run, which allows the Multistatic members that did not have a robust left-mover to more accurately forecast the Truth Run at this time. In addition to this, the Multistatic members accurately represent the location of the right-moving storm and have a higher maximum member-average correlation than prior forecasts, with a maximum member-average correlation of 0.725 for Member 15. While the 2300 UTC forecast had the most accurate ensemble analyses for a majority of the members, the remaining forecast of all Multistatic members struggle to accurately represent the splitting process. However, the spurious convection seen in the 2245 UTC forecast is suppressed in the 2300 UTC forecast.

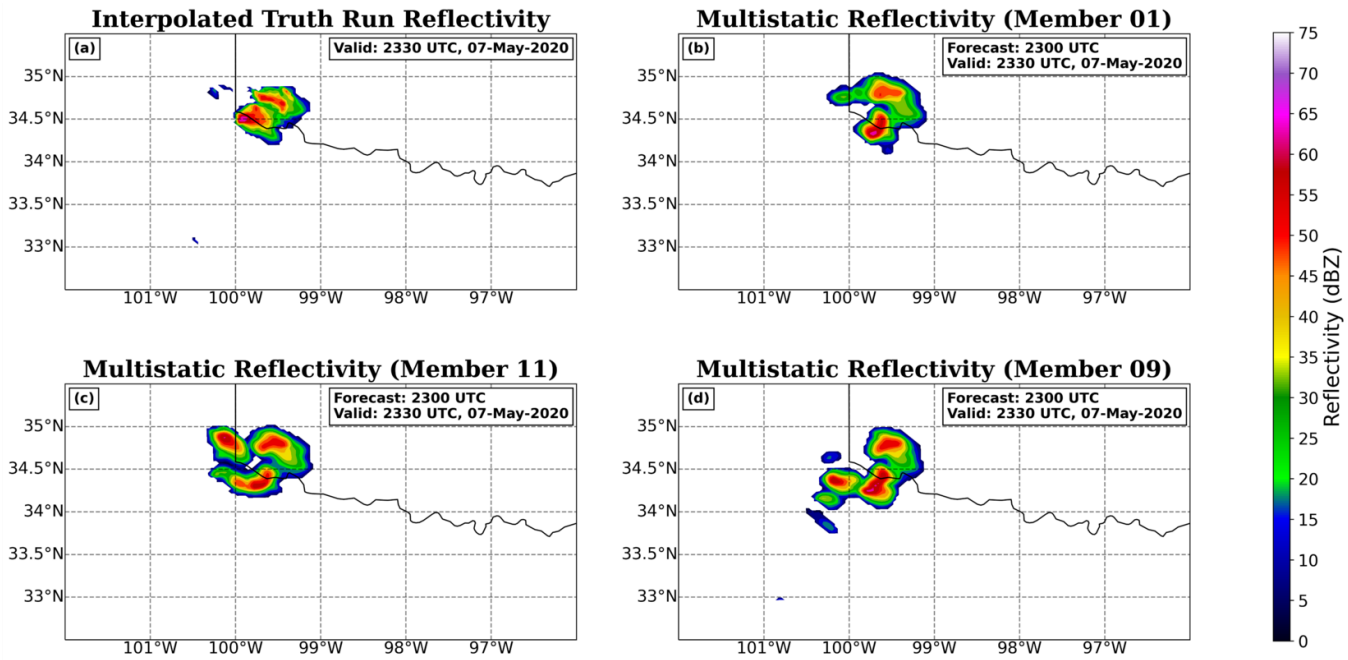

Figure 5.22: (a) Interpolated Truth Run reflectivity (dBZ) at 2330 UTC on 7 May 2020. For the 2300 UTC ensemble forecast at 2330 UTC, the best performing member (b) Member 1, CC of 0.952, the median performing member (c) Member 11, CC of 0.772 (median: 0.761), and the worst performing member (d) Member 9, CC of 0.318 reflectivity is plotted.

The 2330 UTC Multistatic forecasts produce an accurate analysis of the storm, and many members predict the evolution of the left-mover better than in previous forecasts (Figure 5.14). The minimum in CC between 2345 and 0045 UTC is still present, but the 2330 UTC forecast exhibits a higher maximum correlation during this time. Unlike previous forecasts, this improvement is expected owing to the decreased time between initialization and 2345 UTC. However, the CC values are still low relative to other forecast periods during this time (Figure 5.23). The uptick in CC values near the end of the splitting period begins slightly earlier for the 2330 UTC forecast than it did in prior forecasts, 0010 UTC compared to 0015 UTC for the 2300 UTC forecast and 0045 UTC for the other prior forecasts. While this change is not significant between the 2300 UTC forecast and the 2330 UTC forecast, the 2330 UTC forecast begins to produce more accurate forecasts about 35 minutes prior to earlier forecasts. This is expected because the storm is accurately analyzed and beyond the expected 4-6 assimilation cycles typically needed to spin up a storm (Tong and Xue 2005; Guerra et al. 2022). However, the Multistatic members tend to produce a stronger storm than the Truth Run and there is additional spurious convection that is not present in the Truth Run. Once again, the difference in intensity between the Multistatic members and the Truth Run is likely a result of the highest reflectivity cores in the raw Truth Run being smoothed over when interpolated on the 3 km grid. Despite this, the shape and location of the dominant right-mover match the Truth Run well during this forecast.

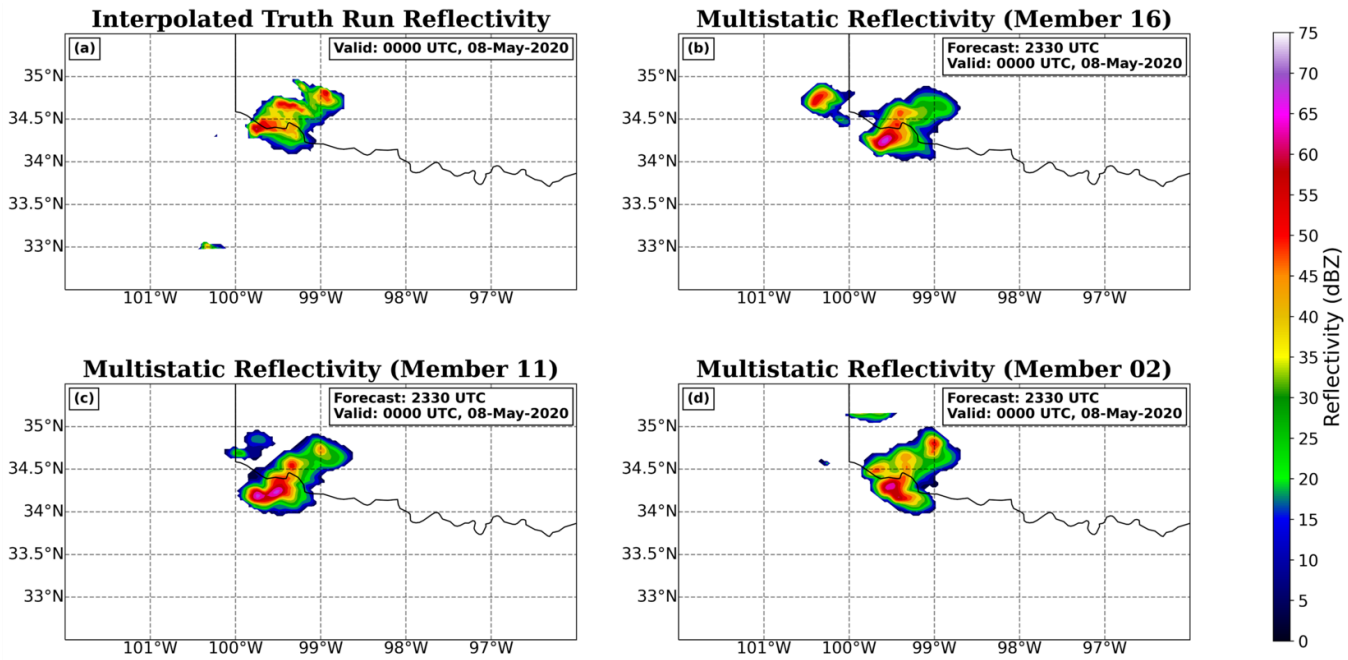

Figure 5.23: (a) Interpolated Truth Run reflectivity (dBZ) at 0000 UTC on 8 May 2020. For the 2330 UTC ensemble forecast at 0000 UTC, the best performing member (b) Member 16, CC of 0.777, the median performing member (c) Member 11, CC of 0.114 (median: 0.111), and the worst performing member (d) Member 2, CC of 0.018 reflectivity is plotted.

Up until the 2330 UTC forecast, every new initialization had many members increasing their average correlation to the Truth Run, but that is not the case for the 2330 UTC forecast. In fact, most members (15 of 18) have a decreased average correlation from the 2300 UTC forecast to the 2330 UTC forecast. Only three members improve their average correlation from the 2300 UTC forecast to the 2330 UTC forecast (Fig. 5.15). Previous research by Guerra et al. (2022) and Stratman et al. (2020) has shown that more DA cycles tend to produce better forecasts, but the 2330 UTC forecast seems to go against this finding. It is likely that the degradation between the 2300 UTC forecast, and the 2330 UTC forecast is caused by the complexity of the storm at this point, making it difficult to produce a forecast as highly correlation to the Truth Run as periods with simpler storm structure. However, despite the reduced correlation to the Truth Run between these two forecasts, the CCs in Figure 5.15 for the 2330 UTC forecast are generally higher than those from earlier forecasts. Therefore, the Multistatic experiment still produces more accurate forecasts at later initialization times than it does for the earlier initialization. In addition to this, the storm is accurately spun up in WoFS for several initializations at this point; therefore, the idea that the complexity of the storm is resulting in the forecast degradation makes sense. It is worth noting that the right-mover was accurately predicted in nearly every forecast after the 2215 UTC initialization, showing that the multistatic network observations accurately forecasted the primary severe threat.

5.3.2 Max Vertical Velocity Analysis

5.3.2.1 Ensemble Analyses

The maximum vertical velocity (MVV) analyses and forecasts have low correlation to the Truth Run throughout all initializations (Figure 5.24). There are a few factors

that decrease the MVV correlation between the Multistatic experiment and the Truth Run. First of all, updrafts are small and incompletely resolved in the 3 km horizontal grid spacing of the Multistatic experiment. The Truth Run with 250 m horizontal grid spacing will resolve higher MVV value with the supercellular updrafts, whereas with 3 km horizontal grid spacing the updraft will be smoothed. Therefore, the Truth Run produces much higher MVV values throughout the analyses and forecasts, and when it is interpolated onto the 3 km grid these higher values still appear. These intensity differences are a major driving factor to the low CCs between the simulations and the Truth Run. Additionally, the MVV values span a smaller spatial extent due to insufficient resolution of updrafts. Therefore, a small change in the MVV values in the Multistatic experiment result in a much larger impact to the CCs. Similarly, a small change in the MVV values of the Interpolated Truth Run will also significantly impact the CCs. Resulting from these two inherent problems with the MVV analysis, little can be accurately inferred from the CCA and diagnosing the impacts must rely on subjective analysis. For this reason, the CCA is weighted less than the subjective analysis for this discussion.

For the 2215 UTC ensemble analyses, all Multistatic members have some MVV analyzed, but all regions are smaller than that of the Truth Run (Figure 5.24). The Truth Run has a maximum MVV around 20 ms^{-1}, while the maximum MVV in any Multistatic member is closer to 10 ms^{-1}. Additionally, the Truth Run has three separate updrafts present at 2215 UTC, while the Multistatic members only analyze one, weaker updraft (Figure 5.25). However, the Multistatic updrafts are located close to where the main updraft in the Truth Run is located. The highest correlation occurs in Member 7 with a CC of 0.405 and a r^2 value of 16.4%. Meanwhile, the lowest correlated member is Member 11 with a CC of 0.010 and a r^2 value of 0.01%. Therefore, neither the best nor the worst correlated member are similar to the Truth Run. Despite

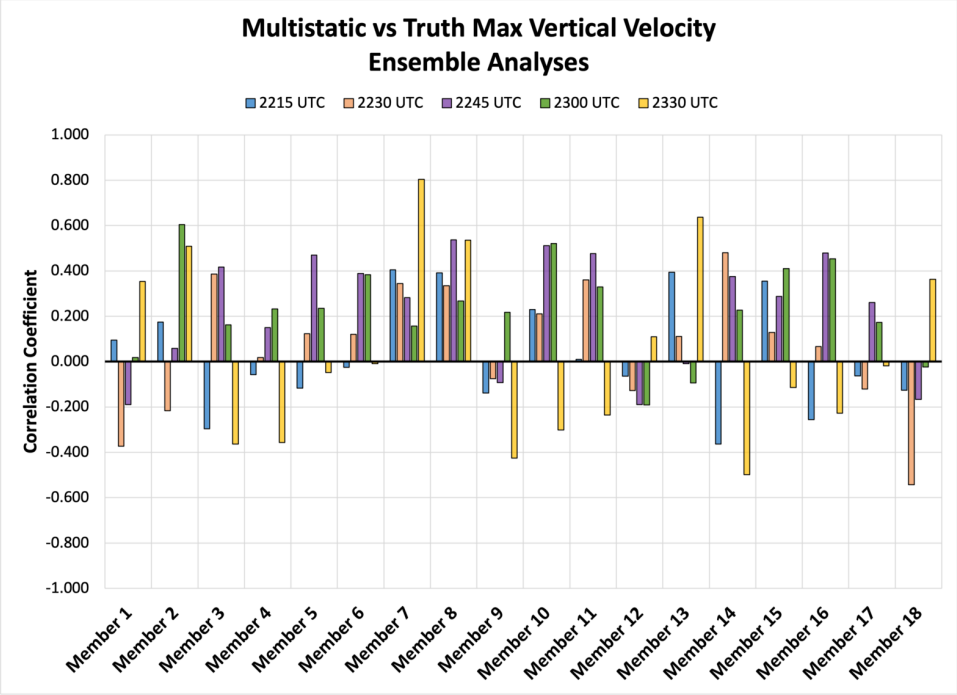

Figure 5.24: Correlation Coefficients for each member for the ensemble analyses from 2215 (blue), 2230 (orange), 2245 (purple), 2300 (green), and 2330 (yellow) UTC.

this, the location of the primary Truth Run updraft is well matched by the Multistatic members and the intensity of the Multistatic experiment is much lower than the Truth Run, which is expected. Overall, this is a qualitatively accurate forecast of updraft location for the Multistatic members.

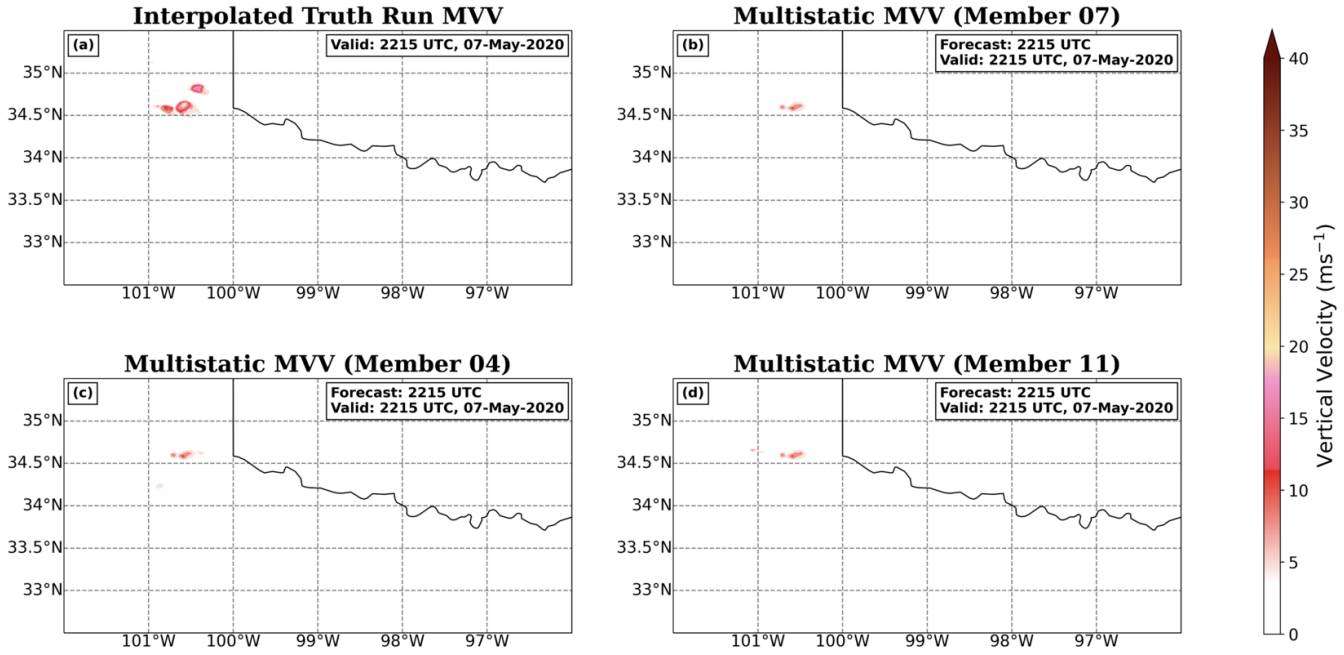

Figure 5.25: (a) Interpolated Truth Run MVV (ms^{-1}) at 2215 UTC on 7 May 2020. For the 2215 UTC ensemble analysis, the best performing member (b) Member 7, CC of 0.405, the median performing member (c) Member 4, CC of -0.057 (median: -0.041), and the worst performing member (d) Member 11, CC of 0.010 MVV is plotted.

Similar to the 2215 UTC ensemble analyses, the 2230 UTC ensemble analyses have low CC values across all members, but there is some evidence of slight improvements with the DA cycling. The maximum CC increases from 0.405 (r^2 value of 16.4%) in the previous ensemble analyses to -0.543 (r^2 value of 29.4%) in the 2230 UTC ensemble analyses. However, the resolution differences and the small spatial scale of the updrafts, compared to reflectivity, results in noisy CC analyses. At this time, the Truth Run is creating a more cohesive updraft, with the three previous updrafts consolidating into a primary updraft to the south and a weaker updraft to the north (Figure 5.26). The MVV is around 20 ms^{-1} for the Truth Run, while the strongest Multistatic member only has an MVV value of around 12 ms^{-1}. Once again, the location of the updraft in the Multistatic members matches the location of the primary updraft in the Truth Run and the Multistatic members produce an accurate forecast of updraft location.

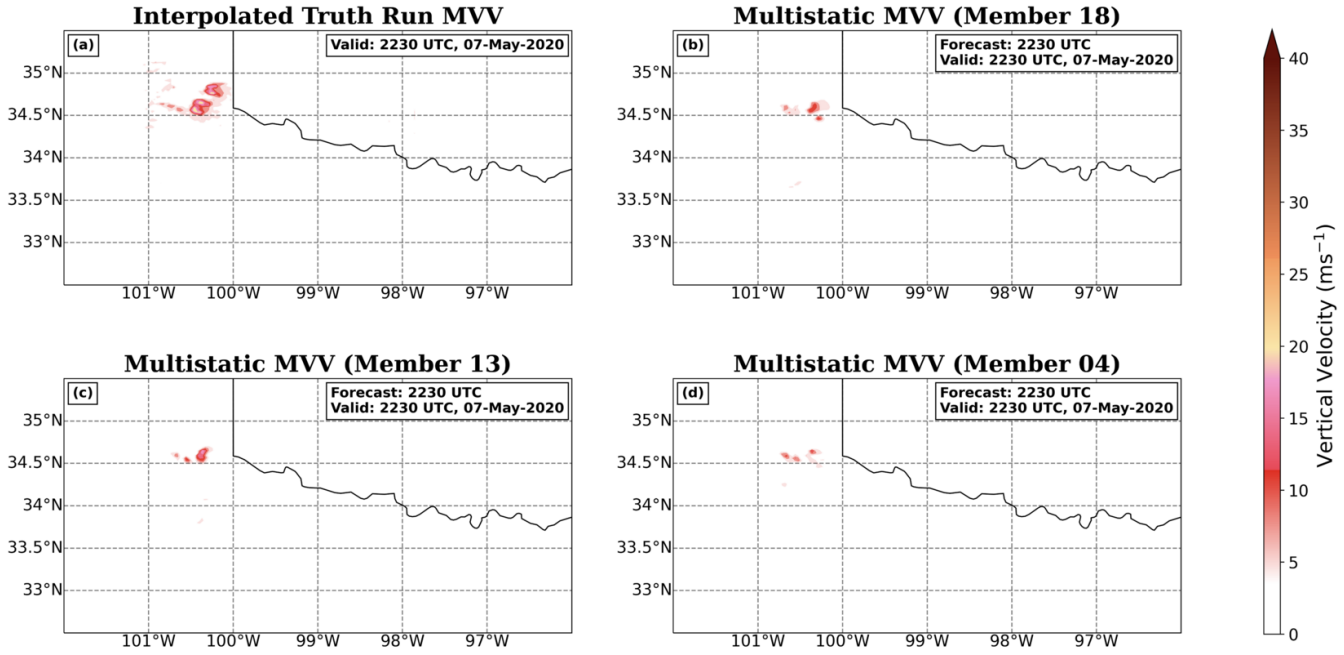

Figure 5.26: (a) Interpolated Truth Run MVV (ms^{-1}) at 2230 UTC on 7 May 2020. For the 2230 UTC ensemble analysis, the best performing member (b) Member 18, CC of -0.543, the median performing member (c) Member 13, CC of 0.112 (median: 0.116), and the worst performing member (d) Member 4, CC of 0.018 MVV is plotted.

After 4 DA cycles, the 2245 UTC ensemble analyses degrades slightly in quality from previous analyses. The highest correlation dropped from -0.543 (r^2 value of 29.4%) in the 2230 UTC ensemble analyses to 0.536 (r^2 value of 28.8%) in the 2245 UTC ensemble analyses, and the lowest correlation dropped from 0.018 in the 2230 UTC ensemble analyses to -0.009 (r^2 value of 0.01%) in the 2245 UTC ensemble analyses. This is the only forecast that degrades in quality from the previous forecast. At 2245 UTC, the Truth Run MVV is complex with a dominant updraft in the center of the storm, but two subsequent updrafts to the north and south. This is likely due to the initial evolution of the storm split. The Multistatic members produce multiple updrafts, with a stronger updraft to the south. The strongest updraft in the Multistatic members is displaced slightly further south than the dominant Truth Run updraft. The northern updraft suggests that the members are capturing the early evolution of the storm split, but with much weaker amplitude than the Truth Run. Member 8, with the highest CC, appears to have the strongest updraft of the members and is well correlated to the Truth Run's location, but the updraft is much smaller than that of the Truth Run (Figure 5.27). The most poorly correlated member, Member 13, has two updrafts that are in the proper positions, but they are much weaker and smaller than the Truth Run updrafts. Additionally, Member 13 has spurious updrafts to the south of the primary updraft, which are not present in the Truth Run. However, most of these spurious updrafts are weaker than about 5 ms^{-1}. Therefore, the poor CCs are more related to spurious updrafts, and resolution-based differences in updraft intensity, than the location of the updrafts and the Multistatic members are producing accurate analyses of the storm location at this time.

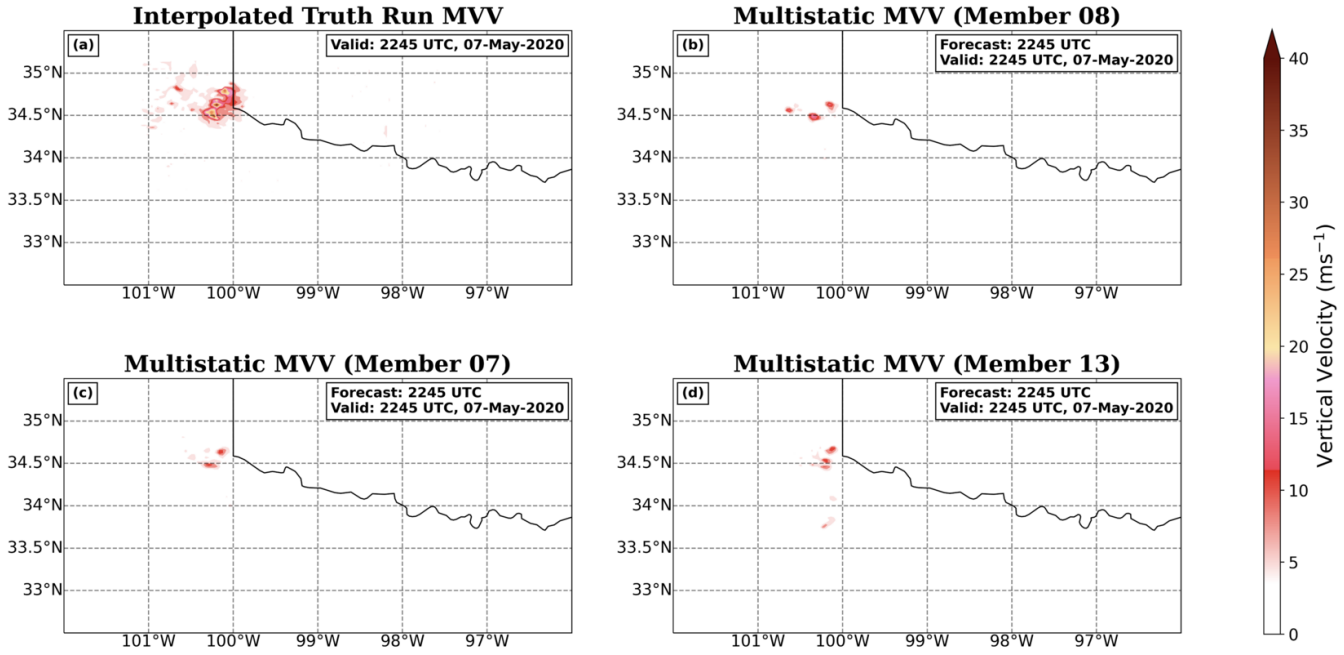

Figure 5.27: (a) Interpolated Truth Run MVV (ms^{-1}) at 2245 UTC on 7 May 2020. For the 2245 UTC ensemble analysis, the best performing member (b) Member 8, CC of 0.536, the median performing member (c) Member 7, CC of 0.282 (median: 0.284), and the worst performing member (d) Member 13, CC of -0.009 MVV is plotted.

Once again, the highest correlation improves from the 2245 UTC ensemble analyses to the 2300 UTC ensemble analyses with additional DA cycles. At this time, Member 2 has the highest correlation to the Truth Run with a CC of 0.604 and a r^2 value of 36.5%. Member 1 has the lowest correlation to the Truth Run with a CC of 0.018 and a r^2 value of 0.03%, an insignificant improvement from the 2245 UTC ensemble analyses. At 2300 UTC, the Truth Run shows a clear, two updraft structure that matches the conceptual model of a splitting supercell (Figure 5.28). The dominant, southern updraft has MVV values in excess of 35 ms^{-1} and the northern updraft has MVV of around 30 ms^{-1}. There are some spurious updrafts to the west of the main Truth Run storm, but they are small with MVV values around 10 ms^{-1}. Additionally, all Multistatic members analyze two updrafts at this time, but both are much weaker than the Truth Run storm with MVV values around 15 ms^{-1} for the strongest members. Member 2 has some additional spurious updrafts to the far south and north of the main two updrafts, and the dominant updraft is displaced further south than the Truth Run updraft. Although small, the northern updraft that is associated with the left-split is positioned similarly to the Truth Run, evident by the larger positive MVV difference and minimal negative differences in Figure 5.29. Member 1 has a displaced dominant updraft as well, but it is smaller than the updraft in Member 2 and the Truth Run. The left-split in Member 1 is displaced slightly to the northeast of the actual location of the left-split in the Truth Run. Both updrafts in Member 1 are smaller than the updrafts in Member 2 and in the Truth Run, which decreases the correlation for this member.

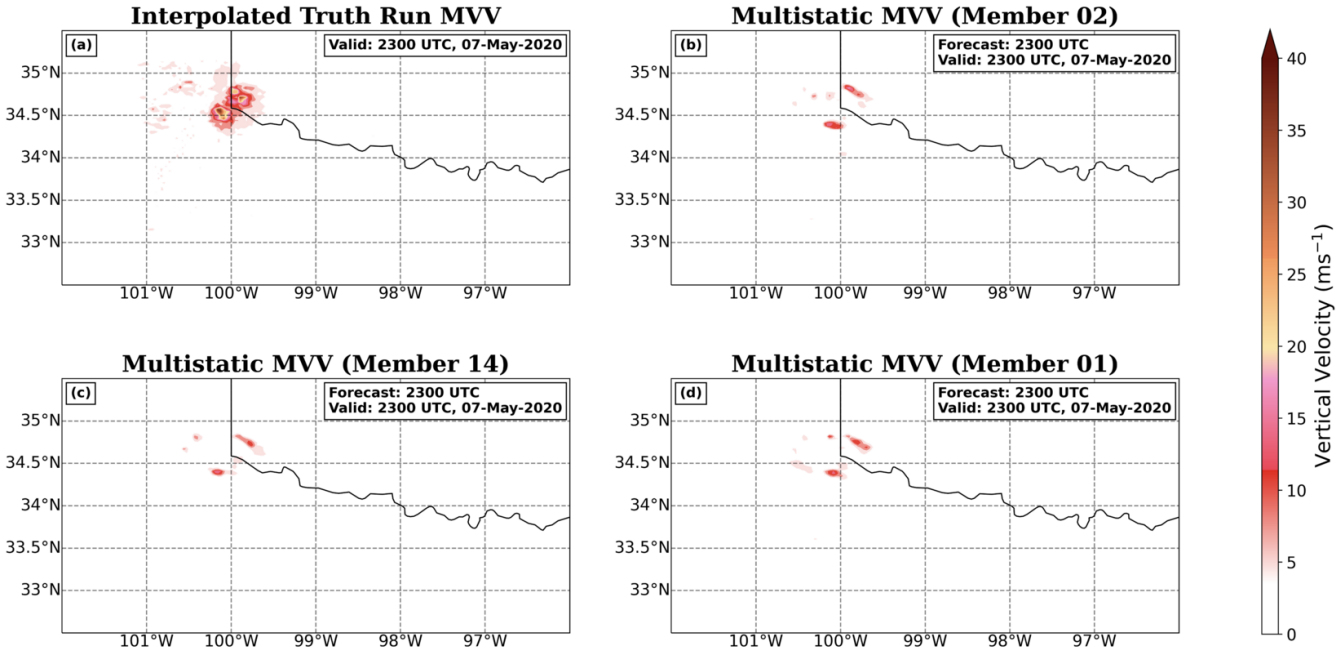

Figure 5.28: (a) Interpolated Truth Run MVV (ms^{-1}) at 2300 UTC on 7 May 2020. For the 2300 UTC ensemble analysis, the best performing member (b) Member 2, CC of 0.604, the median performing member (c) Member 14, CC of 0.227 (median: 0.229), and the worst performing member (d) Member 1, CC of 0.018 MVV is plotted.

By the 2330 UTC ensemble analyses, the CCs have improved significantly from previous analyses after 7 DA cycles. The maximum correlation for this forecast increases to 0.804 with a r^2 value of 64.6%, but the minimum correlation decreased again to -0.009 (r^2 value of 0.01%). This forecast initializes after the split has completed and a robust left-mover is present in the Truth Run domain. The Truth Run right-mover is now one cohesive storm with a single, primary, dominant updraft of around 35 ms^{-1} (Figure 5.30). The left-mover has propagated northeasterly, away from the dominant right-mover, and decreased in strength to a MVV value of around 25 ms^{-1}. Multistatic Member 7 is the best performing member for this forecast, with a large area of MVV values that are weaker than the Truth Run. The larger expanse of MVV values is likely improving the correlation to the Truth Run due to the Truth Run having a larger expanse of strong MVV values. Therefore, Member 7 matches the expanse of the Truth Run's right-mover's updraft better than any other member, but the right-mover updraft is weaker than the Truth Run. Additionally, the strongest updrafts in the Multistatic experiment do not match the location of the strongest updraft in the Truth Run. In fact, the strongest updrafts in Member 7 are displaced to the east of the Truth Run updrafts. Similarly, Member 6 is the lowest correlated member with several spurious updrafts. The strongest updrafts in Member 6 are displaced from the Truth Run and the intensity is lower. Neither Member 7 nor Member 6 match the location of the Truth Run updraft and both are displaced to the east. Therefore, from subjective comparison, the Multistatic analyses are not as accurate as the CCs suggest, due to the displacement of the updrafts.

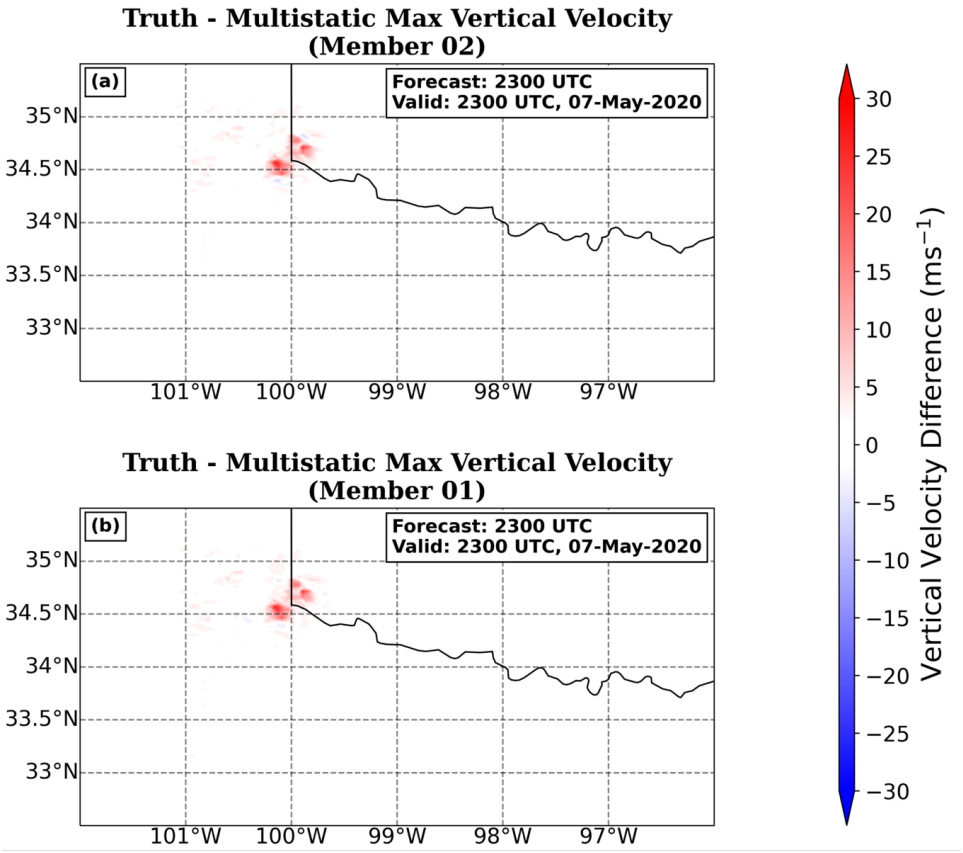

Figure 5.29: 2300 UTC Truth Run MVV minus the 2300 UTC ensemble analysis Multistatic MVV for (a) Member 2 and (b) Member 1. All differences are in ms^{-1}.

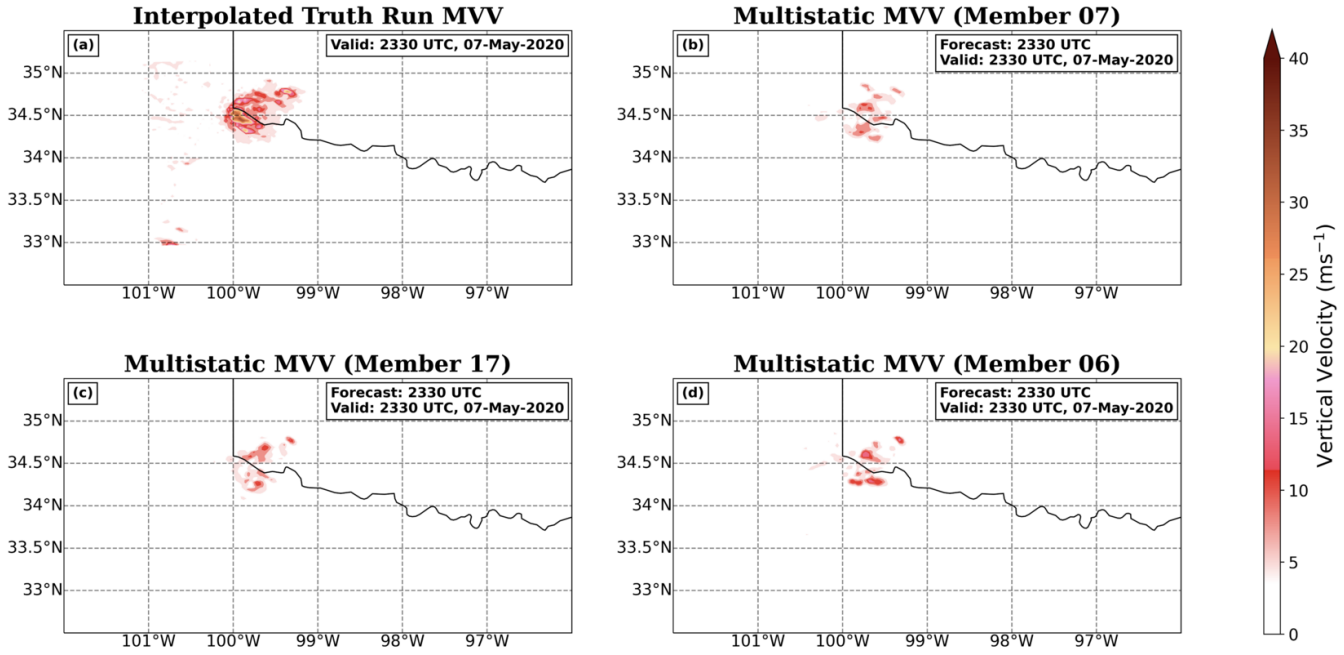

Figure 5.30: (a) Interpolated Truth Run MVV (ms^{-1}) at 2330 UTC on 7 May 2020. For the 2330 UTC ensemble analysis, the best performing member (b) Member 7, CC of 0.804, the median performing member (c) Member 17, CC of -0.019 (median: -0.033), and the worst performing member (d) Member 6, CC of -0.009 MVV is plotted.

5.3.2.2 Ensemble Forecasts

The remaining forecasts for all initializations produce low average CCs across all members (Figure 5.31). The highest member average correlation is 0.430 (r^2 value of 18.47%), 0.503 (r^2 value of 25.28%), 0.508 (r^2 value of 25.83%), 0.517 (r^2 value of 26.76%), 0.525 (r^2 value of 27.54%), and 0.556 (r^2 value of 30.93%) for the 2200, 2215, 2230, 2245, 2300, and 2330 UTC forecasts, respectively. Therefore, even the best member does not accurately produce a forecast of the Truth Run. Once again, it is important to note that the poor correlations are exaggerated by the grid spacing differences between the Multistatic experiment and the Truth Run. The Truth Run will always produce higher MVV values because the 250 m horizontal grid spacing better resolves updraft intensity. Interpolating Truth Run MVV values onto a 3 km grid smooths values but maintains much higher MVV values than any Multistatic member. More pertinent than the clear discrepancy in updraft strength, the Multistatic members tend to displace the main updraft away from where the Truth Run's updraft is located. It is generally displaced to the west and south, with only a few members displaced to the east. Examples of select members showing this displacement for the 2215 and 2230 UTC forecasts at 0000 UTC are shown in Figures 5.32 and 5.33.

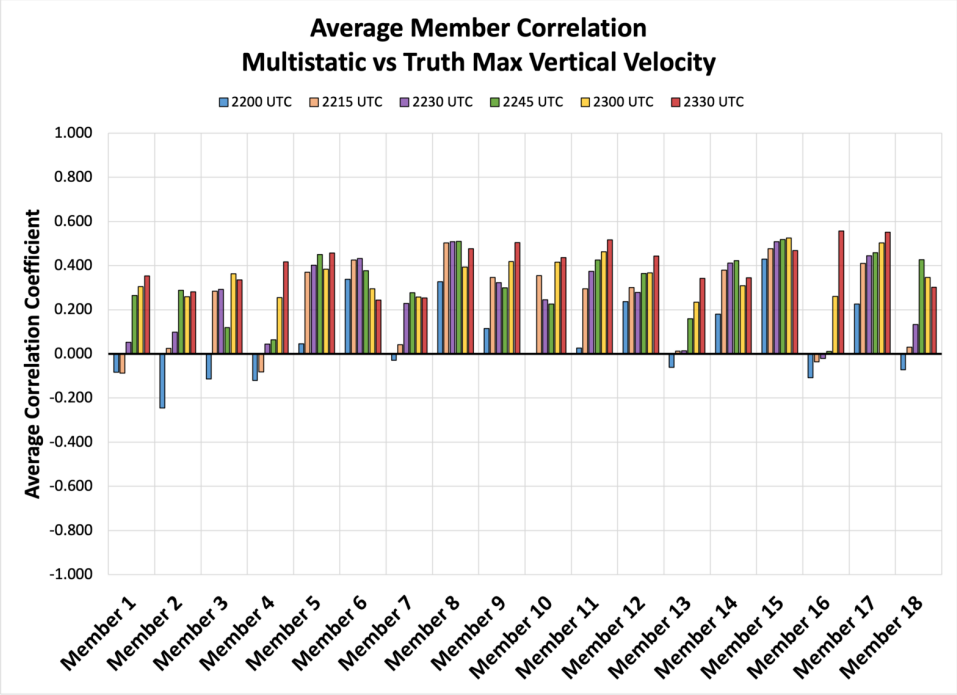

Figure 5.31: Average correlation coefficient for each member for each forecast: 2200 (blue), 2215 (orange), 2230 (purple), 2245 (green), 2300 (yellow), and 2330 UTC (red).

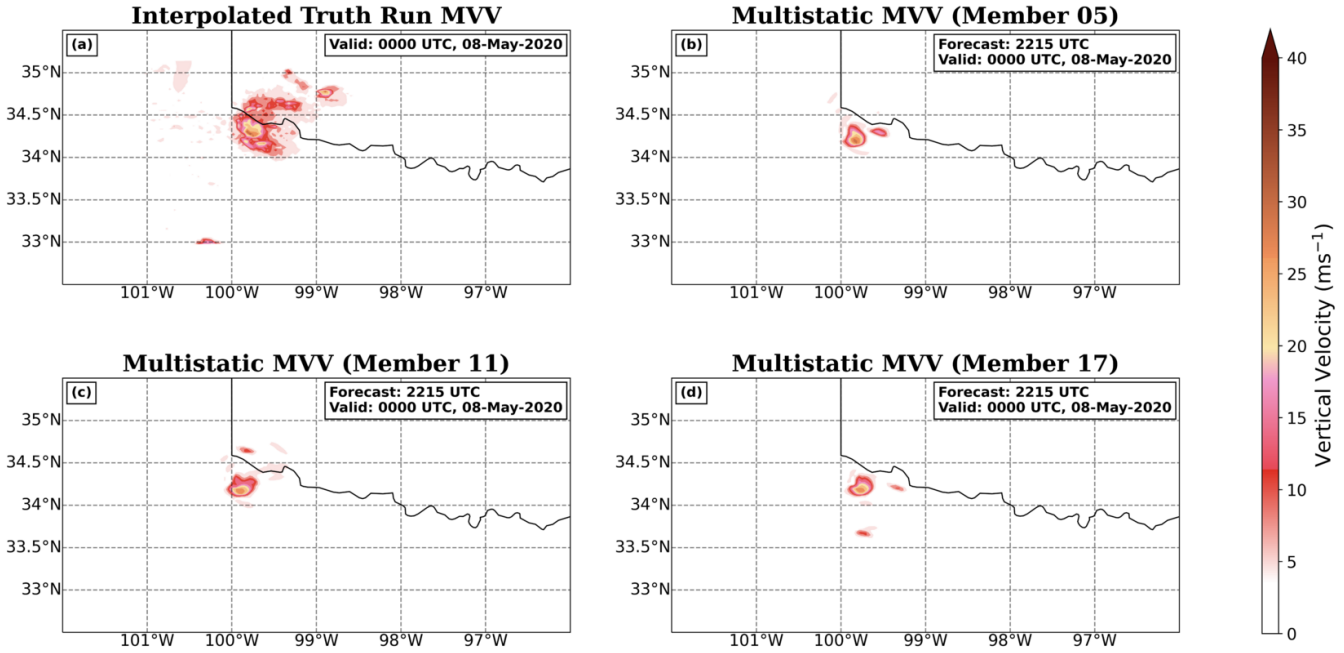

Figure 5.32: (a) Interpolated Truth Run MVV (ms^{-1}) at 0000 UTC on 7 May 2020. MVV is plotted for the 2215 UTC ensemble forecast at 0000 UTC for (b) Member 5 with a southern displacement, (c) Member 11 with a southern displacement, and (d) Member 17 with a southern displacement.

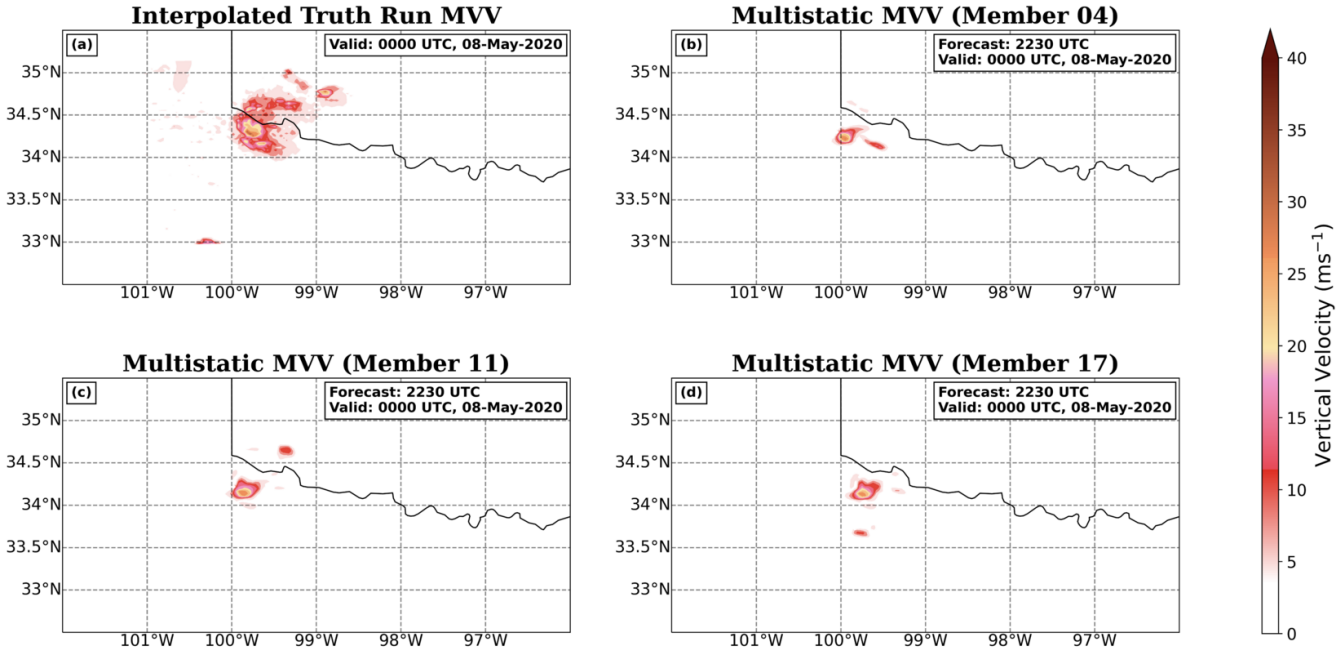

Figure 5.33: (a) Interpolated Truth Run MVV (ms^{-1}) at 0000 UTC on 7 May 2020. MVV is plotted for the 2230 UTC ensemble forecast at 0000 UTC for (b) Member 4 with a southwestern displacement, (c) Member 11 with a southern displacement, and (d) Member 17 with a southwestern displacement.

In 1-hour forecasts initialized at 2300 UTC, the displacement between the Multistatic MVV values and the Truth Run MVV values becomes more widespread. Generally, the Multistatic MVV values for the right-mover are displaced south of the Truth Run updraft, but the displacement is not consistent among the Multistatic members. Member 2 displays a southeastern displacement of around a quarter degree longitude, while Members 12 and 15 show a southern displacement of similar magnitude (Figure 5.34). The displacement shifts further east for the 2330 UTC forecast valid at 0000 UTC. Members 1, 13, and 18 all show a southeasterly displacement of around a quarter degree longitude (Figure 5.35). This shows that the Multistatic members tend to place the right-mover farther south and east and propagate them eastward quicker than the Truth Run. During the later initializations, the displacement shifts further east, while the earlier initializations showed more of a southerly displacement. Overall, there appears to be generally southern bias on the placement of the primary updraft within the Multistatic members, but this bias shifts from a southwestern displacement at early initializations to a southeastern displacement at later initializations.

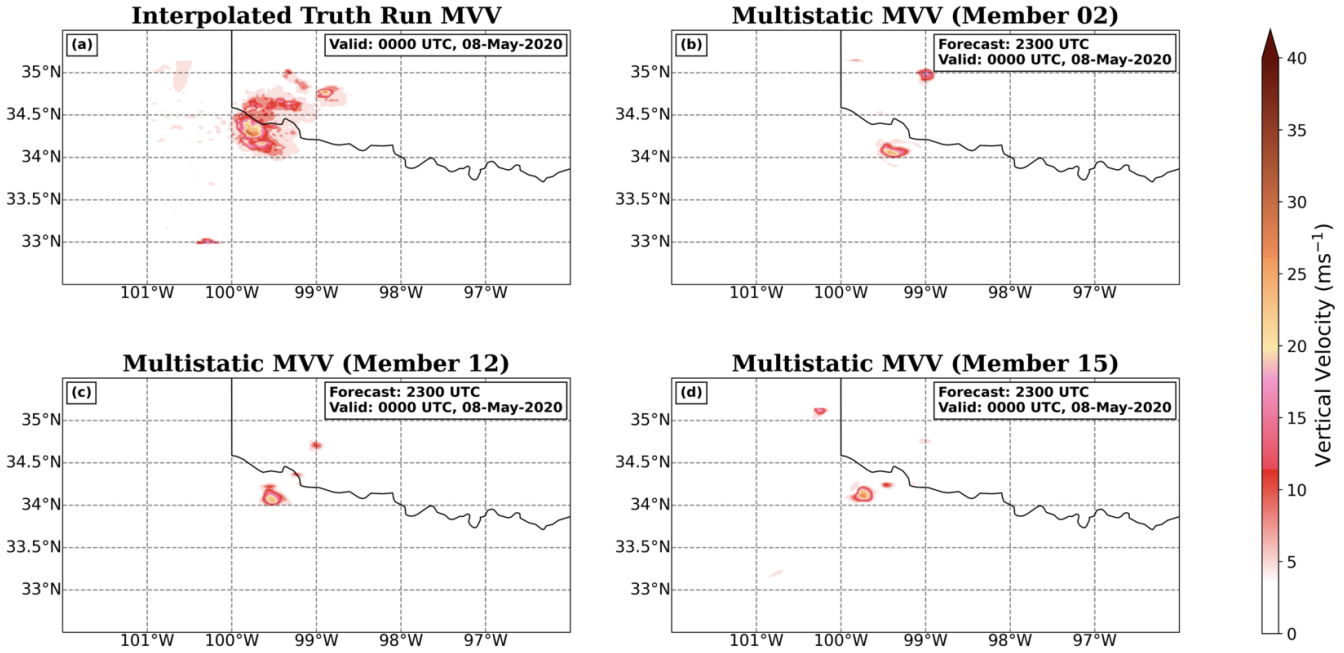

Figure 5.34: (a) Interpolated Truth Run MVV (ms^{-1}) at 0000 UTC on 7 May 2020. MVV is plotted for the 2300 UTC ensemble forecast at 0000 UTC for (b) Member 2 with a southeastern displacement, (c) Member 12 with a southern displacement, and (d) Member 15 with a southern displacement.

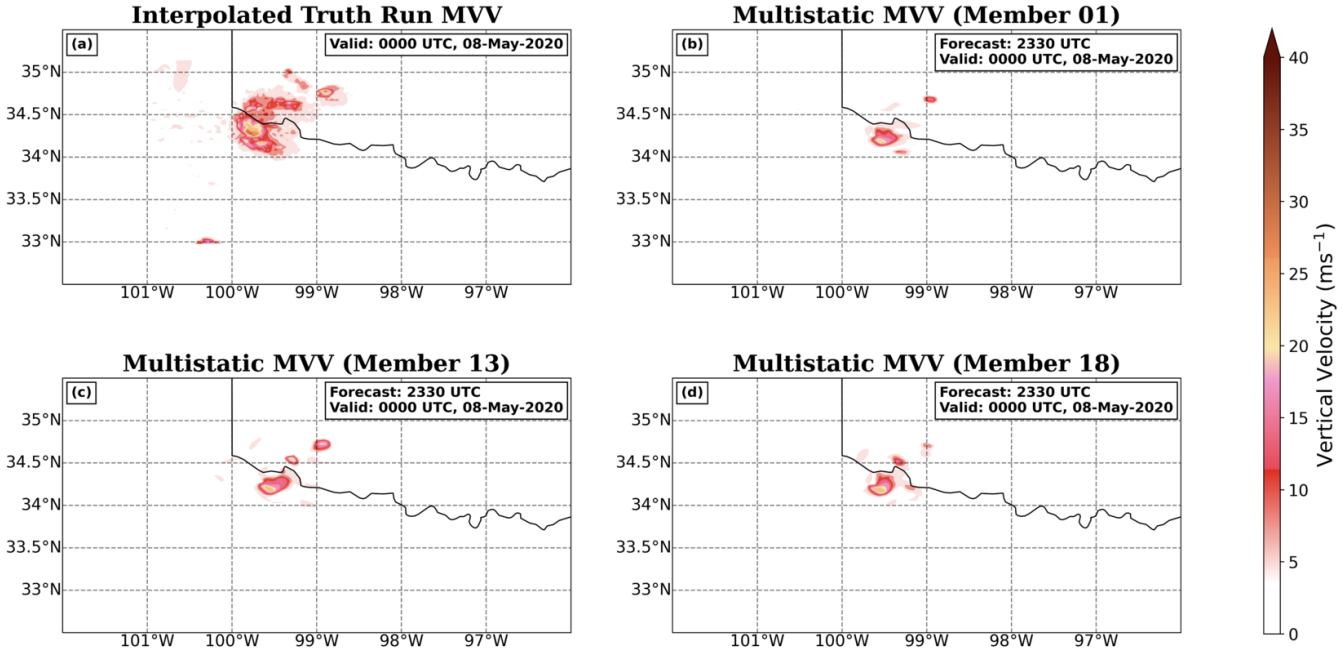

Figure 5.35: (a) Interpolated Truth Run MVV (ms^{-1}) at 0000 UTC on 7 May 2020. MVV is plotted for the 2330 UTC ensemble forecast at 0000 UTC for (b) Member 1 with a southeastern displacement, (c) Member 13 with a southeastern displacement, and (d) Member 18 with a southeastern displacement.

5.4 Multistatic Density vs WSR-88D Only

5.4.1 Reflectivity Analysis

5.4.1.1 Ensemble Analyses

For the 2200 UTC ensemble analyses the Multistatic experiment and WSR-88D Only experiment are essentially identical, with the lowest correlation coefficient of 0.999 (Figure 5.36). This lack of spread is due to the lack of any bistatic velocity observations at this time, resulting in assimilation of identical radar reflectivity observations in each experiment.

The similarity between the Multistatic experiment and the WSR-88D Only experiment continues in the 2215 UTC ensemble analyses (Figures 5.36 and 5.37). Member 6 of the Multistatic experiment has a slightly stronger storm than what the WSR-88D Only Member 6 shows, but these differences are small. However, the stronger storm in the Multistatic Member 6 is more similar to what the Truth Run shows, but most members between the two experiments have storms that are weaker than the Truth Run. Additionally, Member 17 for both experiments has spurious convection in the northwestern portion of the domain that is not present in the Truth Run. The Multistatic members tend to have a slightly larger storm overall when compared to the WSR-88D Only members, but again the difference is subtle. CCA further shows that the two experiments look similar at this time. Member 17 has the lowest correlation between the Multistatic experiment and the WSR-88D Only experiment with a CC of 0.947 and a r^2 value of 89.8%. Conversely, Member 6 has the highest correlation with a CC of 0.9995 and a r^2 value of 99.9%, showing that the Multistatic Member 6 and the WSR-88D Only Member 6 are essentially identical. However, for the Multistatic vs WSR-88D Only experiment, the most interesting members are those with the lowest

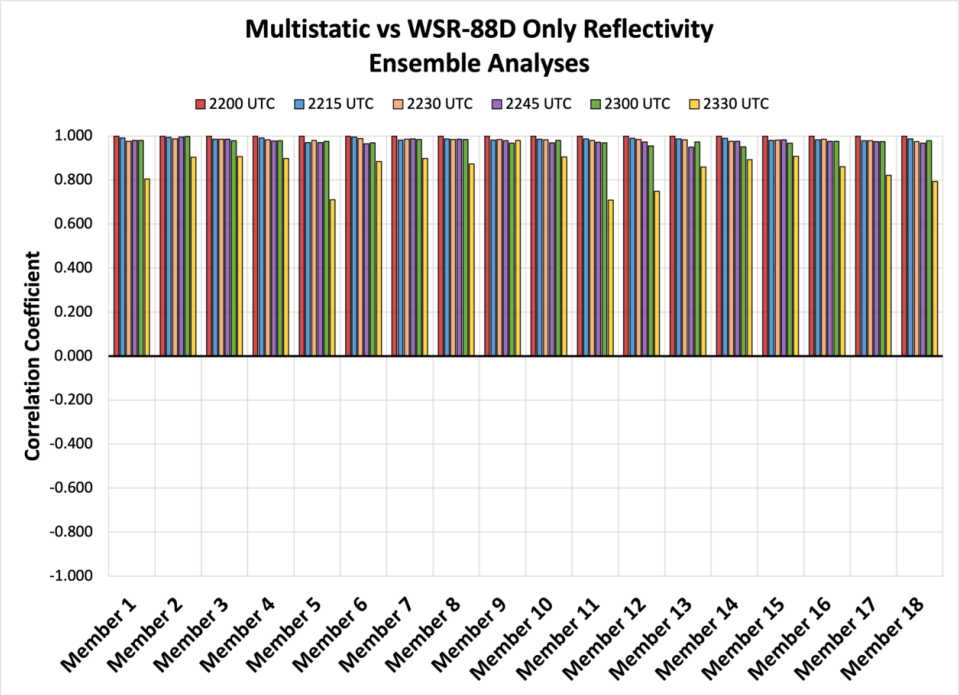

Figure 5.36: Multistatic vs WSR-88D Only correlation coefficient for each member for the ensemble analyses of the 2200 (red), 2215 (blue), 2230 (orange), 2245 (purple), 2300 (green), and 2330 UTC (yellow) forecast runs.

correlation, which result when there is a larger difference between the Multistatic experiment and the WSR-88D Only experiment. Both experiments are similar between the strongest and most weakly correlated members (Figure 5.37), with the Multistatic members having slightly higher simulated reflectivity than the WSR-88D Only members. The stronger storms match the Truth Run better than the weaker storms in the WSR-88D Only members.

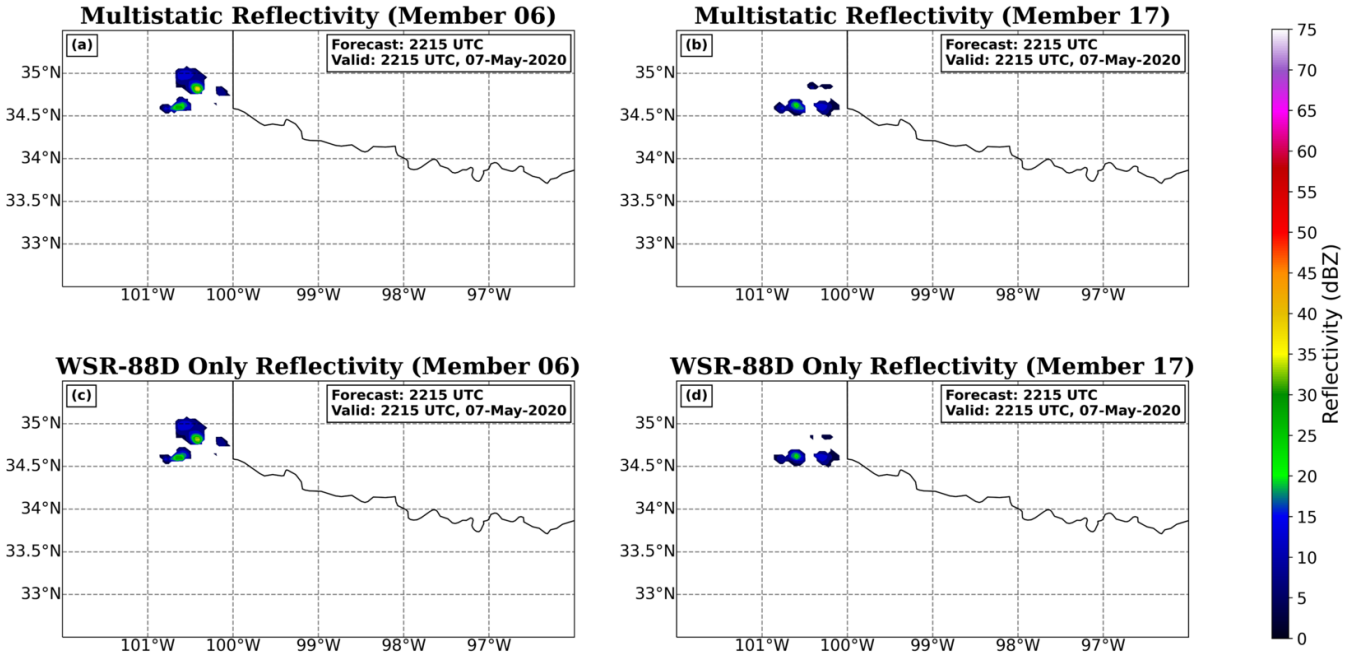

Figure 5.37: (a) Multistatic reflectivity (dBZ) for the highest correlation member, Member 6, (b) Multistatic reflectivity for the lowest correlation member, Member 17, (c) WSR-88D Only reflectivity for the highest correlation member, Member 6, and (d) WSR-88D Only Reflectivity for the lowest correlation member, Member 17.

Once again, the differences between the Multistatic members and the WSR-88D Only members are small for the 2230 UTC ensemble analyses (Figure 5.36). Many of the Multistatic members tend to have a slightly stronger storm in the domain, which matches the Truth Run better, but neither experiment looks significantly different from the other. The CCs between the Multistatic members and the WSR-88D Only members support this, with the highest correlated member being Member 6 with a CC of 0.988 and the lowest correlated member, Member 18, with a CC of 0.975. However, the WSR-88D Only Members 6 and 18 have a stronger storm than corresponding members in the Multistatic experiment (Figure 5.38). Figure 5.38 shows Member 6 and a more representative member, Member 5, that shows the higher intensity in the Multistatic experiment. For this analysis, the Multistatic experiment has 8 members with a higher correlation to the Truth Run, while the WSR-88D Only experiment has 11 members with a higher correlation to the Truth Run. However, the subjective analysis suggests that more Multistatic members have more accurate analyses of the intensity of the Truth Run storm at this time.

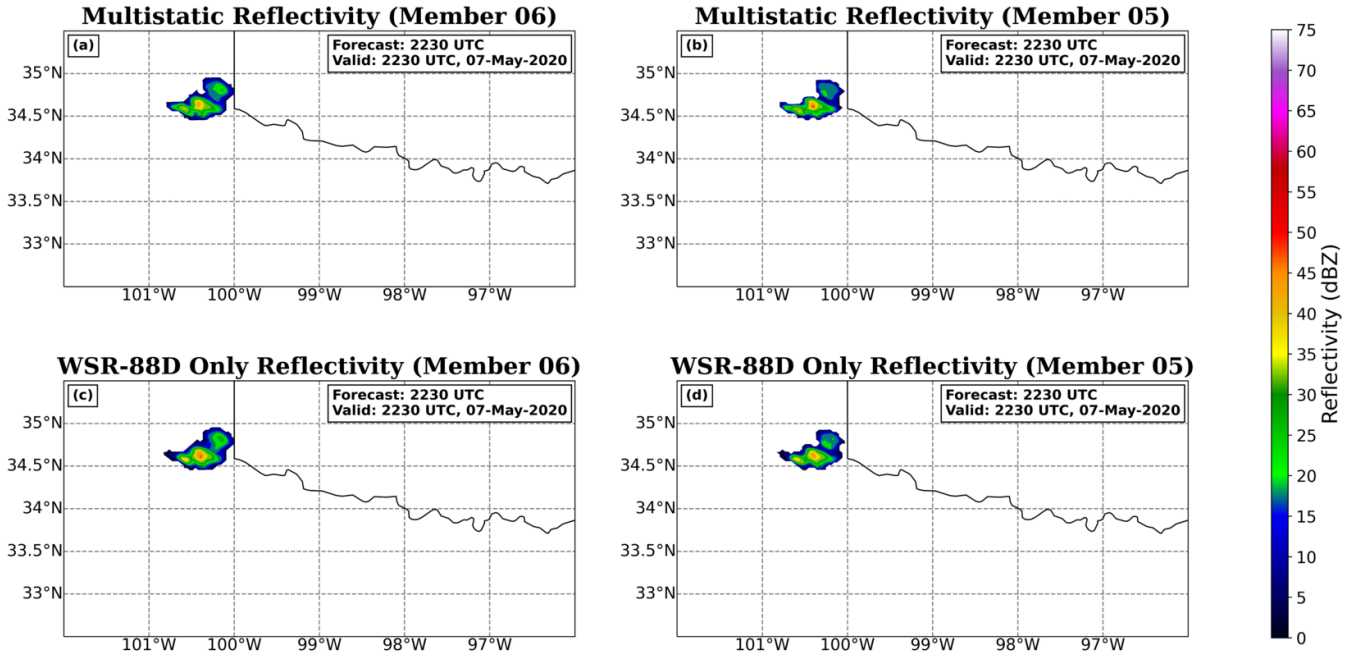

Figure 5.38: (a) Multistatic reflectivity (dBZ) for the highest correlation member, Member 6, (b) Multistatic reflectivity for a representative member, Member 5, (c) WSR-88D Only reflectivity for the highest correlation member, Member 6, and (d) WSR-88D Only Reflectivity for a representative member, Member 5.

At the 2245 UTC ensemble analyses, the two experiments remain similar (Figure 5.36); the storm is located directly over the transmitting radar at this time and many of the Multistatic members have a slightly stronger storm in the domain than the WSR-88D Only members do, which better matches the Truth Run (Figure 5.39). For this ensemble analysis, Member 2 has the highest correlation between the experiments while Member 13 has the lowest correlation, with CC values of 0.995 and 0.949, respectively. Interestingly, both Multistatic Members 13 and 2 have a stronger storm than what is present in the WSR-88D Only members. Multistatic Member 2 appears to analyze the western appendage of the storm more accurately than the WSR-88D Only Member 2. Multistatic Member 13's storms appear to match the Truth Run well, other than some discrepancies between the intensities. However, all differences between the two experiments are subtle. It appears that the multistatic network may help resolve the intensity of the storm slightly better at this time, but this is not true for every member.

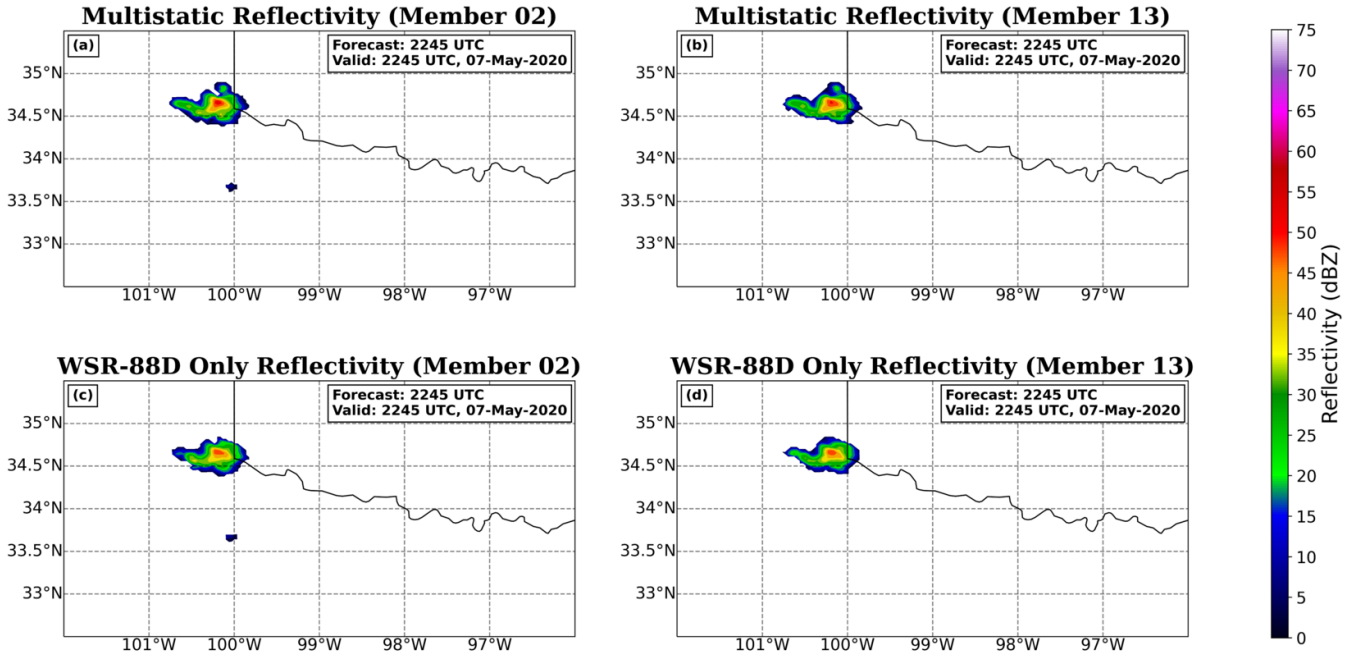

Figure 5.39: (a) Multistatic reflectivity (dBZ) for the highest correlation member, Member 2, (b) Multistatic reflectivity for the lowest correlation member, Member 13, (c) WSR-88D Only reflectivity for the highest correlation member, Member 2, and (d) WSR-88D Only Reflectivity for the lowest correlation member, Member 13.

By the 2300 UTC analysis, the experiments are becoming more dissimilar, and the CCs continue to drop (Figure 5.36). Multistatic members 1, 2, 3, 4, 8, 13, 15, 17, and 18 appear to have a stronger storm than the corresponding WSR-88D Only members, while the remaining members have similar intensities between the experiments. The WSR-88D Only members do not appear to have any member with a stronger storm than the Multistatic experiment. Additionally, while similar, the storms in the Multistatic members appear to capture more storm-scale detail than the WSR-88D Only members. For this analysis, Member 2 has the highest correlation with a CC of 0.998 and Member 14 has the lowest with a CC of 0.951 (Figure 5.40). Member 14 analyzes a stronger storm in the Multistatic experiment that is more similar to the intensity of the Truth Run. When compared to the Truth Run, the Multistatic Member 14 has a CC of 0.902 (r^2 value of 81.4%), while the WSR-88D Only Member 14 has a CC of 0.880 (r^2 value of 77.5%), a subtle, yet potentially meaningful difference. A majority of the Multistatic members have a higher correlation to the Truth Run for the 2300 UTC ensemble analyses than the WSR-88D Only members (Figure 5.41). Member 2 has a similar strength storm for both experiments, resulting in a higher correlation between the two experiments, but the Multistatic Member 2 is slightly more correlated to the Truth Run than the WSR-88D Only Member 2, with CCs or 0.306 and 0.292, respectively. The Multistatic analysis has a clearer improvement in the 2300 UTC analysis than previous times, which is owing to the 5 DA cycles completed at this analysis. Guerra et al. (2022) found that it takes 4-6 DA cycles for WoFS to accurately spin up a storm; therefore, the storm is well spun up at this time and the Multistatic experiment produces a slightly more accurate analysis than the WSR-88D Only experiment.

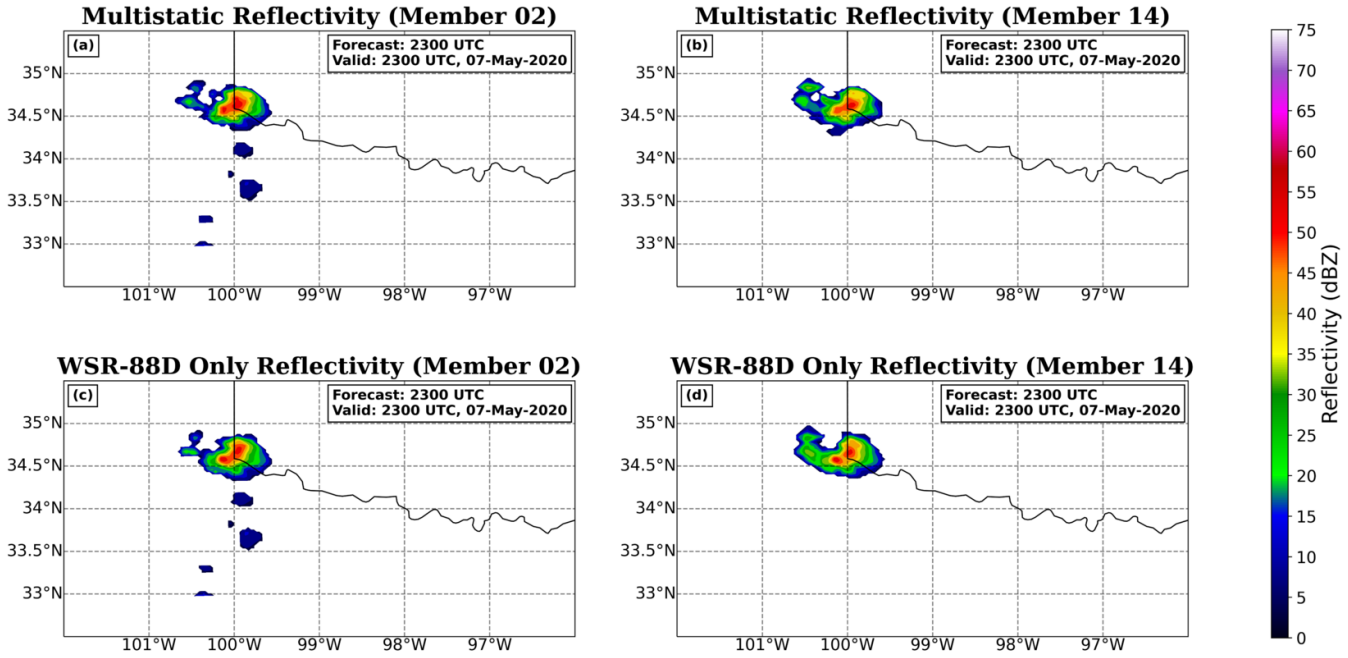

Figure 5.40: (a) Multistatic reflectivity (dBZ) for the highest correlation member, Member 2, (b) Multistatic reflectivity for the lowest correlation member, Member 14, (c) WSR-88D Only reflectivity for the highest correlation member, Member 2, and (d) WSR-88D Only Reflectivity for the lowest correlation member, Member 14.

After 7 DA cycles, the 2330 UTC ensemble analyses continue to look more different between the two experiments (Figure 5.36). The Truth Run storm has completed the split and a robust left-mover remains in the domain. Both experiments accurately analyze the right-mover, but the intensity of the right-mover more closely resembles the Truth Run in the Multistatic members (Figure 5.42), while the WSR-88D Only members tend to have a slightly weaker right-mover. Member 9 has the highest correlation between the Multistatic experiment and WSR-88D Only experiment with a CC of 0.980 while Member 11 has the lowest correlation between the experiments with a CC of 0.709. The CCA does not necessarily match the subjective analysis, as a majority of the WSR-88D Only members have a higher correlation to the Truth Run than the Multistatic members. In fact, only Multistatic Members 1, 6, 10, and 13 have a higher correlation to the Truth Run than the corresponding WSR-88D Only members. As noted in previous sections, the storm is complex at this time and the degradation in quality of the analyses is well documented (Figure 5.6). The Multistatic members tend to have strong spurious convection to the west of primary storm, which is not shown in the WSR-88D Only members. It is likely that the higher CCs for the WSR-88D Only experiment are driven by the lack of spurious convection to the west of the primary storm. However, the developing right-mover is more accurately analyzed in the Multistatic experiment than the WSR-88D Only experiment, and it is clear that the spurious convection to the west is not the primary storm. Therefore, despite the analysis quality degrading from 2300 UTC to 2330 UTC, the Multistatic members more accurately represent the dominant storm than the WSR-88D Only members. As a result, the Multistatic experiment produces a more accurate analysis than the WSR-88D Only experiment for the highest impact storm in the domain, but with a stronger over prediction of spurious convection trailing the splitting storm.

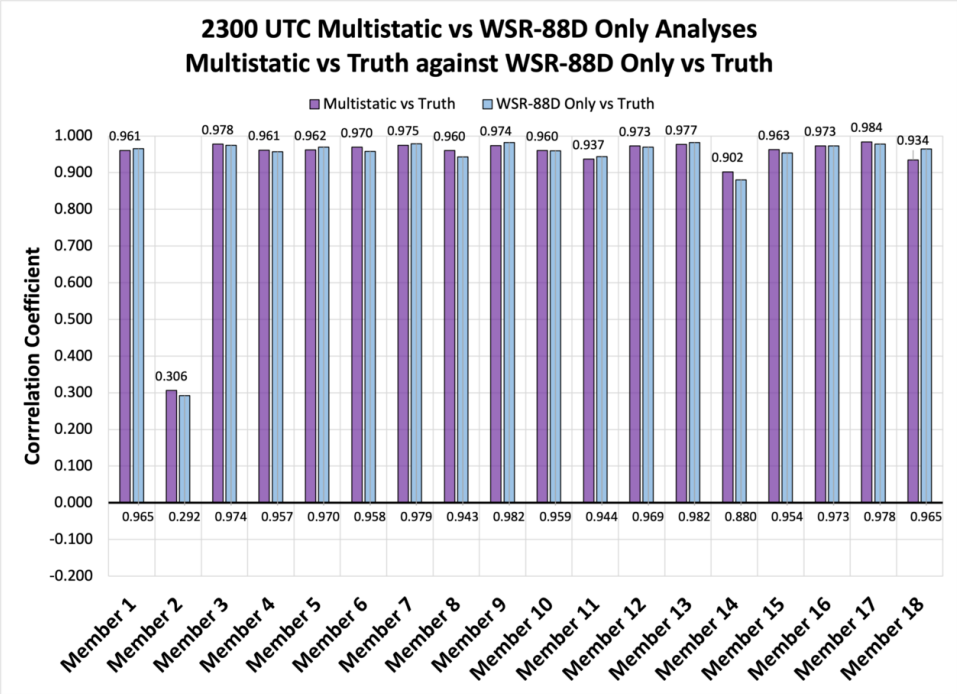

Figure 5.41: 2300 UTC ensemble analysis correlation coefficient for the Multistatic vs Truth Run (purple) experiment plotted against the WSR-88D Only vs Truth Run (blue) ensemble analysis correlation coefficient. The correlation value above the bars is for the Multistatic vs Truth Run experiment and the correlation values closest to the x-axis are for the WSR-88D Only vs Truth Run experiment. Multistatic average correlation coefficient is 0.925 and the WSR-88D Only average correlation coefficient is 0.923 for this analysis.

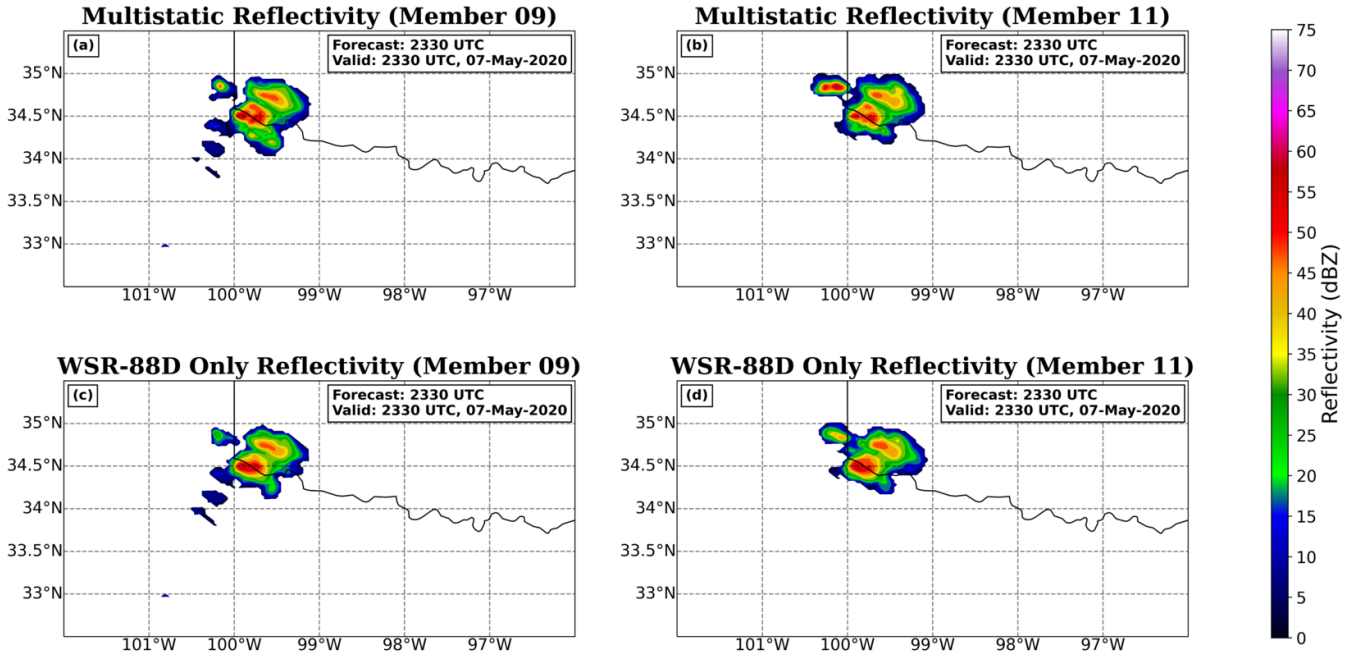

Figure 5.42: (a) Multistatic reflectivity (dBZ) for the highest correlation member, Member 9, (b) Multistatic reflectivity for the lowest correlation member, Member 11, (c) WSR-88D Only reflectivity for the highest correlation member, Member 9, and (d) WSR-88D Only Reflectivity for the lowest correlation member, Member 11.

Throughout the forecasts, the correlation between the Multistatic experiment and the WSR-88D Only experiment continually decreased. If the multistatic network had no impact on the Multistatic experiment, the correlations between the two experiments would look much more like the 2200 UTC ensemble analysis for all forecast times. However, since the correlation continually decreases, it is concluded that assimilation of multistatic velocity observations is having an effect on the Multistatic experiment. Additionally, the Multistatic experiment tends to produce more accurate analyses of the Truth Run storm than the WSR-88D Only experiment in subjective analysis. Though differences are subtle, the Multistatic members tend to analyze a stronger dominant storm that more accurately matches the Truth Run storm at the given times. Additionally, the Multistatic member do produce more spurious convection, especially at later initializations, but the dominant right-mover is more accurately analyzed than in the WSR-88D Only members, which have less spurious convection. Both experiments accurately analyze the location of the primary supercell throughout all initializations, but the Multistatic consistently produces more accurate intensities.

5.4.1.2 Ensemble Forecasts

A summary of the member average correlation between the Multistatic experiment and the WSR-88D Only experiment is shown in Figure 5.43. Following the nearly identical 2200 UTC forecasts, more differences between the Multistatic experiment and the WSR-88D Only experiment appear in the 2215 UTC forecast. However, there is a lot of variability in how the two experiments differ throughout the forecast. Inconsistent variations in intensity of the predicted storm are present across the two experiments, including members that incorrectly predict storm dissipation. For the 2215 UTC forecast, 11 of the 18 Multistatic members have a higher member average correlation to the Truth Run than the WSR-88D Only members (Figure 5.44). The Truth Run at 0010

and 0200 UTC is shown in Figure 5.45. The lowest forecast correlation between the Multistatic and WSR-88D Only experiments occurs in Member 7 at 0200 UTC, with a CC of 0.441 (Figure 5.46). The lowest correlation between the Multistatic experiment and the WSR-88D Only experiment is the most interesting, as it suggests that the largest differences are occurring between the two experiments. The Multistatic storm at 0200 UTC is further north, while the WSR-88D Only storm is further south and nearly outside of the Truth Run domain. However, the Truth Run storm is further south than the Multistatic storm, but further west than the WSR-88D Only storm (Figures 5.45 and 5.47). The second lowest correlation throughout the 2215 UTC forecast occurs in Member 14 at 0010 UTC with a CC of 0.500. Member 14 has stronger reflectivity to the south in the Multistatic experiment, while there is stronger reflectivity to the north in the WSR-88D Only experiment. The Multistatic experiment has stronger reflectivity than the Truth Run at this time and subjective analysis confirms that the Multistatic storm is located nearly identically to the Truth Run storm. However, the WSR-88D Only storm is located slightly further west than the Truth Run storm, suggested by the negative values to the west.

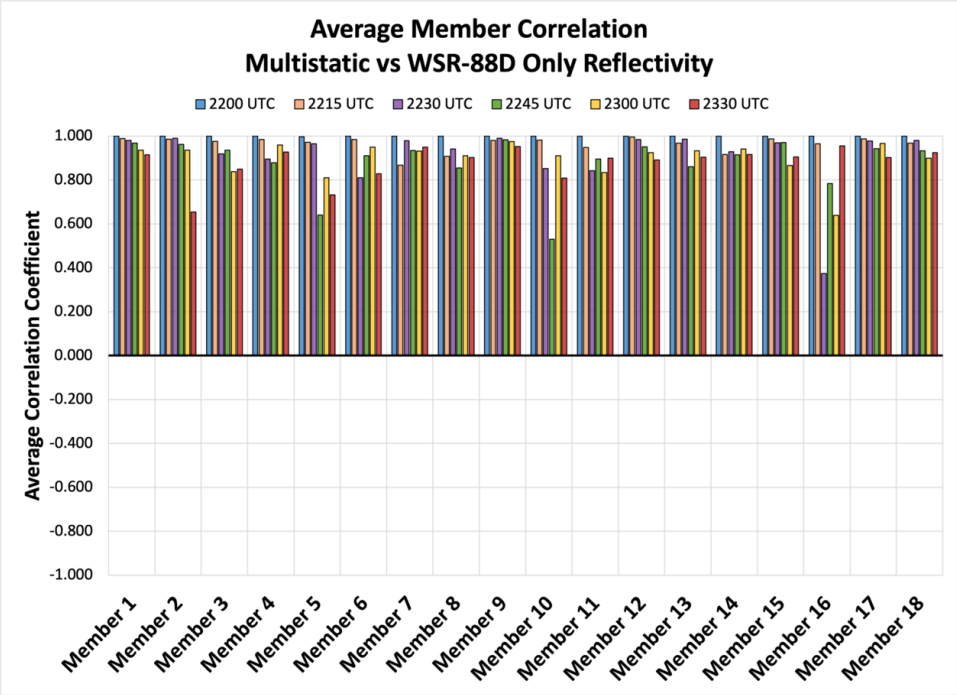

Figure 5.43: Average correlation coefficient for each member for each forecast: 2200 (blue), 2215 (orange), 2230 (purple), 2245 (green), 2300 (yellow), and 2330 UTC (red).

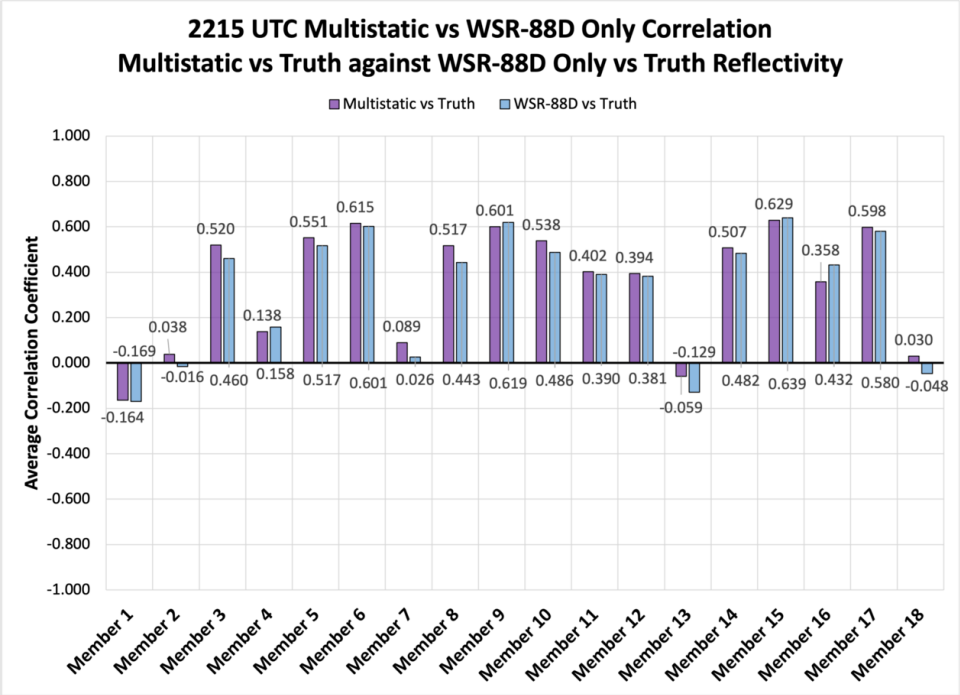

Figure 5.44: Member average correlation coefficient for the Multistatic vs Truth Run (purple) experiment plotted against the WSR-88D Only vs Truth Run (blue) member average correlation coefficient for the 2215 UTC forecast. The average value is plotted nearest the top of the bar for the Multistatic vs Truth Run experiment and nearest the x-axis for the WSR-88D Only vs Truth Run experiment.

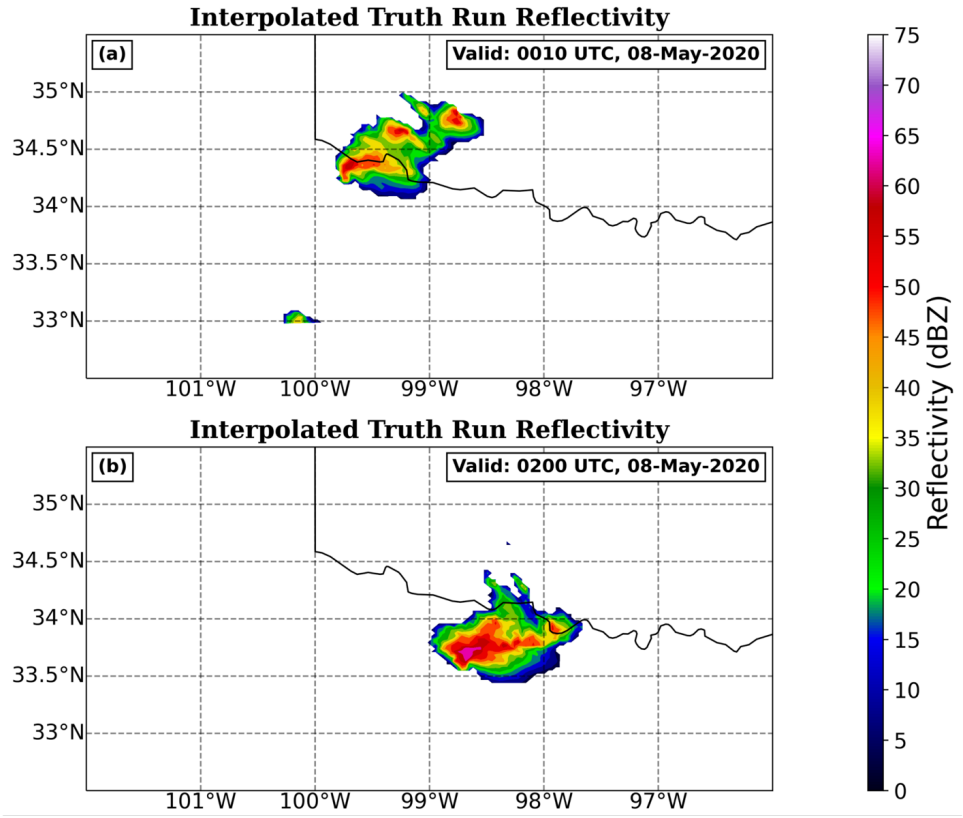

Figure 5.45: Interpolated Truth Run reflectivity (dBZ) at (a) 0010 UTC and (b) 0200 UTC.

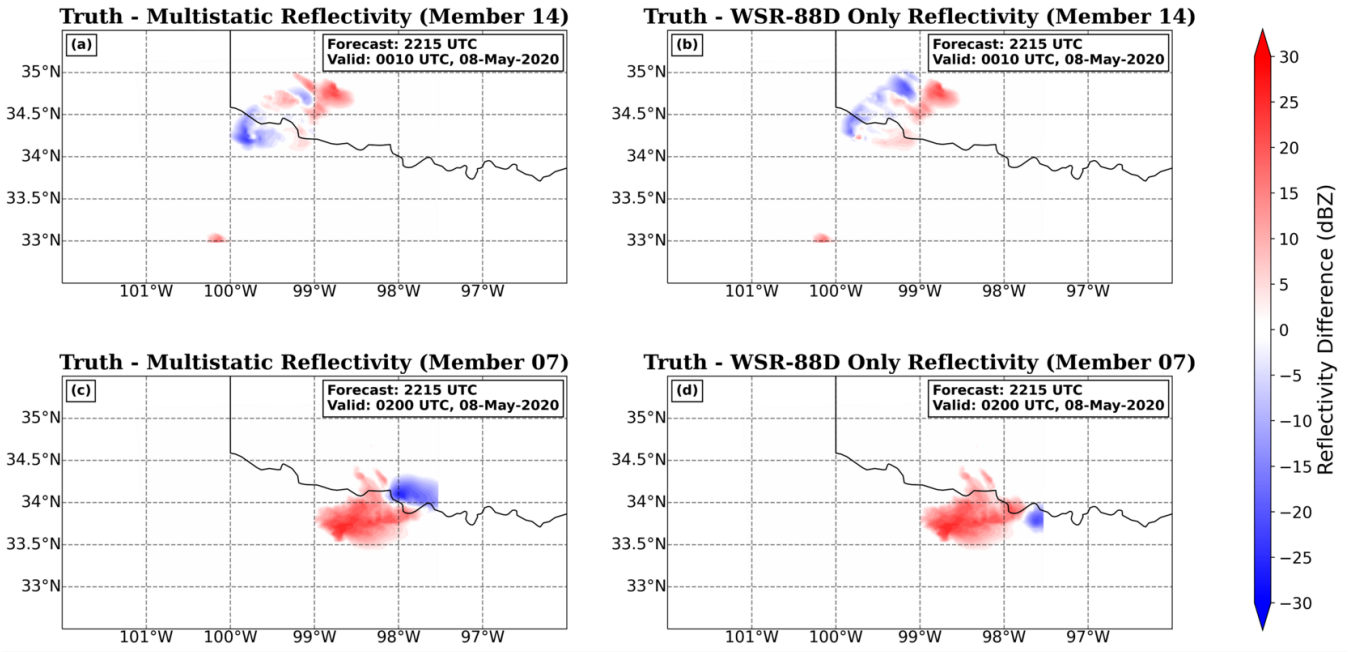

Figure 5.46: Reflectivity difference (dBZ) for the 2215 UTC forecast at 0010 UTC for (a) Truth Run minus Multistatic reflectivity Member 14 and (b) Truth Run minus WSR-88D Only Member 14 is plotted. Reflectivity difference (dBZ) for the 2215 UTC forecast at 0200 UTC for (c) Truth Run minus Multistatic reflectivity Member 7 and (d) Truth Run minus WSR-88D Only reflectivity Member 7 is plotted. Storms are cut off due to reaching the Truth Run boundary, as shown in Figure 4.1.

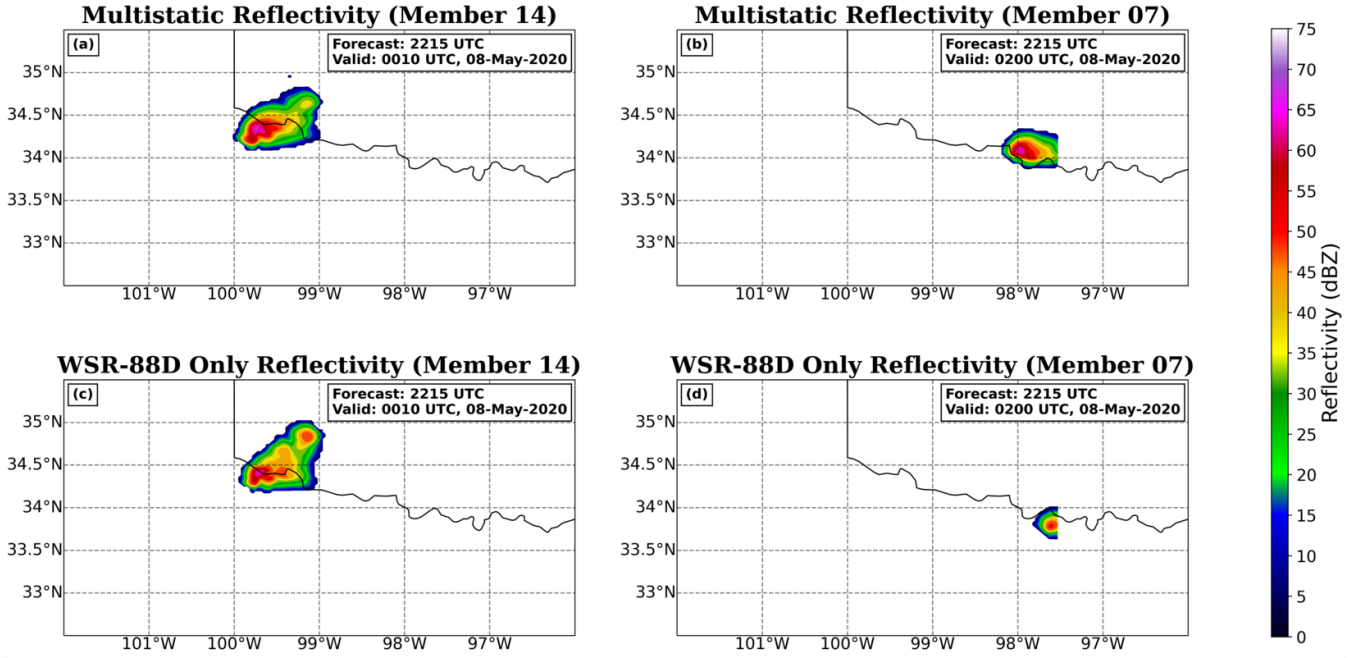

Figure 5.47: Reflectivity (dBZ) for (a) Multistatic Member 14 at 0010 UTC, (b) Multistatic Member 7 at 0200 UTC, (c) WSR-88D Only Member 14 at 0010 UTC, and (d) WSR-88D Only Member 7 at 0200 UTC is plotted. Storms are cut off due to reaching the Truth Run boundary, as shown in Figure 4.1.

Like the previous forecast, the 2230 UTC forecast starts with both the Multistatic experiment and the WSR-88D Only experiment being similar. By 2315 UTC, the Multistatic storm appears larger and stronger for most members, while the storm dissipates in Member 7 in both experiments. The Interpolated Truth Run is shown in Figure 5.48 for 2315 UTC and 0000 UTC. From 2345 UTC until 0045 UTC in the forecast, the Multistatic members tend to have a stronger, more accurately predicted right-moving storm in a majority of the members, but struggle to properly predict the left-mover, whereas the WSR-88D Only experiment predicts the left-mover more accurately. In fact, the Multistatic members predict the left-mover to dissipate well before the Truth Run, while the WSR-88D Only members maintain a weaker left-mover (Figure 5.49). The Multistatic members appear to match the Truth Run right-mover better through 0100 UTC, but all members in both experiments produce accurate analyses of the right-mover throughout the remainder of the forecast. Member 16 has the lowest member average correlation of 0.374, demonstrating that Member 16 is the most different between the two experiments. This difference is caused by the Multistatic Member 16 predicting storm dissipation, while the WSR-88D Only Member 16 maintains the left-mover. While the Multistatic experiment dissipates the left-mover well before the Truth Run, it does consistently produce an accurate forecast of the right-mover, with intensities that match the Truth Run more closely than the WSR-88D Only experiment. Overall, there is a mixed forecast quality in the two experiments, with the Multistatic experiment producing a slightly more accurate prediction of the right-mover, but the WSR-88D Only experiment producing a more accurate prediction of the lower impact left-mover.

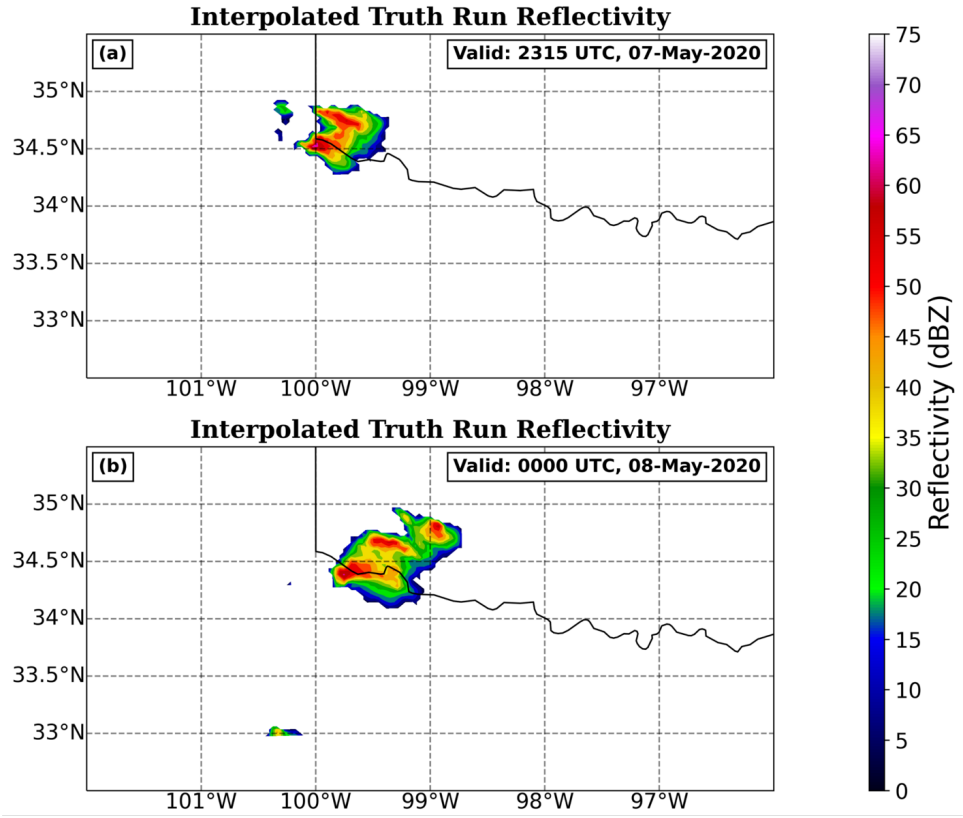

Figure 5.48: Interpolated Truth Run reflectivity (dBZ) at (a) 2315 UTC and (b) 0000 UTC.

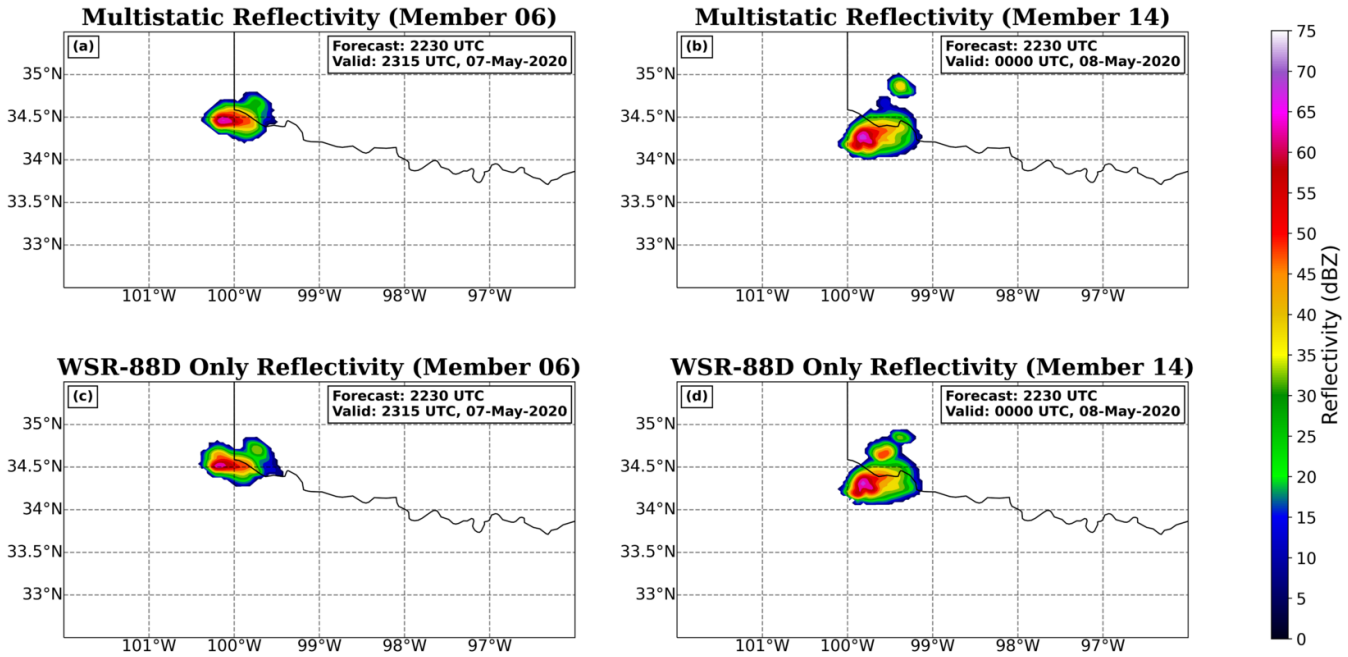

Figure 5.49: Reflectivity (dBZ) for (a) Multistatic Member 6 at 2315 UTC, (b) Multistatic Member 14 at 0000 UTC, (c) WSR-88D Only Member 6 at 2315 UTC, and (d) WSR-88D Only Member 14 at 0000 UTC is plotted.

By the 2245 UTC forecast, many members for both experiments continue to struggle with predicting the split storm in the 2345 UTC to 0045 UTC time period. During this period, there is a robust left-mover in the Truth Run domain, but neither experiment resolves the left-mover, or they have already predicted it to dissipate. The Interpolated Truth Run for 2315 UTC is shown in Figure 5.48 and the Interpolated Truth Run for 2345 UTC is shown in Figure 5.50 for comparison. At 2315 UTC the WSR-88D Only Member 13 has a correlation to the Truth Run of 0.917, while the Multistatic Member 13 has a correlation to the Truth Run of -0.136, showing that the WSR-88D Only Member 13 was far outperforming the Multistatic Member 13 at this time (Figure 5.51). This under performance by the Multistatic Member 13 is clearly shown in Figure 5.52, where the difference between the Multistatic experiment and the WSR-88D Only experiment is clearly indicated by the large changes in positive and negative values. By 0015 UTC, most members for both experiments produce a dominant right-mover that is stronger than the Truth Run. Once again, the WSR-88D Only members tend to maintain the left-mover longer than the Multistatic members do, which more closely resembles the evolution in the Truth Run. Variable differences in the coverage of spurious convection and prediction of the right-mover are seen between members of the two experiments.

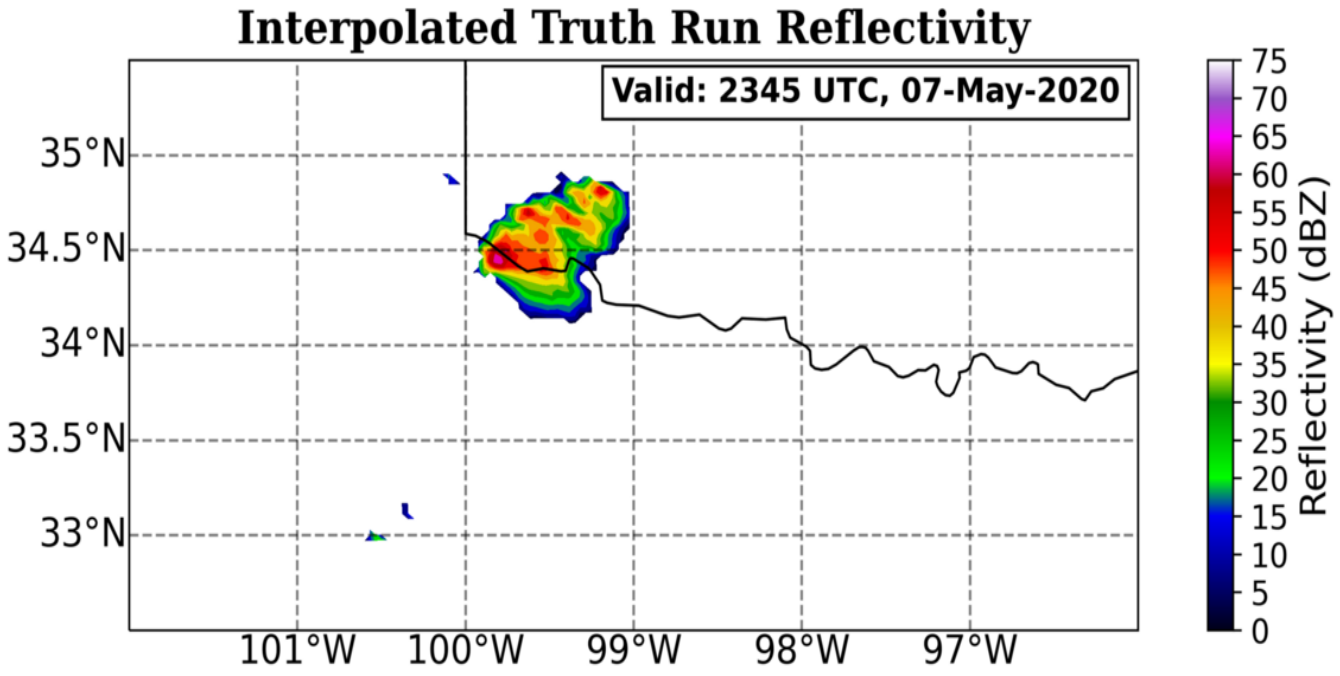

Figure 5.50: 2345 UTC Interpolated Truth Run reflectivity in dBZ.

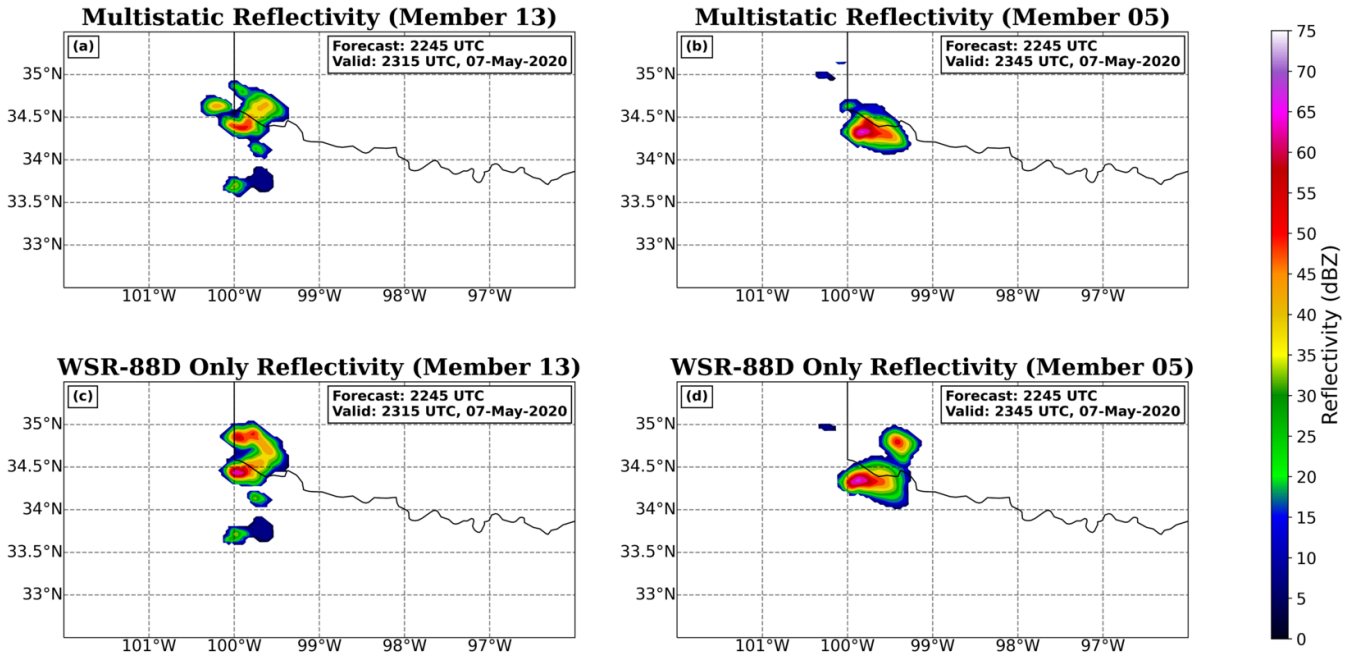

Figure 5.51: Reflectivity (dBZ) for (a) Multistatic Member 13 at 2315 UTC, (b) Multistatic Member 5 at 2345 UTC, (c) WSR-88D Only Member 13 at 2315 UTC, and (d) WSR-88D Only Member 5 at 2345 UTC is plotted.

The 2300 UTC forecast initializes during the storm split, resulting in a nosier forecast from both experiments for the first several timesteps. A majority of the members from both experiments predict a well-defined left-mover but struggle initially to resolve the right-mover. The multistatic network observations appear to be complicating the ensemble analyses and short-term prediction, which is evidenced by many Multistatic members predicting a multiple core structure not present in the Truth Run (Figure 5.22). Until about 0015 UTC, the Multistatic members produce noisy storms with multiple reflectivity cores that do not match the Truth Run, whereas the WSR-88D Only members have already begun to more accurately forecast the Truth Run prior to this time. However, Member 16 still aggressively weakens the right-mover in both experiments. This variability in quality between the Multistatic and WSR-88D Only experiments is reflected in the CC values for the forecasts, where 9 of the 18 Multistatic members are better correlated to the Truth Run (Figure 5.53), suggesting clear differences in forecast quality are not present in the 2300 UTC forecast.

The storm has completed the split by the time the 2330 UTC forecast initializes, but 12 of the 18 members have a decrease in correlation between the Multistatic and WSR-88D Only experiments from the 2300 UTC forecast and the 2330 UTC forecast (Figure 5.43). The robust left-mover is present in the domain for both experiments, where previously both experiments quickly weakened the left-mover as the split completed. However, the Multistatic experiment produces a noisier storm, where the left-mover has not completely moved away from the right-mover and the reflectivity fields are overlapping (Figure 5.23). Additionally, a majority of the Multistatic members continue to predict a right-mover that is stronger than the WSR-88D Only members (Figure 5.54). By 0100 UTC, the right-mover is predicted accurately across all members for both experiments, but the Multistatic members tend to have more spurious convection than the WSR-88D Only members. Overall, the location of the right-mover

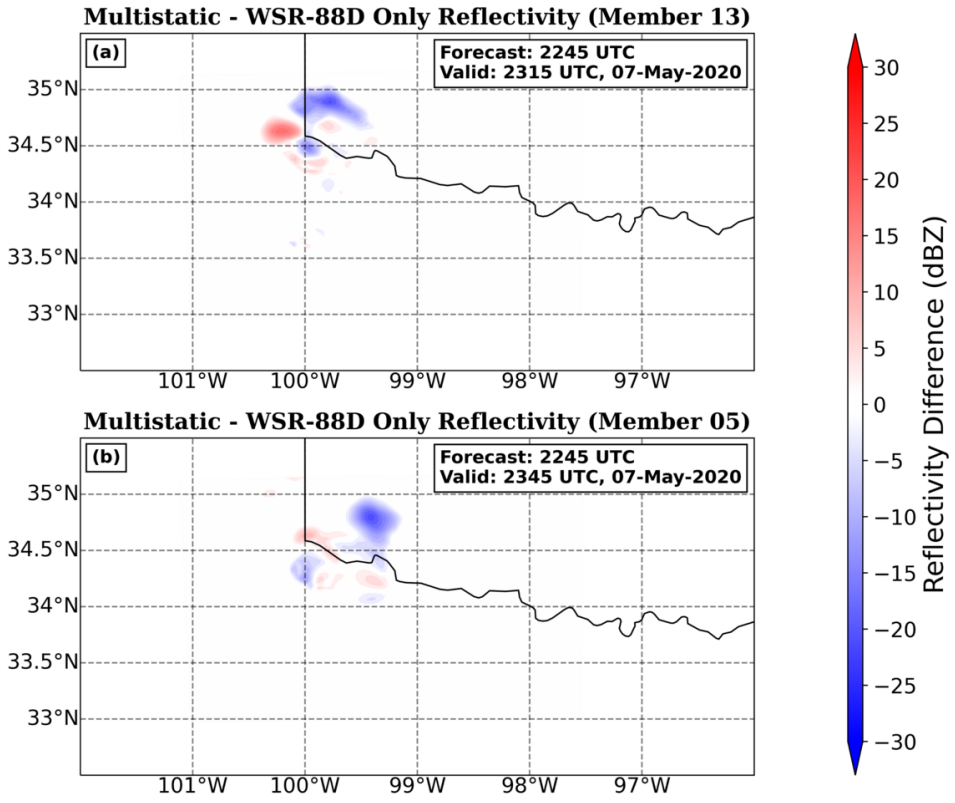

Figure 5.52: Multistatic minus WSR-88D Only reflectivity for (a) Member 13 at 2315 UTC and (b) Member 5 at 2345 UTC. All reflectivity differences are in dBZ.

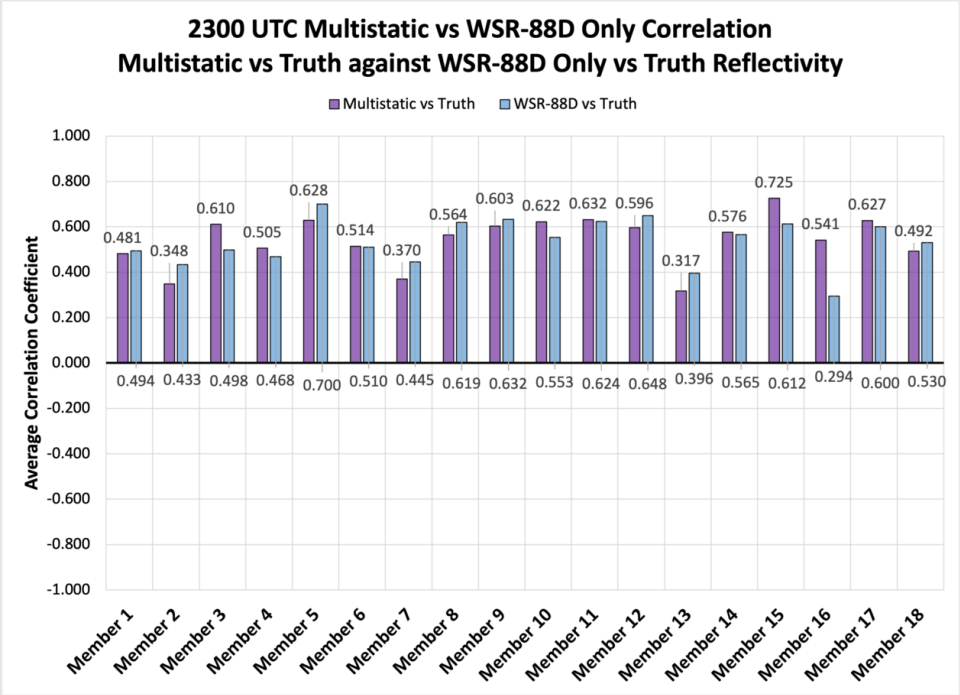

Figure 5.53: Member average correlation coefficient for the Multistatic vs Truth Run (purple) experiment plotted against the WSR-88D Only vs Truth Run (blue) member average correlation coefficient for the 2300 UTC forecast. The average value is plotted nearest the top of the bar for the Multistatic vs Truth Run experiment and nearest the x-axis for the WSR-88D Only vs Truth Run experiment.

is accurately predicted for both experiments. Despite the similarities at later times, the Multistatic experiment more accurately forecasts the right-mover's intensity at earlier times, while the WSR-88D Only experiment tends to forecast the left-mover's intensity more accurately at earlier times. As a result of the right-mover being the primary storm of concern for this forecast, the Multistatic experiment produces a more accurate forecast for this initialization.

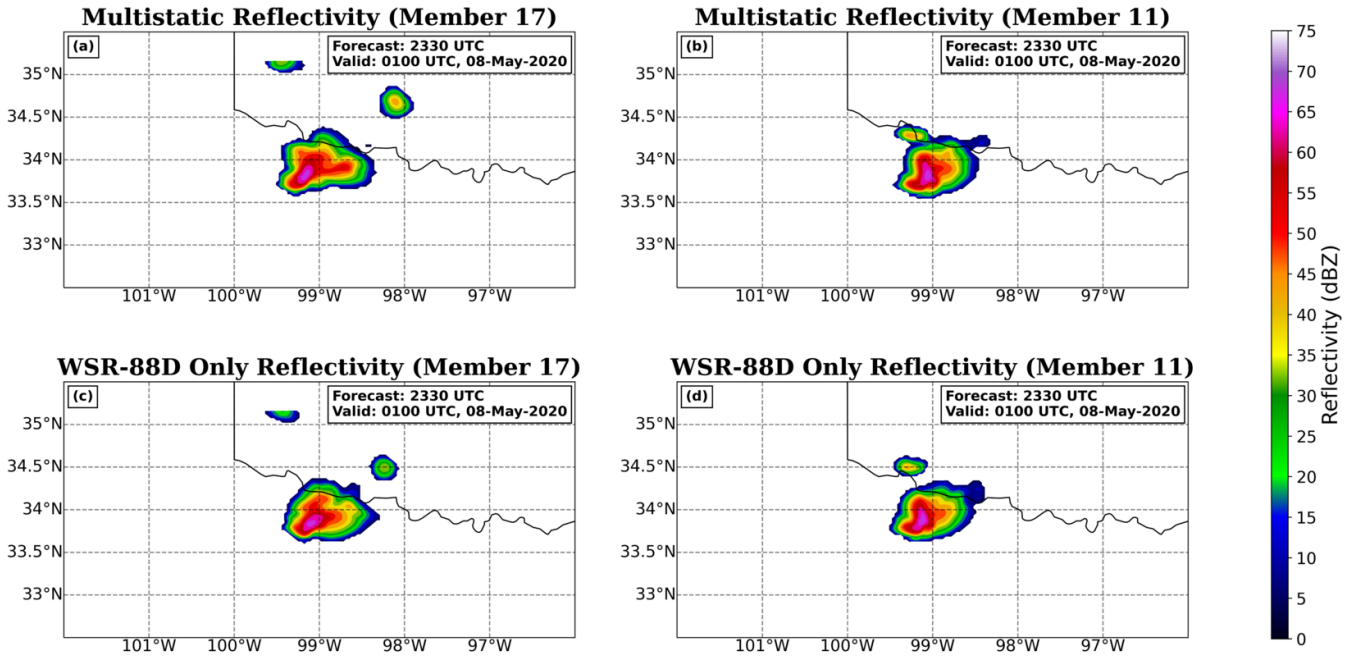

Figure 5.54: Reflectivity (dBZ) at 0100 UTC for (a) Multistatic Member 17, (b) Multistatic Member 11, (c) WSR-88D Only Member 17, and (d) WSR-88D Only Member 11 is plotted.

Similar to the member average correlation between the Multistatic experiment and the Truth Run for the 2300 and 2330 UTC forecasts, the 2330 UTC forecast exhibits a decrease in the member average correlation between the Multistatic and WSR-88D Only experiments from the 2300 UTC forecast (Figure 5.43). This means that the Multistatic and the WSR-88D Only experiments are more different for the 2330 UTC forecast than for the 2300 UTC forecast. While Guerra et al. (2022) and Stratman et al. (2020) found that more DA cycles produce more accurate forecasts, this is not the case for either experiment, at least in terms of correlation with the Truth Run. The degradation in the correlation to the Truth Run is likely due to the complexity of the storm at this time, as previously mentioned. The Multistatic experiment decreased its member average correlation to the Truth Run for a majority of the members in the 2330 UTC forecast, but still had higher correlations to the Truth Run than previous forecasts (Figure 5.15). Therefore, there is greater ensemble consistency, and a generally more accurate forecast in every member, but a decrease in CC in most members from the 2300 UTC forecast to the 2330 UTC forecast, likely owing to greater storm complexity (Figure 5.55). Both experiments are able to accurately forecast the storm, despite the degradation of correlation to the Truth Run for both experiments, but the Multistatic experiment more accurately forecasts the intensity of the primary storm.

5.4.2 Max Vertical Velocity Analysis

5.4.2.1 Ensemble Analyses

A summary of the WSR-88D Only members' correlation to the Truth Run for the ensemble analyses are shown in Figure 5.56 and can be compared to Figure 5.24, the Multistatic members' correlation to the Truth Run for the ensemble analyses. Due to the lack of assimilated data at 2200 UTC, the ensemble analyses for the 2200 UTC

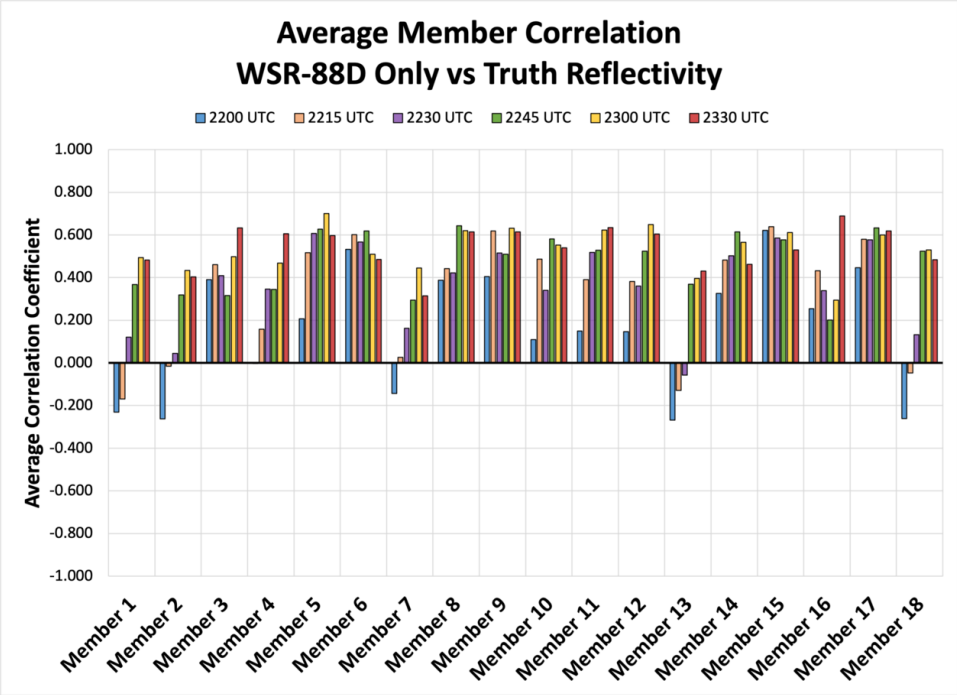

Figure 5.55: Average correlation coefficient for each member for each forecast: 2200 (blue), 2215 (orange), 2230 (purple), 2245 (green), 2300 (yellow), and 2330 UTC (red).

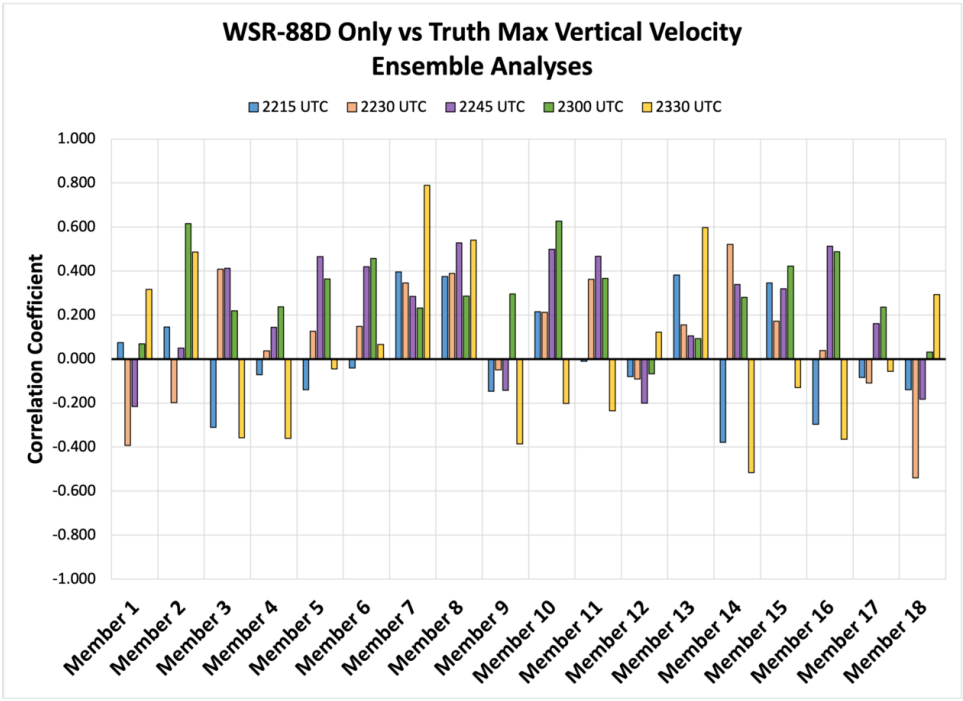

Figure 5.56: Correlation coefficients for each WSR-88D Only member for the ensemble analyses from 2215 (blue), 2230 (orange), 2245 (purple), 2300 (green), and 2330 (yellow) UTC.

forecast are identical between the Multistatic and WSR-88D Only members, with CC values of 1.000 or 0.999 for all members. Similarly, the ensemble analyses for the 2215 UTC run are essentially identical between the Multistatic experiment and the WSR-88D Only experiment, with the lowest CC being 0.997 for Member 15 and the highest CC being 0.999 for several members. Comparing Figure 5.25 to 5.57 shows that while the experiments are essentially identical, neither accurately analyses the MVV in the Truth Run at this time. Much like the Multistatic experiment, which has MVV values around 10 ms^{-1}, the WSR-88D Only experiment has a maximum MVV around 10 ms^{-1}, while the Truth Run has a maximum MVV closer to 20 ms^{-1}. Despite this, the location of the updraft is similar for both experiments, and the location matches the Truth Run.

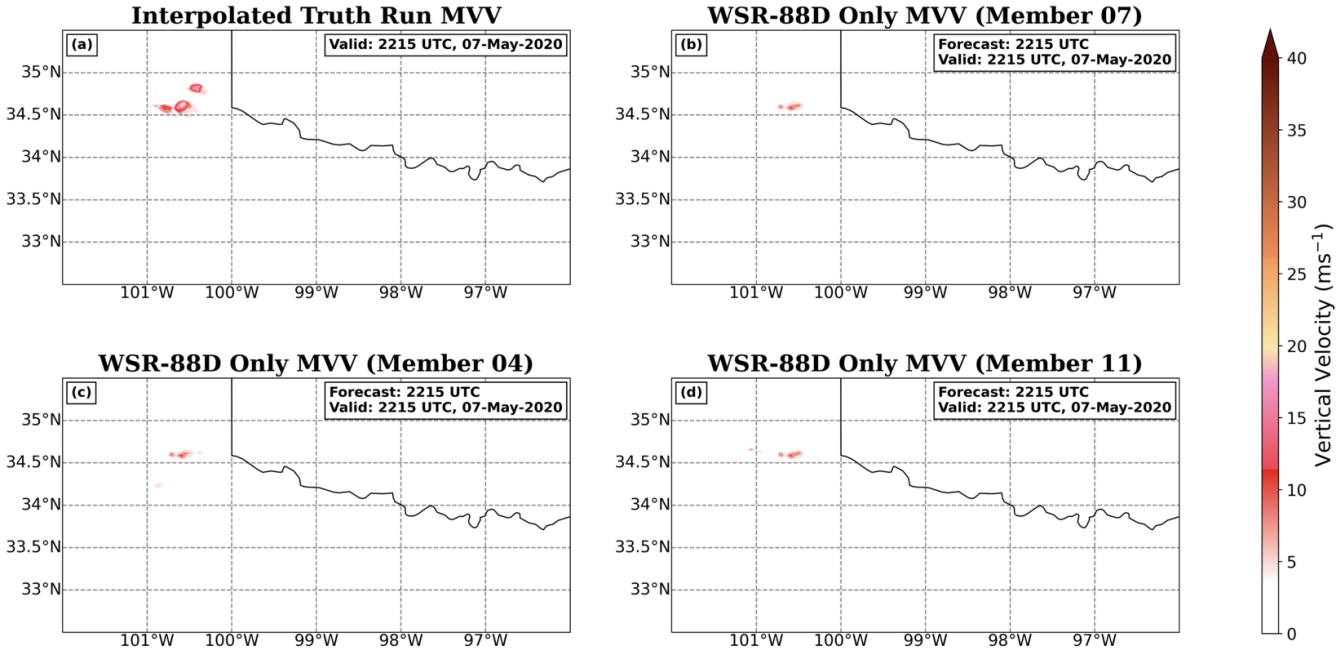

Figure 5.57: (a) Interpolated Truth Run MVV (ms^{-1}) at 2215 UTC on 7 May 2020. For the 2215 UTC WSR-88D Only ensemble analysis, the best performing member (b) Member 7, CC of 0.395, the median performing member (c) Member 4, CC of -0.072 (median: -0.056), and the worst performing member (d) Member 11, CC of -0.010 MVV is plotted.

The spread of the CCs between the Multistatic experiment and the WSR-88D Only experiment increase for the 2230 UTC ensemble analyses, showing that the two experiments are beginning to differ more significantly. The maximum correlation between the two experiments occurs in Member 9, with a CC of 0.994 (r^2 value of 98.7%), while the lowest correlation occurs in Member 11, with a CC of 0.878 (r^2 value of 77.0%). Comparing Figure 5.26 and Figure 5.58 shows that WSR-88D Only Member 18 does not have the spurious updraft to the west of the main updraft like the Multistatic Member 18. However, the spurious updraft to the west is more similar to what the Truth Run shows rather than there being no spurious updrafts. Additionally, WSR-88D Only Member 13 has a slightly stronger updraft, 20 ms^{-1} compared to 15 ms^{-1} in the Multistatic Member 13. The WSR-88D Only Member 13 matches the intensity of the Truth Run updraft, with a maximum MVV value of 20 ms^{-1} in the Truth Run, but a majority of the members from both experiments do not match this intensity. However, Member 13 is not representative of the differences between the Multistatic experiment and the WSR-88D Only experiment. A majority of the Multistatic members have a stronger updraft than the WSR-88D Only experiment, suggesting that the multistatic network observations are spinning up the storm's updraft quicker than the WSR-88D Only experiment. Despite the intensity differences, the location of the main updraft in both experiments matches the Truth Run well, leading to accurate analyses of the updraft location for both experiments.

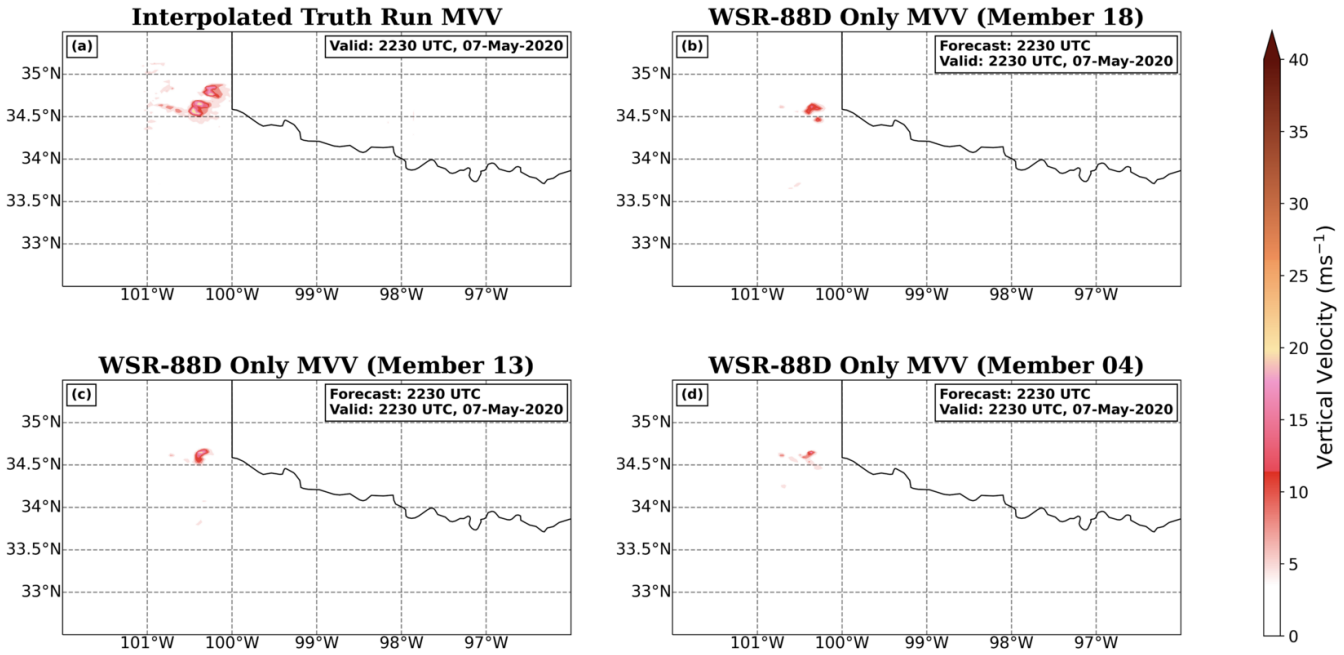

Figure 5.58: (a) Interpolated Truth Run MVV (ms^{-1}) at 2230 UTC on 7 May 2020. For the 2230 UTC WSR-88D Only ensemble analysis, the best performing member (b) Member 18, CC of -0.539, the median performing member (c) Member 13, CC of 0.156 (median: 0.137), and the worst performing member (d) Member 4, CC of 0.038 MVV is plotted.

The 2245 UTC ensemble analyses have better correlation overall between the Multistatic and WSR-88D Only experiments compared to the previous analyses. The highest correlation between the two experiments is 0.994 (r^2 value of 98.8%), while the lowest is 0.920 (r^2 value of 84.7%). For this time, the two experiments are producing more similar analyses and there are fewer differences between the two. Figure 5.27 shows the Multistatic member most highly correlated to the Truth Run (Member 18), the median Multistatic member (Member 13), and the lowest correlation member to the Truth Run (Member 4). Figure 5.59 shows the corresponding WSR-88D Only members, but Member 13 is not the lowest correlated member to the Truth Run for the WSR-88D Only experiment. Neither experiment matches the expanse of the MVV values in the Truth Run, but only the Multistatic members show a multiple updraft set up. The WSR-88D Only members show a cohesive updraft, while the Multistatic members show two distinct updrafts, which matches the Truth Run more closely. The intensities do not match the Truth Run for either experiment, with the maximum MVV in the Truth Run around 35 ms^{-1} and the maximum MVV in the Multistatic experiment is around 15 ms^{-1} and 10 ms^{-1} in the WSR-88D Only experiment. A majority of the Multistatic members have a stronger updraft at this time than the WSR-88D Only members, which is evidence that assimilating the multistatic network observations is more rapidly spinning up the storm updraft. Additionally, both experiments' Member 13 shows some spurious updrafts around 5 ms^{-1} south of the primary updraft that are not in the Truth Run. The Multistatic experiments produces an accurate analysis of the location of both the updrafts present at this time, while the WSR-88D Only experiments show one updraft that matches the location of the southern-most updraft in the Truth Run. For these reasons, the Multistatic experiments produces a more accurate analysis at this time than the WSR-88D Only experiment.

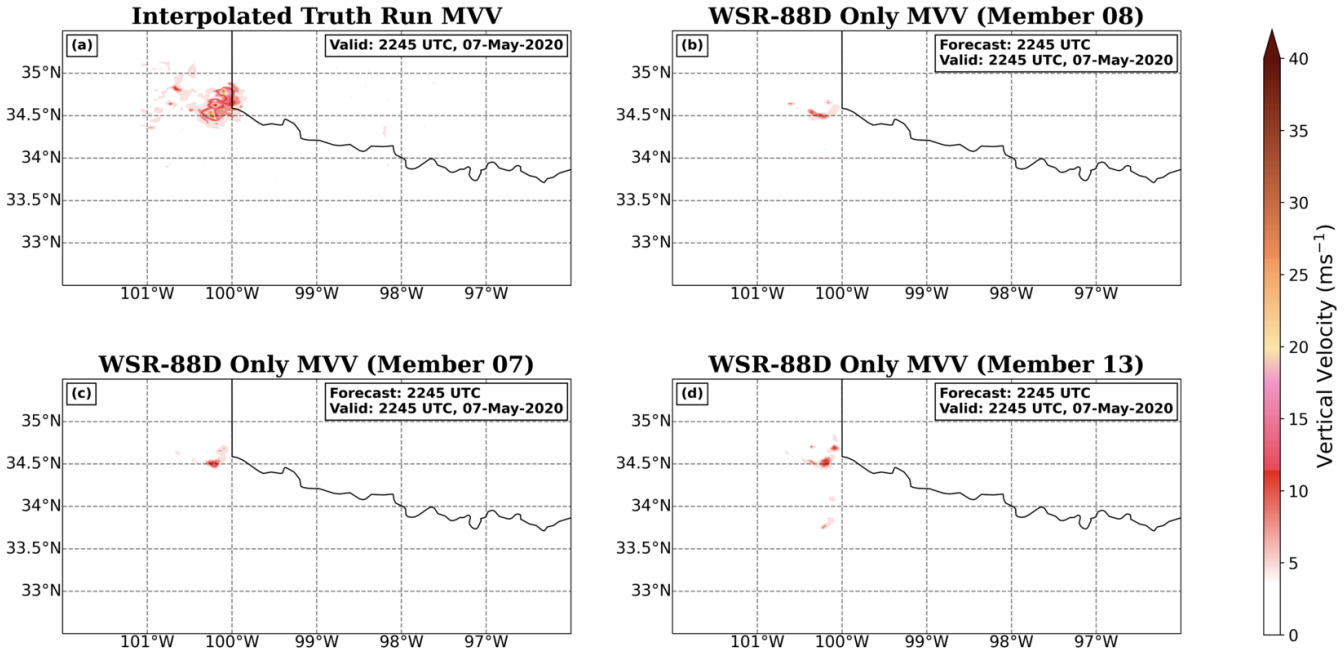

Figure 5.59: (a) Interpolated Truth Run MVV (ms^{-1}) at 2245 UTC on 7 May 2020. For the 2245 UTC WSR-88D Only ensemble analysis for (b) Member 8, CC of 0.528, (c) Member 7, CC of 0.285 (median: 0.302), and (d) Member 13, CC of 0.106 MVV is plotted.

Following 5 completed DA cycles, the spread in the correlations between the Multistatic and WSR-88D Only experiments have increased again. For the 2300 UTC ensemble analyses, the highest correlation is 0.992 (r^2 value of 98.3%) and the lowest is 0.874 (r^2 value of 76.4%), showing that the two experiments are once again becoming more different from one another. The Truth Run has a dominant southern updraft with a slightly weaker updraft to the northeast, which is the left-mover. Both experiments have this left-mover updraft to the northeast that matches the location of the Truth Run left-mover updraft (Figures 5.28 and 5.60). Both experiments have updrafts associated with the right-mover and the left-mover, but the right-mover updraft in the WSR-88D Only experiment tends to be larger than the Multistatic experiment. The two updrafts are nearly the same strength in both experiments, except WSR-88D Only Member 2, which shows a stronger right-mover. Neither experiment matches the intensity of the Truth Run, with the maximum MVV values in the Truth Run around 35 ms^{-1}, while the Multistatic and WSR-88D Only experiments have a maximum MVV value around 15 ms^{-1}, neglecting WSR-88D Only Member 2. Despite the intensity differences, both experiments accurately analyze the location of the left-mover updraft, while the right-mover updrafts tend to be displaced slightly south of where it is in the Truth Run.

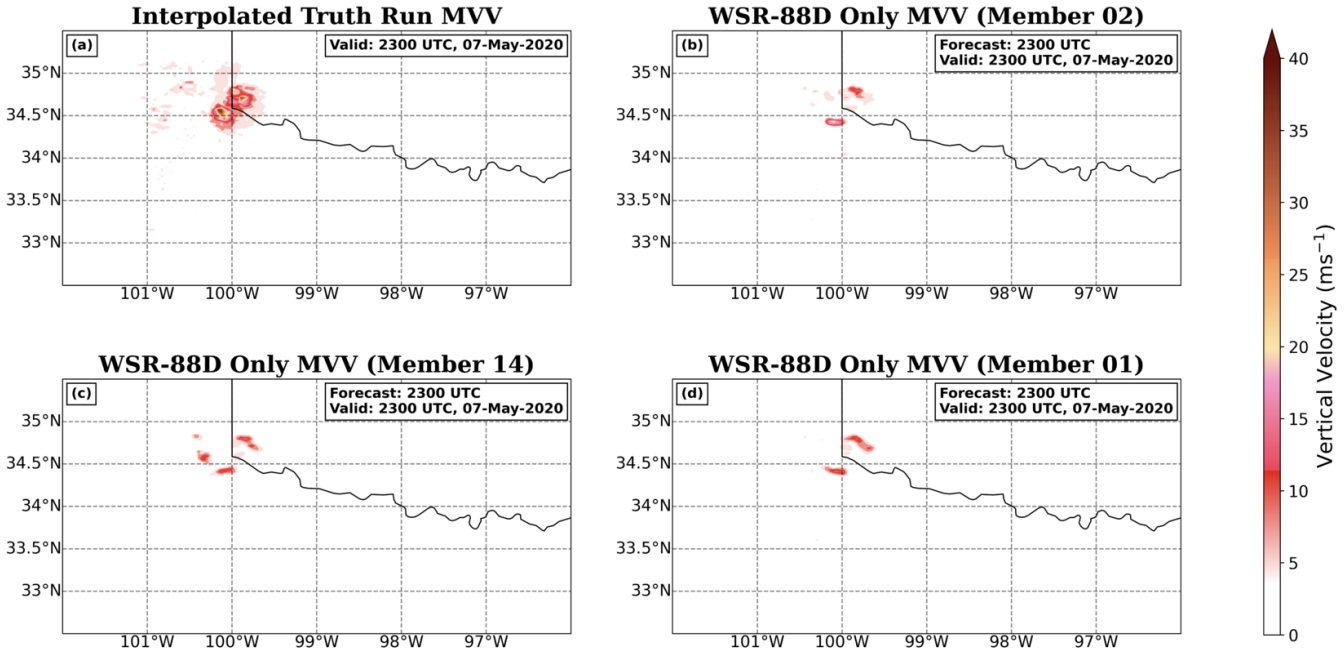

Figure 5.60: (a) Interpolated Truth Run MVV (ms^{-1}) at 2300 UTC on 7 May 2020. For the 2300 UTC WSR-88D Only ensemble analysis for (b) Member 2, CC of 0.616, (c) Member 14, CC of 0.281 (median: 0.283), and (d) Member 1, CC of 0.069 MVV is plotted.

Similarly for the 2330 UTC ensemble analyses, the correlation spread has continued to increase between the Multistatic and WSR-88D Only experiments. The highest correlation for the 2330 UTC analysis is 0.972 (r^2 value of 94.5%), while the lowest correlation is 0.463 (r^2 value of 21.4%). This decrease in correlation is expected, as previous discussion shows the degradation of analysis quality at this time. The Truth Run is a large, cohesive storm with a strong right-mover updraft and a weaker, yet still robust, left-mover updraft. The WSR-88D Only experiment has fewer spurious updrafts than the Multistatic experiment at this time (Figures 5.30 and 5.61). The Multistatic experiments has no obvious dominant right-mover updraft and features a large number of spurious updrafts. Additionally, the WSR-88D Only experiment tends to have a stronger right-mover updraft, with MVV values around 25 ms^{-1}, while the Multistatic experiment has MVV values around 15 ms^{-1}. Overall, the WSR-88D Only experiment more accurately analyzes the right-mover updraft, as the Truth Run has MVV values for the right-mover of around 35 ms^{-1}. Neither experiment accurately analyzes the left-mover updraft, as the Truth Run has MVV values for the left-mover around 25 ms^{-1}, while the experiments have MVV values around 15 ms^{-1} for the left-mover, when the left-mover is easily visible. In addition to the intensity differences, the right-mover updraft in the Multistatic experiment is displaced to the southeast and displaced slightly east in the WSR-88D Only experiment. While the WSR-88D Only experiment produces a more accurate analysis of the right-mover intensity, the left-mover is difficult to determine, and the right-mover is displaced slightly to the east. The Multistatic experiment does not accurately analyze the Truth Run updrafts at this time, as the analyses are noisy with no clear dominant right-mover present.

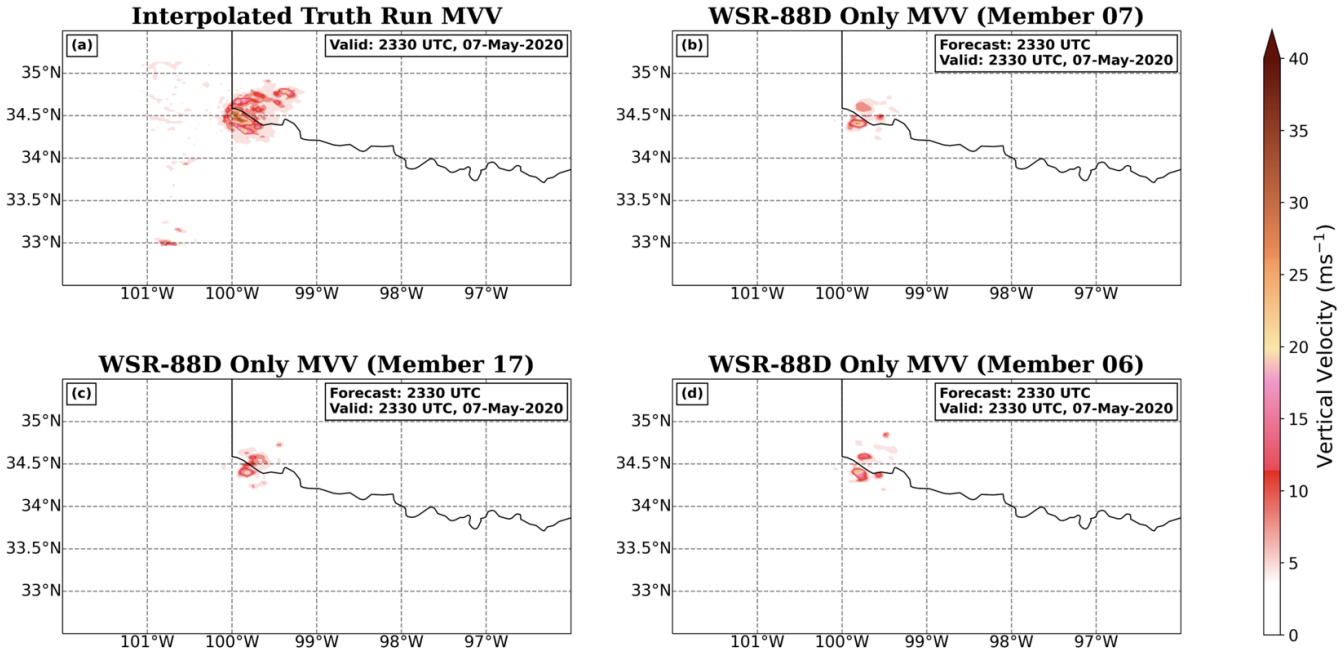

Figure 5.61: (a) Interpolated Truth Run MVV (ms^{-1}) at 2330 UTC on 7 May 2020. For the 2330 UTC WSR-88D Only ensemble analysis for (b) Member 7, CC of 0.789, (c) Member 17, CC of -0.055 (median: -0.050), and (d) Member 6, CC of 0.067 MVV is plotted.

5.4.2.2 Ensemble Forecasts

The remaining forecasts for all initializations of the WSR-88D Only experiment and the Multistatic experiment produce low correlations to the Truth Run, but higher correlations between the two experiments. At 0000 UTC in all forecasts, the storm split has completed, and a robust left-mover remains in the Truth Run domain. Previous discussion shows that neither experiment accurately forecasts the left-mover, but the right-mover is more accurately forecast. Figures 5.32 and 5.62 show representative members from the 2215 UTC Multistatic and the WSR-88D Only experiment forecasts at 0000 UTC, respectively. Both experiments tend to displace the right-mover updraft to the west and south. This west and south displacement of the updrafts is more easily seen in the 2230 UTC forecasts at 0000 UTC (Figures 5.33 and 5.63). Interestingly, the Multistatic Member 11 more accurately analyzes the left-mover updraft at this time, while the WSR-88D Only Member 11 shows a small updraft much further west than the left-mover updraft in both the Truth Run and the Multistatic Member 11.

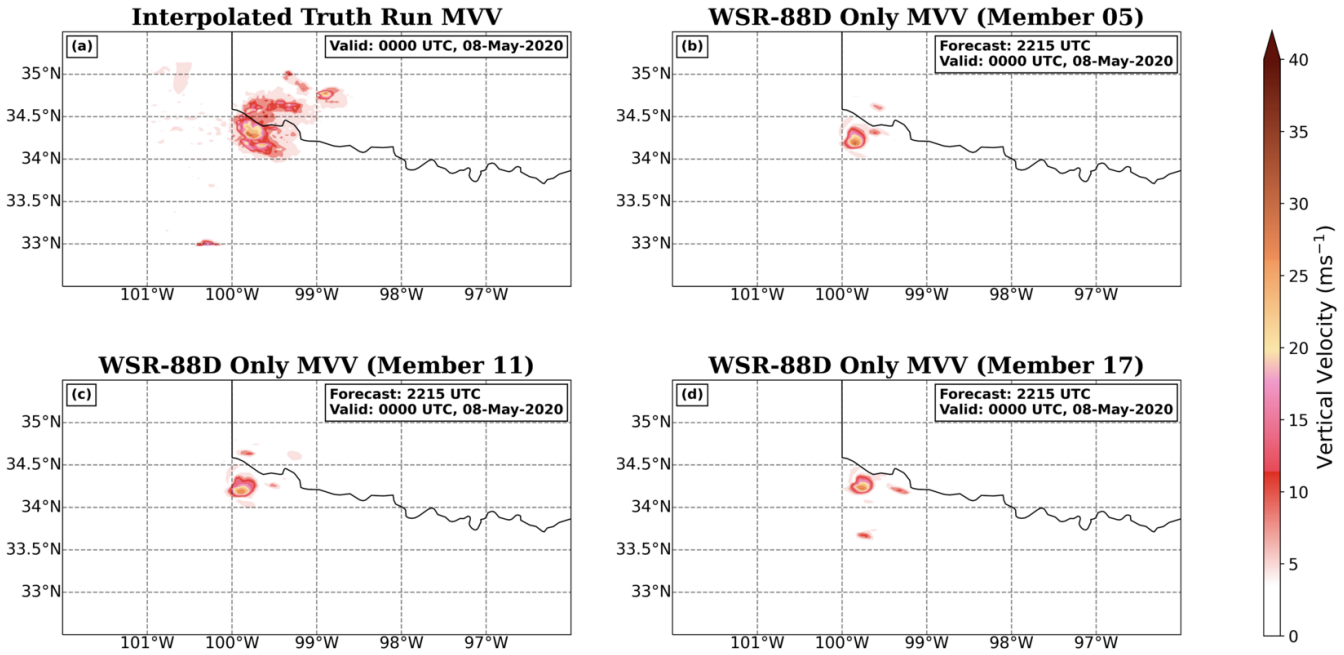

Figure 5.62: (a) Interpolated Truth Run MVV (ms^{-1}) at 0000 UTC on 7 May 2020. MVV is plotted for the 2215 UTC ensemble forecast at 0000 UTC for the WSR-88D Only experiment (b) Member 5 with a southern displacement, (c) Member 11 with a southern displacement, and (d) Member 17 with a southern displacement.

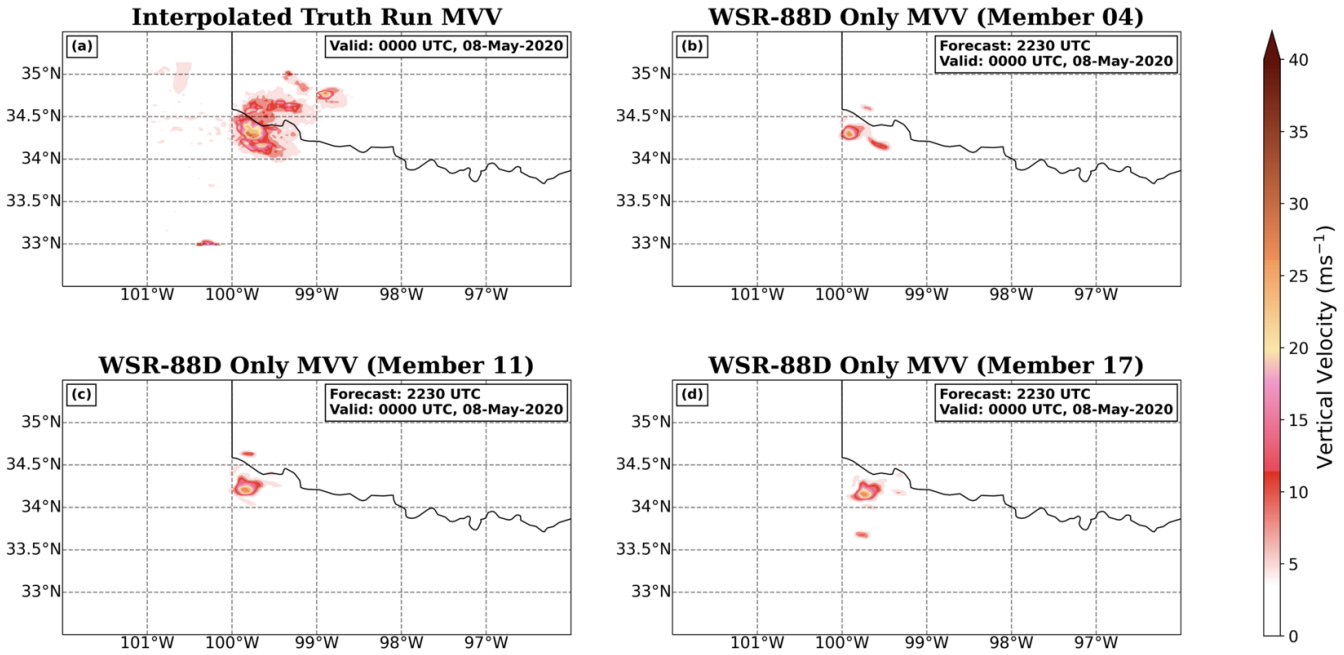

Figure 5.63: (a) Interpolated Truth Run MVV (ms^{-1}) at 0000 UTC on 7 May 2020. MVV is plotted for the 2230 UTC ensemble forecast at 0000 UTC for the WSR-88D Only experiment (b) Member 4 with a southern displacement, (c) Member 11 with a southern displacement, and (d) Member 17 with a southern displacement.

By the 2300 UTC forecast, the displacement between the updrafts becomes more widespread. Figure 5.34 shows Multistatic members with a southern and southeastern displacement of the right-mover updraft, while the WSR-88D Only members tend to have a consistent southeastern displacement of the right-mover updraft (Figure 5.64). Conversely, the left-mover in Members 2 and 12 for both experiments have a more northern and western displacement from the left-mover updraft in the Truth Run, with the Multistatic members having a slightly larger and stronger left-mover updraft. Similarly, at 2330 UTC, the Multistatic members have a southeasterly displacement from the right-mover updraft and a left-mover updraft that more accurately matches the location of the Truth Run (Figure 5.35). However, the WSR-88D Only members tend to have a right-mover updraft that is more predominantly shifted to the east, rather than the southeast (Figure 5.65). Once again, the left-mover updraft is shifted to the west in the WSR-88D Only members and is weaker than the Truth Run's left-mover updraft. This displacement across the experiments suggests that the Multistatic and WSR-88D Only experiment place the storms further to the east and tend to propagate them more quickly to the east than the Truth Run. However, the Multistatic experiments tends to forecast the location of the left-mover more accurately than the WSR-88D Only experiment. Therefore, the experiments propagate the right-mover to the east more rapidly than the Truth Run, but only the Multistatic experiment accurately propagates the left-mover, while the WSR-88D Only experiment lags the left-mover behind the Truth Run.

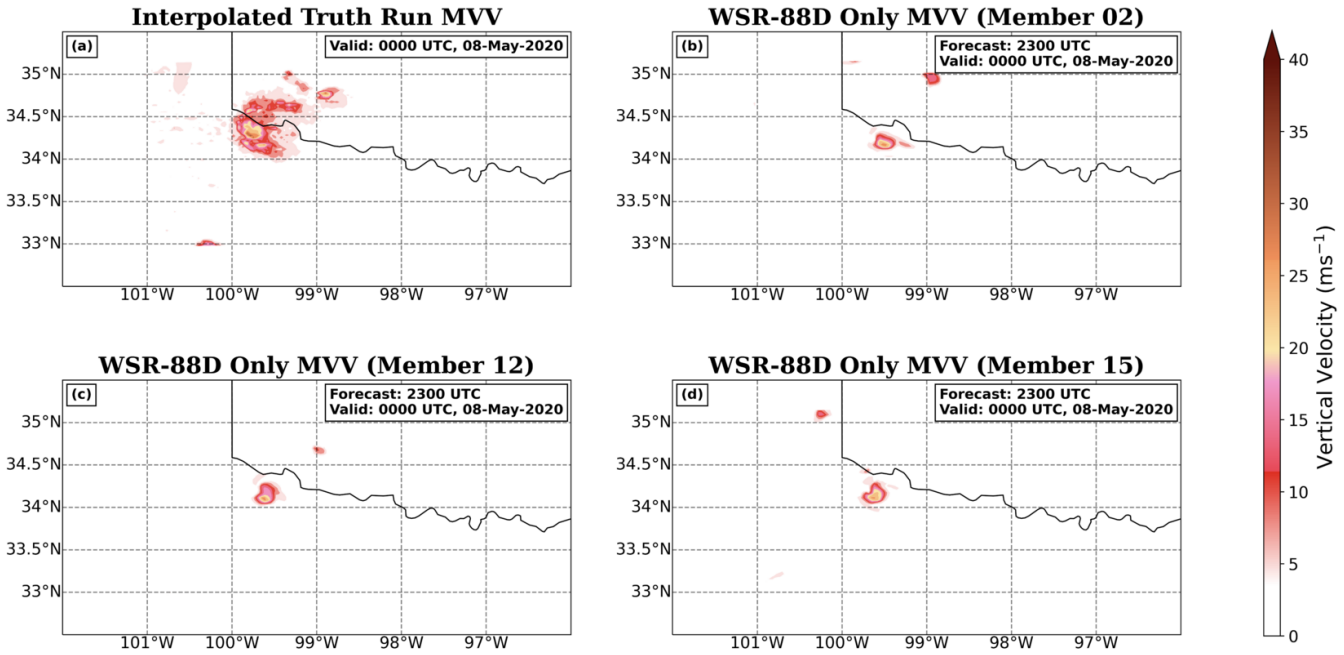

Figure 5.64: (a) Interpolated Truth Run MVV (ms^{-1}) at 0000 UTC on 7 May 2020. MVV is plotted for the 2300 UTC ensemble forecast at 0000 UTC for the WSR-88D Only experiment (b) Member 2 with a southeastern displacement, (c) Member 12 with a southeastern displacement, and (d) Member 15 with a southeastern displacement.

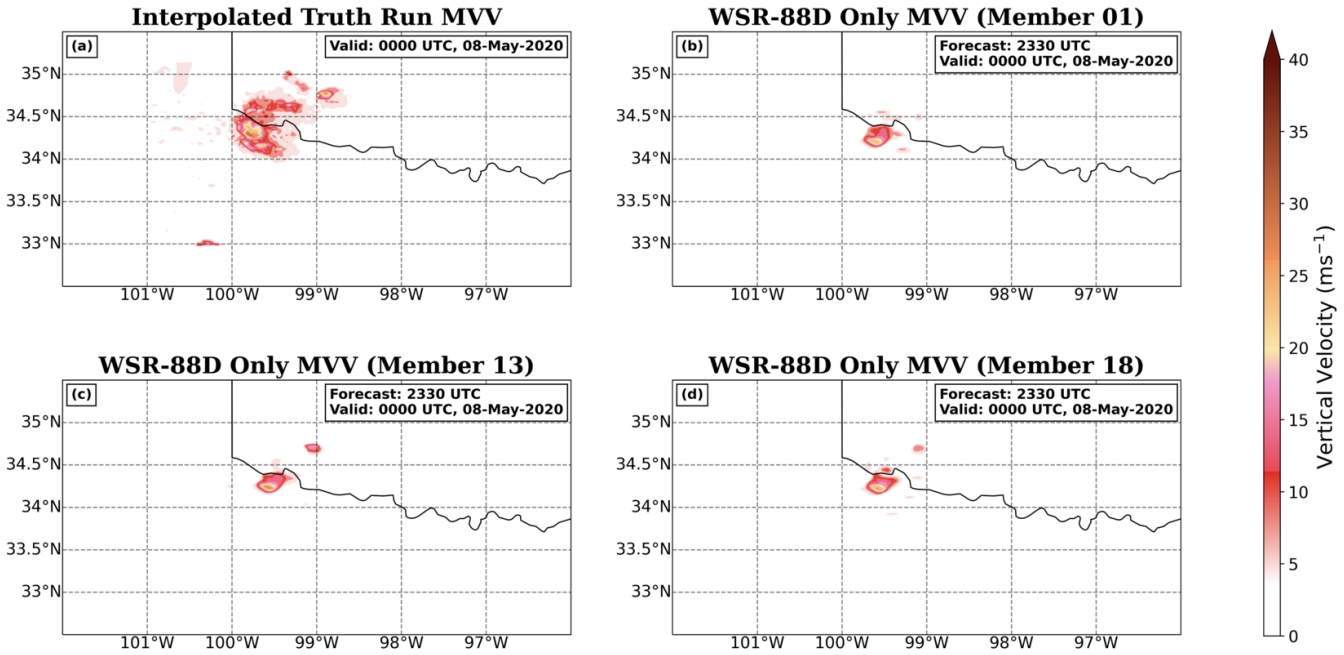

Figure 5.65: (a) Interpolated Truth Run MVV (ms^{-1}) at 0000 UTC on 7 May 2020. MVV is plotted for the 2330 UTC ensemble forecast at 0000 UTC for (b) Member 1 with a southeastern displacement, (c) Member 13 with a eastern displacement, and (d) Member 18 with a southeastern displacement.

5.5 Probability Analysis

A probabilistic 2 to 5-km updraft helicity (UH25; Kain et al. (2008)), analysis is completed using the Neighborhood Maximum Ensemble Probability Swaths method described by Schwartz and Sobash (2017) and Roberts et al. (2019). A 9-km diameter neighborhood is used for the UH25 probability swaths rather than a larger, 15-km or 27-km diameter in order to preserve small-scale variations between the Multistatic and WSR-88D Only experiments. Additionally, all neighborhoods used by WoFS are smaller than the 80 km diameter neighborhood typically used in "next-day" CAMs (i.e., High Resolution Ensemble Forecast). The 2200 UTC UH25 probability swaths at the end of the run are essentially identical between the Multistatic and the WSR-88D Only experiment, as expected due to the lack of bistatic velocity observations assimilated at this initialization (Figure 5.66). The probability for the 2200 UTC forecast is low, around 0.3, and there are no clear swaths of probability of UH25 exceeding 60 $m^2 s^{-2}$, as would be expected for a forecast initialized at the time of convection initiation (Guerra et al. 2022).

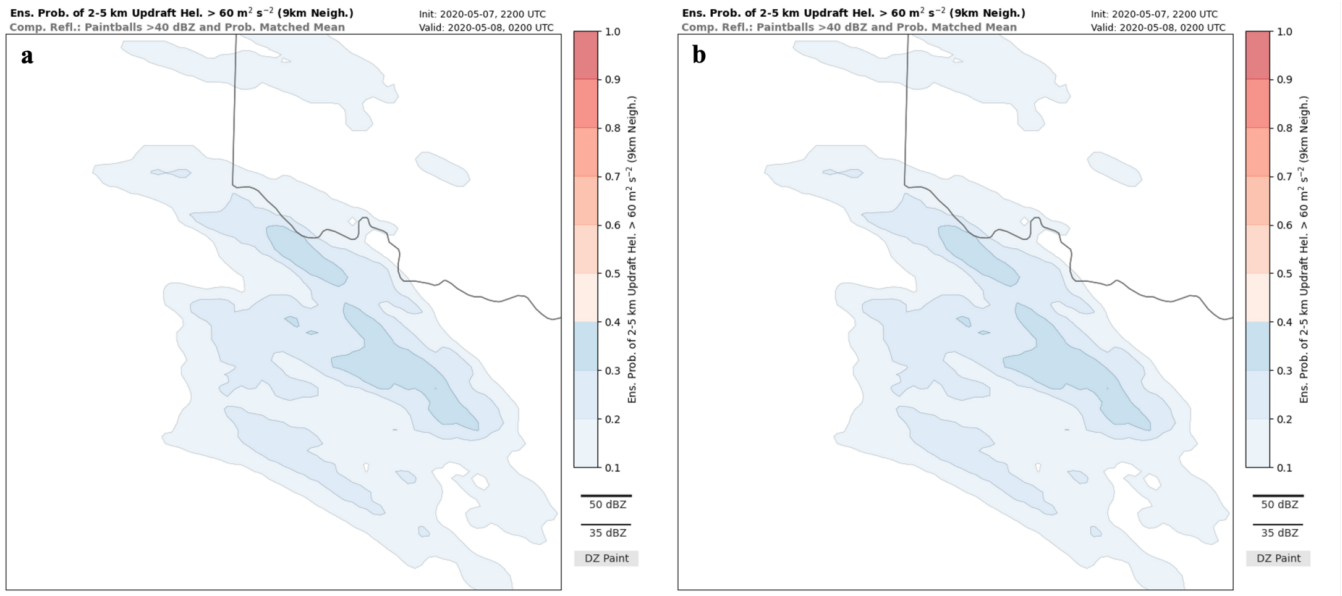

Figure 5.66: Probability of 2 to 5 km updraft helicity exceeding 60 m^2s^{-2} using a 9 km diameter neighborhood for the 2200 UTC forecast for (a) the Multistatic experiment and (b) the WSR-88D Only experiment. The 0200 UTC time step is used to show the probability swath for the entire forecast, corresponding to the Truth Run time.

The 2215 UTC forecasts are dramatically different, with both experiments exhibiting a probability swath of more than 0.8 for UH25 greater than 60 m^2s^{-2} (Figure 5.67). Both experiments have increased the probability of a mesocyclone by nearly 50%, which shows that both experiments have spun an incipient storm extremely quickly. The WSR-88D Only experiment predicts a 90% probability of a mesocyclone with UH25 greater than 60 m^2s^{-2} at this time, suggesting that the WSR-88D Only experiment is more confident in the specific track of the mesocyclone early in the forecast period. The Multistatic experiment is more confident in the mesocyclone track throughout much of the forecast period, with the 0.8 probability extending further to the southeast than the WSR-88D Only experiment. Additionally, the Multistatic experiment shows that there is a 70% probability that the mesocyclone will exceed the threshold slightly further into the storm's life than in the WSR-88D Only experiment, evident by the 0.7 contour extending slightly further to the southeast in the Multistatic experiment. In the latter portions of the forecast, the Multistatic experiment is once again more confident that the strong mesocycle will extend further into the storm's life, evidenced by the 0.6 probability swath extending much further to the southeast in the Multistatic experiment. A more confident prediction of the track of the right-mover is issued in the 2215 UTC Multistatic forecast, as indicated by a longer, narrow swath with higher probabilities of significant UH than the WSR-88D Only experiment.

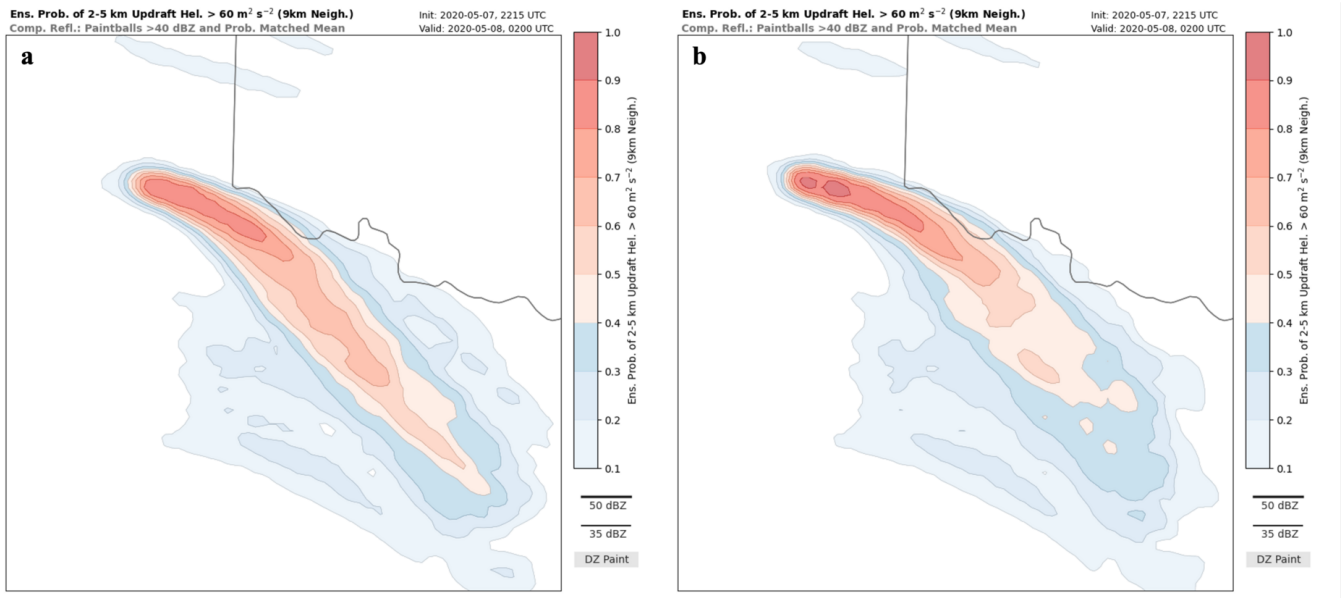

Figure 5.67: As in Figure 5.66, but for the 2215 UTC forecast.

Smaller differences appear between the UH25 probability swaths for the Multistatic and WSR-88D Only experiments in the 2230 UTC forecast. Both experiments have a 80% probability of a mesocyclone with a UH25 exceeding 60 m^2s^{-2} in the early portions of the forecast, but the WSR-88D Only experiment has a split swath with the first swath only having a probability of 70% (Figure 5.68). The Multistatic experiment is more confident in a mesocyclone exceeding the threshold slightly before the WSR-88D Only experiment, evident by a small westward displacement of the initial 0.8 swath in the Multistatic experiment. Additionally, the WSR-88D Only swath is displaced slightly north of the Multistatic swath, suggesting a slightly more northern track in the WSR-88D Only experiment. Later in the forecast, the 0.6 probability contour is slightly further southeast in the Multistatic experiment than in the WSR-88D Only experiment, showing that the Multistatic experiment is slightly more confident in the track of the mesocyclone than the WSR-88D Only experiment. All of these observations suggest that the Multistatic experiment is confident in a strong mesocyclone of UH25 exceeding 60 m^2s^{-2} earlier in the forecast and keeps the probability of this strong mesocyclone longer into the storm's track than the WSR-88D Only experiment. Additionally, the Multistatic experiment suggests a more southerly track than the WSR-88D Only experiment at this time.

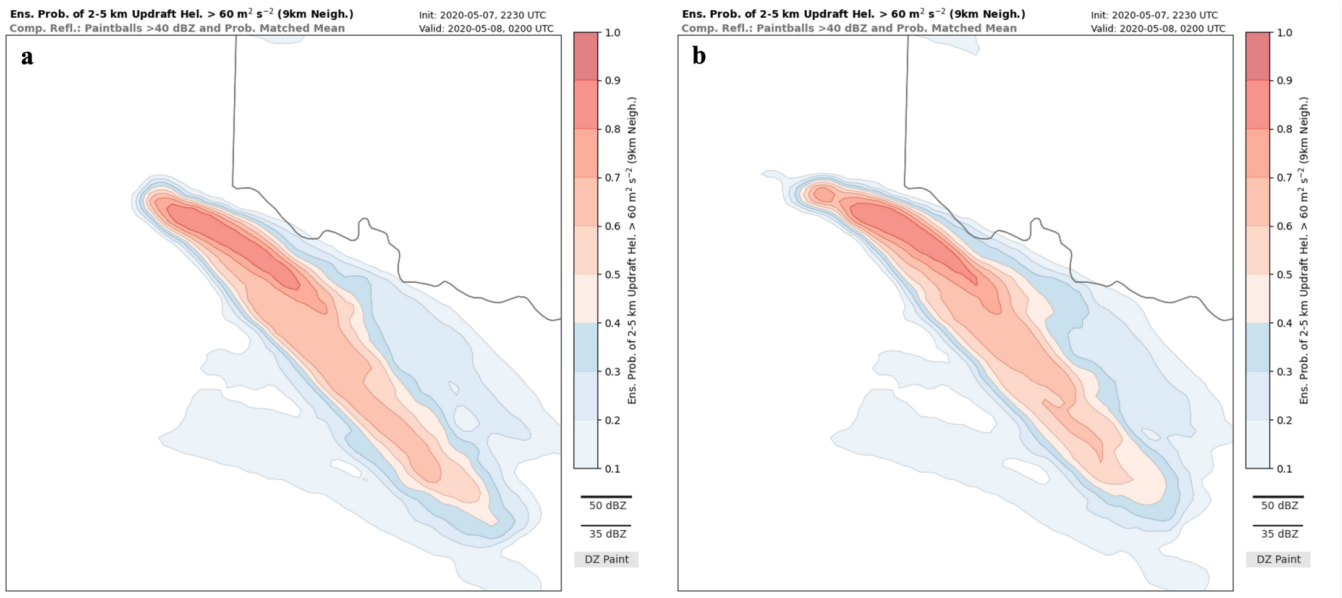

Figure 5.68: As in Figure 5.66, but for the 2230 UTC forecast.

By the 2245 UTC forecast, the UH25 probability swaths for the two experiments have changed significantly. The Multistatic experiment has a maximum probability of 0.9, or 90%, for a mesocyclone exceeding the 60 m^2s^{-2} threshold, while the WSR-88D Only experiment has a maximum probability of 0.8, or 80% (Figure 5.69). At the beginning of the forecast, the Multistatic experiment's 0.8 probability swath starts slightly further west than the WSR-88D Only experiment, and the WSR-88D Only experiment is displaced slightly north, though the displacement has decreased slightly from the 2230 forecast. Later in the forecast, the 0.8 probability swath for the Multistatic experiment once again continues further to the southeast than the WSR-88D Only experiment, resulting in the Multistatic experiment having a longer, and higher, probability swath for a mesocyclone exceeding the threshold than the WSR-88D Only experiment, evident by the longer swath and the 0.9 probability near the early and middle portions of the forecast. Therefore, for the 2245 UTC forecast, the Multistatic experiment has less spread in the location of the storm than the WSR-88D Only case, indicating that the Multistatic experiment is more confident in the prediction of the storm track than the WSR-88D Only experiment.

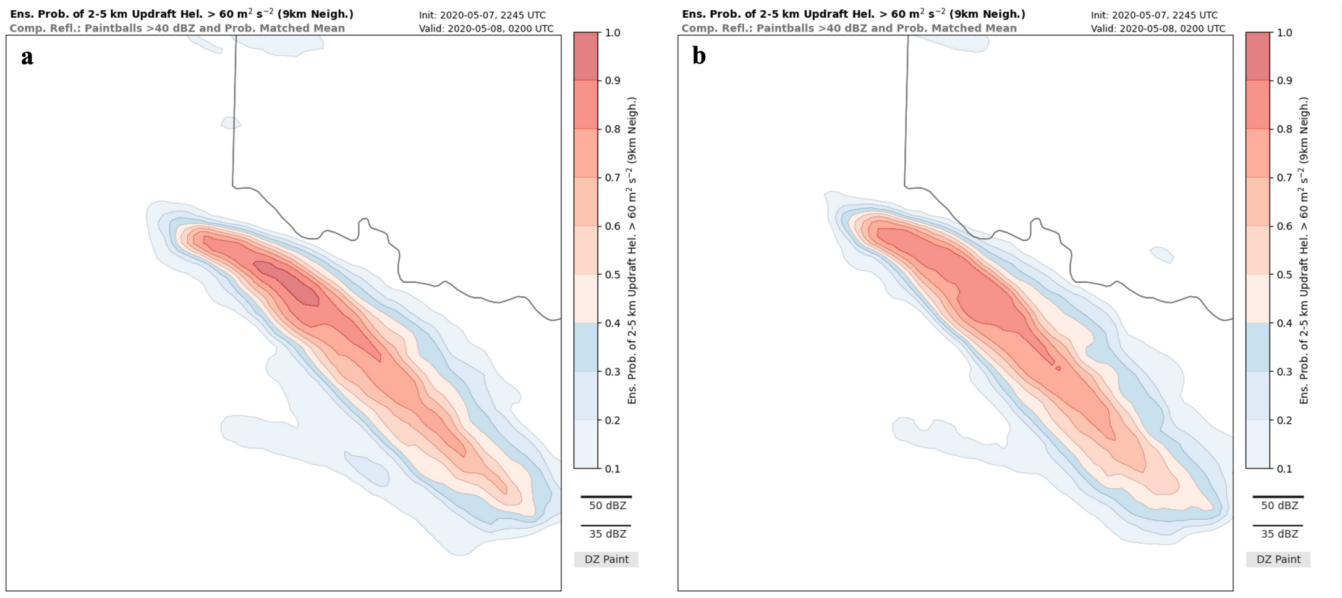

Figure 5.69: As in Figure 5.66, but for the 2245 UTC forecast.

The 2300 UTC forecast shows interesting differences between the Multistatic experiment and the WSR-88D Only experiment. Both experiments have a probability of greater than 90% of a mesocyclone exceeding the 60 m^2s^{-2} threshold, but the WSR-88D Only 0.9 probability swath begins much further west than the Multistatic experiment (Figure 5.70). The 2300 UTC forecast initializes as the storm is beginning to split, but before a robust left-mover is in the domain. Therefore, in the early portions of this forecast, the Multistatic experiment predicts greater spatial spread in the location of the mesocyclone, evident by the 0.8 probability in the earlier portion of the forecast, but the WSR-88D Only experiment is confident in the early track of the right-mover mesocyclone, which is evident by the 0.9 probability early in the forecast. However, as time progresses and the storm continues to mature, the Multistatic experiment becomes more confident that the mesocyclone will exceed the threshold along the center of the predicted track. While the Multistatic experiment is slow to gain confidence in the track of a strong mesocyclone, it is more confident in the mesocyclone's location later into the forecast and the storm's life as evidenced by the 0.9 probability swath extending much further to the southeast than the WSR-88D Only experiment. Therefore, the Multistatic experiment was less confident in the storm's track during the earlier portions of the forecast but became more confident as time progressed. Conversely, the WSR-88D Only experiment was more confident in the mesocyclone track during the split, but less confident in storm track later in later portions of the forecast. The Multistatic experiment was less confident in mesocyclone location during the storm split, further shown in previous discussions, but became more confident in mesocyclone location in later portions of the 2300 UTC forecast.

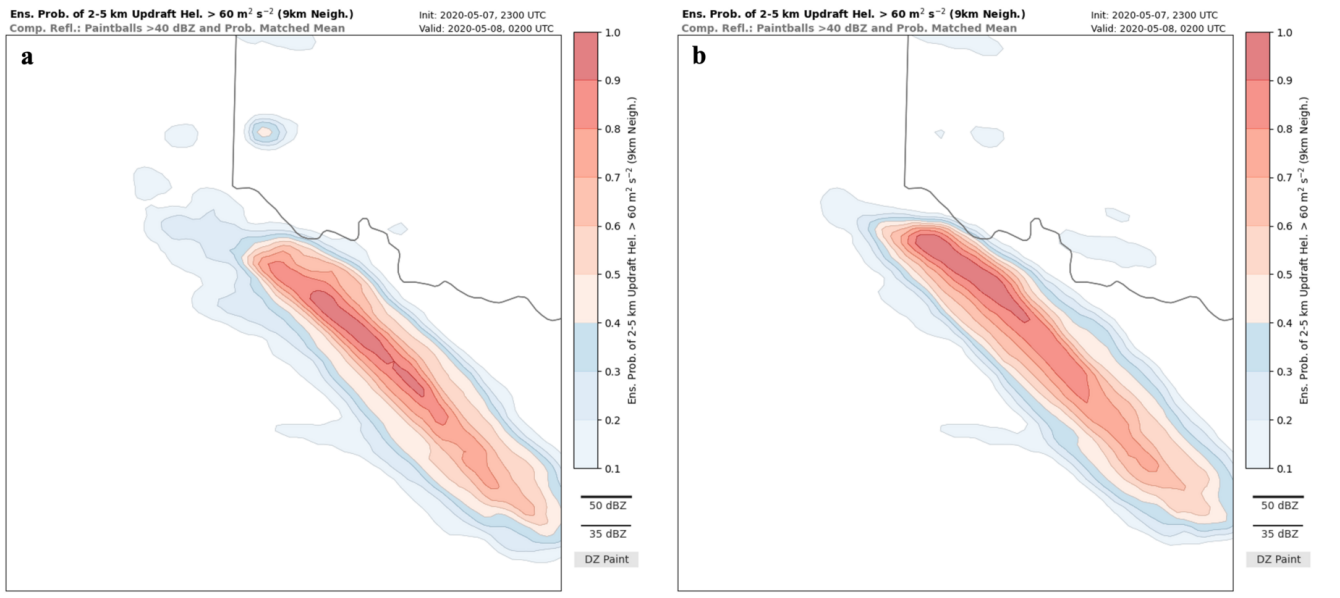

Figure 5.70: As in Figure 5.67, but for the 2300 UTC forecast.

The 2330 UTC forecast shows a further increase in confidence of the mesocyclone track from the previous forecast, with both experiments predicting more than 90% confidence in a mesocyclone exceeded the 60 m^2s^{-2} threshold (Figure 5.71). In the earlier portions of this forecast, the WSR-88D Only experiment has the 0.9 probability starting slightly further west than the Multistatic experiment, suggesting that the WSR-88D Only experiment is analyzing the storm further west than the Multistatic experiment. Additionally, the WSR-88D Only experiment is displaced to north of the Multistatic experiment by a larger amount than the 2300 UTC forecast. While both experiments are confident in a strong mesocyclone, the Multistatic experiment is confident in the mesocyclone track longer than the WSR-88D Only experiment, evident by the Multistatic 0.9 probability swath extending much further southeast than the WSR-88D Only swath. Both experiments are confident in a strong mesocyclone throughout most of the storm's life, which is expected since the storm is well spun up in WoFS at this time and the complexity of the splitting storm has decreased at this time. As a result, the Multistatic experiment continuously produces a probability swath that extends further southeast than the WSR-88D Only experiment. Additionally, the WSR-88D Only experiment consistently displaces the mesocyclone to the north of the Multistatic experiment, while the Multistatic experiment remains further south.

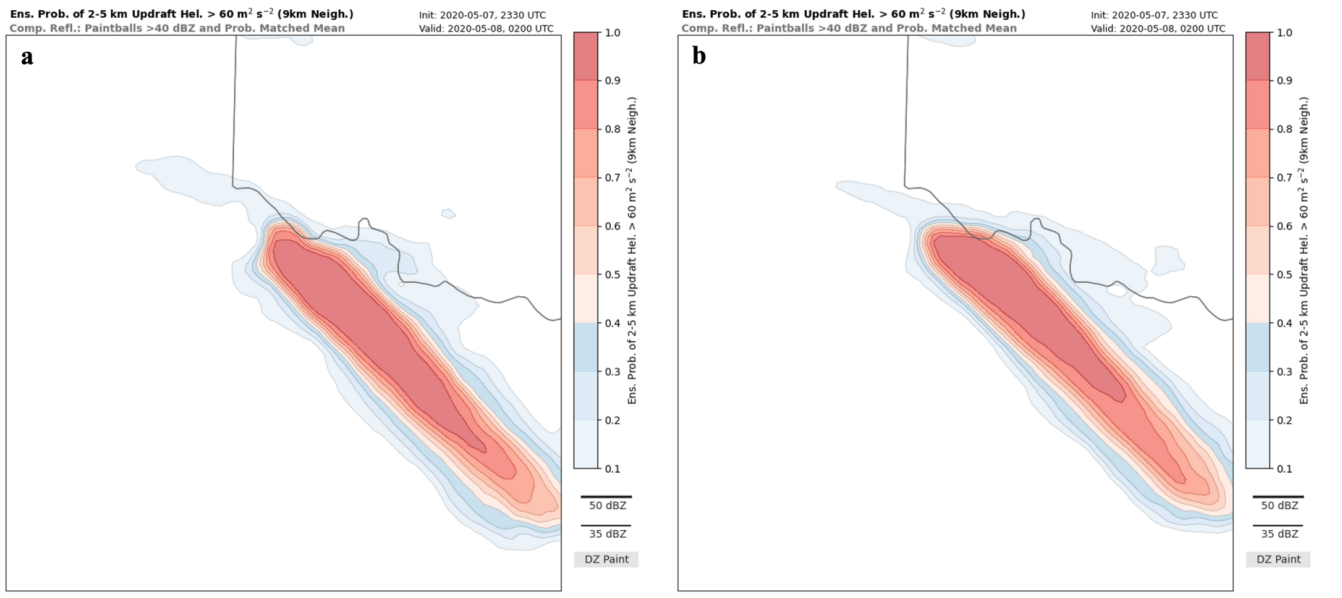

Figure 5.71: As in Figure 5.66, but for the 2330 UTC forecast.

Chapter 6

Discussion

Both the Multistatic and the WSR-88D Only experiments have their strengths and weaknesses, and large, consistent differences in quality are not observed in either. The Multistatic experiment tends to produce storms with higher reflectivity values than the WSR-88D Only experiment throughout the forecasts, but both predict maximum reflectivity values higher than the reflectivity values of the Truth Run (Figures 5.19-5.23). However, for the 2215 UTC ensemble analyses of the reflectivity the Multistatic members perform better than the WSR-88D Only members, with the Multistatic members having slightly larger and stronger storms that match the Truth Run better than the weaker storms in the WSR-88D Only experiment (Figures 5.8 and 5.37). The CCA supports this conclusion, with a majority of the Multistatic members having a higher correlation to the Truth Run. Additionally, the 2215 UTC forecast is the first forecast initialization when more than just zeros are assimilated from the multistatic network, allowing the multistatic network to have the first impacts on the WoFS ensemble analyses. These differences suggest that the assimilation of bistatic velocity observations from the multistatic network enables WoFS to spin-up storms quicker and more accurately.

A second analysis and forecast period where the Multistatic members perform better than the WSR-88D Only members is the 2300 UTC reflectivity forecast. While this forecast is not near the initiation of the storm and the storm has been spun-up in the model for several DA cycles at this point, this forecast does initialize as the storm is

beginning to split. The forecast at this time is complex, but the multistatic network produces a more accurate analysis of the storm and outperforms the WSR-88D Only experiment for the majority of members (Figures 5.12 and 5.40). This is supported both by subjective analysis of the 2300 UTC ensemble analyses, as well as the correlation between the Multistatic experiment and the Truth Run and the correlation between the WSR-88D Only experiment and the Truth Run.

While both the 2215 and 2300 UTC Multistatic MVV forecasts have a relatively poor correlation to the Truth Run, the poor correlation is driven by the resolution-based intensity differences between the simulations. The location of the updrafts are similar between the Truth Run and the Multistatic experiment, which is supported by difference plots showing only positive values and no displaced negative values for the 2215 UTC ensemble analyses for 16 of the 18 members (not shown). For the 2300 UTC MVV ensemble analyses, there are no displaced negative difference values between the Multistatic experiment and the Truth Run, so the Multistatic experiment is producing a good forecast of the location of the updraft. However, for the WSR-88D Only experiment, there are some displaced negative values near the main updraft between the WSR-88D Only experiment and the Truth Run. In addition to the differences in the 2215 and 2300 UTC forecasts, the Multistatic members tend to have higher MVV values than the WSR-88D Only members for the 2215 and 2230 UTC forecasts, which suggests that the Multistatic experiment is spinning up a stronger updraft quicker than the WSR-88D Only forecasts.

The remaining forecast times, 2230, 2245, and 2330 UTC, exhibit a majority of the WSR-88D Only members producing higher correlations to the Truth Run than the Multistatic members. However, subjectively looking at the 2230 UTC reflectivity forecast, the Multistatic members have a slightly stronger storm that more closely matches the Truth Run, but the overall differences are small (Figure 5.20). Similarly,

the 2245 UTC reflectivity forecast has stronger storms in the Multistatic members than in the WSR-88D Only members (Figure 5.21). The 2330 UTC forecast has a majority of the WSR-88D Only members with a higher correlation to the Truth Run, but subjectively the Multistatic experiment still produces stronger storms with a better shape on the right-split (Figure 5.54). Additionally, the WSR-88D Only members tend to have a weaker storm, with the core of highest reflectivity being displaced from the Truth Run. The lower correlation to the Truth Run in the Multistatic experiment is primarily driven by the Multistatic experiment inaccurately predicting the left-mover, where most members allow the left-mover to dissipate well before it dissipates in the Truth Run. Despite this, the Multistatic members more accurately predict the right-mover, which is the primary storm producing severe weather during this event.

In addition to reflectivity differences, the WSR-88D Only members tend to have stronger MVV values in the 2330 UTC ensemble analyses than the Multistatic members, but this difference is much smaller for the 2230 and 2245 UTC ensemble analyses, with the Multistatic members producing stronger MVV values than the WSR-88D Only experiment (Figures 5.26 and 5.58). During the 2230 UTC forecast, the Multistatic updrafts are more displaced from the Truth Run than the WSR-88D Only updrafts, but these differences are small and difficult to see from a subjective perspective. A similar story occurs for the 2245 UTC MVV forecast, where more Multistatic members are displaced from the Truth Run than in the WSR-88D Only experiment (Figures 5.27 and 5.59). Interestingly, for the 2330 UTC MVV ensemble analyses, more WSR-88D Only members have a displaced updraft than the Multistatic members (Figures 5.30 and 5.61). While neither experiment accurately analyzed the intensity of the MVV, it appears that the Multistatic experiment may have produced a slightly more accurate analysis of the updraft location at this time.

All of the previous discussion is further supported by the UH25 probability swath analysis for each forecast initialization. The 2215 UTC forecast, which is after the first multistatic network observations are assimilated, shows a more continuous UH25 probability swath for the Multistatic experiment, with probability values exceeding 0.8, while the WSR-88D Only experiment has two discontinuous swaths (Figure 5.67). However, it is important to note that both experiments produced accurate, high confidence forecasts of the right-mover track early after CI compared to expectations. From the 2215 UTC forecast onwards, both the Multistatic and WSR-88D Only experiments' UH track forecasts are good. For the 2215 UTC forecast, the WSR-88D Only experiment is slightly more confident in the track of the mesocyclone in the earlier portions of the forecast period, but the Multistatic experiment is more confident in the mesocyclone track throughout the remaining forecast.

Throughout the middle forecasts, 2230 and 2245 UTC, the Multistatic experiment consistently produces a continuous swath of high probability values, while the WSR-88D Only experiment still predicts more discontinuous swaths for the 2230 UTC forecast (Figure 5.68). Additionally, the Multistatic swath is displaced south of the WSR-88D Only experiment, demonstrating that the Multistatic experiment favors a more southerly track while the WSR-88D Only experiment favors a more northerly track. The northerly track of the WSR-88D Only experiment more closely matches the Truth Run in the early portions of the forecast. Additionally, the northerly track matches better at the end of the forecast as well, but the Multistatic UH swath matches the eastward extent of the storm better. The 2245 UTC forecast exhibits a probability difference between the Multistatic experiment and the WSR-88D Only experiment, with the WSR-88D Only experiment predicting lower probabilities of UH25 exceeding the 60 $m^2 s^{-2}$ threshold than the Multistatic experiment (Figure 5.69). Additionally,

the WSR-88D Only experiment is displaced slightly north of the Multistatic experiment and slightly east of the Multistatic experiment. At the beginning of the forecast, the northern displacement of the WSR-88D Only swath matches the Truth Run more closely, but the westward displacement of the Multistatic swath more closely matches the Truth Run. At the end of the forecast, the two experiments' swath are identically located south of the Truth Run, but the Multistatic swath extends further east than the WSR-88D Only experiment. Based on this, the WSR-88D Only experiment becomes less confident in storm track in the 2245 UTC forecast, while the Multistatic experiment remains highly confident in storm track. This difference is important because the WSR-88D Only experiment is more uncertain about the track of the right-mover following the split than the Multistatic experiment.

Probability swath displacement between the Multistatic experiment and the WSR-88D Only experiment continues in the later forecasts, 2300 and 2330 UTC. However, both experiments continue to predict that the storm will likely exceed the 60 m^2s^{-2} threshold. Both experiments show high probability for UH25 greater than 60 m^2s^{-2}. In the 2300 UTC forecast, the Multistatic experiment has a thinner swath of the highest probabilities, further suggesting that the Multistatic members are in more agreement on where the right-mover will track, while the WSR-88D Only experiment has a thicker swath of highest probabilities, indicating that the members are less confident on storm track (Figure 5.70). Both experiments have a probability swath that is displaced much further east than where the Truth Run shows the right-mover at the start of the 2300 UTC forecast. The WSR-88D Only swath is once again displaced to the north of the Multistatic swath in the early forecasts, which more accurately matches the Truth Run. However, at the middle portions of the forecast, near the end of the 0.9 probability, the Multistatic swath more closely matches the Truth Run. Therefore, both experiments accurately forecast the track of the storm at this time, despite the

initial displacement early in the forecast. The Multistatic UH swath is shifted further to the east at the beginning of the 2330 UTC forecast than the WSR-88D Only swath, but the WSR-88D Only swath more closely matches the initial location of the Truth Run (Figure 5.71). The WSR-88D Only swath is shifted slightly further north than the Multistatic experiment, but the difference does not impact the north/south location accuracy of the track. The Multistatic 0.9 probability swath extends further southeast than the WSR-88D Only swath and slightly matches the path of the Truth Run better than the WSR-88D Only swath, but the difference is likely only a few kilometers. Therefore, the WSR-88D Only swath is more accurate on the east/west placement early in the forecast, but the Multistatic is more accurate on the north/south placement later in the forecast. Both experiments accurately match the Truth Run's path, but the Multistatic is slightly better at the end of the forecast.

Based on the UH25 probability swath analysis, both experiments accurately predict the track of the right-moving supercell, even after only 2 assimilation cycles post CI. However, the Multistatic experiment is more confident in the storm track of the right-mover in every forecast. Specifically, for the forecasts where the Multistatic experiment performs better, 2215 and 2300 UTC, the assimilation of multistatic network observations results in the Multistatic members having a higher probability of exceeding the UH25 threshold, especially for later lead times. However, the Multistatic swath is displaced to the south of the Truth Run's path, but more closely matches the east/west extent of the swath at the end of the forecast. Therefore, the Multistatic experiment is too far south at the beginning and end of the forecast, but is confident in the path later into the forecast.

Similarly, the 2300 UTC analyses and forecast further supports that the Multistatic experiment more accurately predicts strength of the storm and where it will track. The 2300 UTC ensemble analyses of reflectivity show that the Multistatic experiment more

accurately analyzes the left-mover. The intensity of the left-mover is similar between the Multistatic experiment and WSR-88D Only experiment, but the Multistatic experiment has a larger expanse of the highest reflectivity in the left-mover than WSR-88D Only experiment. The larger expanse of the highest reflectivity in the left-mover more closely matches what the Truth Run shows at this time, but the difference is small between the two experiments (Figures 5.14 and 5.42). Additionally, the WSR-88D Only experiment does not accurately predict updraft location for the 2300 UTC forecast, evident by the eastward displacement of the right-mover updraft and the left-mover updraft's westward displacement from the Truth Run (Figure 5.65). The Multistatic experiment has a left-mover that located closer to the Truth Run's left-mover, and a right-mover that is displaced southeast of the Truth Run, which matches the UH analysis.

While the WSR-88D Only experiment produces higher CC in the remaining forecasts, this is primarily a result of the WSR-88D Only experiment more accurately predicting the left-mover. The reflectivity values were similar between the experiments during these forecasts, but the Multistatic experiment tended to have higher reflectivity than the WSR-88D Only experiment and more closely resembled the Truth Run when subjectively analyzing the two experiments. Additionally, the WSR-88D Only tends to produce UH probability swaths that are displaced to the north of the Multistatic experiment, which more closely matches the Truth Run, but the displacement is relatively small for all forecasts. Therefore, it appears that the Multistatic experiment produced slightly better forecasts and analyses throughout the experiment, especially during the 2215 and 2300 UTC forecasts, but the differences between the two experiments were small, such as a difference of only a few dBZ for reflectivity. However, the Multistatic experiment had significantly higher (5 ms^{-1} or more) MVV values than the WSR-88D Only experiment in the earlier initialization times, 2215 and 2230 UTC. This suggests

that while the differences between the two experiments are not large, the differences seem to indicate a positive impact from assimilating multistatic velocity observations.

Chapter 7

Conclusion

This project used Observing System Simulation Experiments to determine the impact of assimilating additional Doppler velocity observations from a network of bistatic radar receivers on forecasts by the Warn-On Forecast System. The OSSE looked at a splitting, hail-producing supercell that impacted northern Texas on 7 May 2020 and dropped significant severe hail throughout its life cycle. The Truth Run was created by downscaling WoFS Member 12 from the 2000 UTC forecast on 7 May 2020 from 3-km grid spacing to 250-m grid spacing. Two experiments were then conducted, one which assimilated Truth Run reflectivity and emulated bistatic velocity data from a 5-receiver multistatic network (Multistatic experiment) and the other which only assimilated emulated 88D radial velocity observations and Truth Run reflectivity (WSR-88D Only experiment). Reflectivity, maximum vertical velocity, and 2 to 5-km updraft helicity swaths were analyzed to determine the impacts of assimilating emulated multistatic network observations. Reflectivity and MVV analysis focused on the ensemble analyses, as this is when the largest impacts from the multistatic network occur as well as the subsequent forecasts. UH25 probability swaths were analyzed for the entire forecast, taking the image from the 0200 UTC time step to observe the multistatic network impacts during the time of the Truth Run.

The reflectivity analysis and forecasts were similar, but generally more accurate in the Multistatic experiment for all forecasts. The 2215 and 2300 UTC Multistatic forecasts most clearly outperform the WSR-88D Only forecasts based on correlation

coefficient analysis and subjective comparisons. Previous research shows that assimilating additional radar data near the time of storm initiation improved WoFS analysis of storms and its subsequent forecasts (Wheatley et al. 2015; Guerra et al. 2022). This holds true in this OSSE, as the 2215 UTC forecast is the first forecast with multistatic network velocity observations assimilated and produced more accurate reflectivity forecasts and a higher, continuous UH25 probability swath than either the previous forecast or the WSR-88D Only experiment. The MVV analysis shows that the Multistatic experiment and WSR-88D Only experiment were essentially identical in updraft location at this time, with both experiments showing minimal displacement from the Truth Run, but with subtly stronger MVV in the Multistatic experiment than the WSR-88D Only experiment, indicating a more rapid spin up of the storm updraft with assimilation of multistatic velocity observations.

For the 2300 UTC forecast, the Multistatic members and WSR-88D Only members produced analyses as the storm was beginning to split. The Multistatic experiment outperformed the WSR-88D Only experiment for all variables considered. The storm had been spun-up for several DA cycles by the time the 2300 UTC forecast initialized, allowing the assimilated multistatic network data to impact more than just storm spin-up. The MVV analysis showed that the WSR-88D Only experiment was not positioning the updraft as accurately as the Multistatic experiment (Figures 5.35 and 5.65), which was indicated by negative difference values appearing in several WSR-88D Only members and not in the corresponding Multistatic members (difference plots not shown). Additionally, the reflectivity in the WSR-88D Only members was weaker than those in the Multistatic members, with both experiments weaker than the Truth Run. Forecast improvement from assimilation of multistatic velocity observations is further supported in the UH25 probability swath analysis, where the Multistatic experiment predicted a

continuous, thinner, higher probability swath compared to the WSR-88D Only experiment. The Multistatic members had more agreement in predicted storm location given the thinner probability swath.

According to the correlation coefficient analysis, the WSR-88D Only experiment was more similar to the Truth Run for the remaining forecasts, but the subjective analysis and probability analysis do not support this apparent improvement. The Multistatic members continued to produce stronger reflectivity in the dominant storm than the WSR-88D Only members, and the probability swaths of the Multistatic experiment consistently produced a single, continuous, high probability swath along the path of the storm. Additionally, the Multistatic experiment was more confident in storm track than the WSR-88D Only experiment, with longer, thinner UH25 probability swaths (Figures 5.68-5.71), even though the Multistatic swath was displaced from the Truth Run. The MVV analysis showed that the WSR-88D Only members had stronger updrafts in the 2330 UTC ensemble analyses, but the difference in MVV values for the 2230 and 2245 UTC forecasts were small and the 2245 UTC forecasts showed that the Multistatic members were more displaced from the Truth Run updraft than the WSR-88D Only members (Figures 5.34 and 5.64). For the 2330 UTC forecast, the WSR-88D Only members are more displaced from the Truth Run updraft. The primary reason that the WSR-88D Only members produced higher CC values to the Truth Run than the Multistatic members did during the latter forecasts is that the WSR-88D Only members tended to maintain the left-mover in the domain, while the Multistatic experiment allowed the left-mover to dissipate well before it dissipated in the Truth Run. Therefore, even in the forecasts that the Multistatic experiment did not perform better than the WSR-88D Only experiment, based on correlation coefficients, the forecasts were similar. Assimilating observation from the multistatic network did not appear to degrade the forecasts, and the subjective analysis suggests

that the Multistatic experiment still performed slightly better in the 2230, 2245 and 2330 UTC forecasts. In general, the multistatic network improves the WoFS forecasts for the crucial times of 2215 UTC, when the storm was just beginning to appear in observations, and at 2300 UTC, when the storm was beginning to split. All other times were similar between the two experiments, with subtle potential improvements in the Multistatic experiment.

Future work may consider looking at a different WoFS experiment. The 7 May 2020 case is one of the best WoFS forecasts to date; therefore, no matter what data are added to this experiment it would be difficult to outperform an already excellent forecast. This may explain why the Multistatic and WSR-88D Only experiments were nearly identical at times, since the WSR-88D Only experiment is essentially the prediction of what WoFS Member 12 would have forecast that day. Therefore, it would be interesting to examine how a multistatic network impacts WoFS forecasts that perform more poorly than the 7 May 2020 forecast. Additionally, changing the multistatic network design may have yielded different results. In hindsight, it would have likely been beneficial to add additional receivers north of the storm, as most of them were placed south and along the storm's path, rather than slightly offset from the path. Different configurations of the multistatic network design may cause different impacts, as well as change the way the receivers are viewing the storm. In addition to different configurations and using a different case, there may be some benefit to assimilating data for an entire radar volume, rather than cutting off observations at 6.4°. This would provide a fuller view of the storm from the bistatic receivers, as well as potentially assimilate useful observations from higher up in the storm. A final avenue of future work revolves around the use of maximum vertical velocity, specifically that it might be more useful to use an area-based metric for updrafts or use averaging to get a 3 km average of the 250 m grid spacing maximum vertical velocity observations. Each of these factors

may change the overall results of the maximum vertical velocity analysis and provide a different explanation of what is occurring in the experiments.

Reference List

Byrd, A. D., R. D. Palmer, and C. J. Fulton, 2019: Development of a Low-Cost Multistatic Passive Weather Radar Network. *IEEE Transactions on Geoscience and Remote Sensing*, **58**, 2796–2808.

Coniglio, M. C., S. M. Hitchcock, and K. H. Knopfmeier, 2016: Impact of Assimilating Preconvective Upsonde Observations on Short-Term Forecasts of Convection Observed during MPEX. *Monthly Weather Review*, **144**, 4301–4325.

de Elía, R. and I. Zawadzki, 2001: Optimal Layout of a Bistatic Radar Network. *Journal of Atmospheric and Oceanic Technology*, **18**, 1184–1194.

Dowell, D. C., C. R. Alexander, E. P. James, S. S. Weygandt, S. G. Benjamin, G. S. Manikin, B. T. Blake, J. M. Brown, J. B. Olson, M. Hu, et al., 2022: The High-Resolution Rapid Refresh (HRRR): An Hourly Updating Convection-Allowing Forecast Model. Part 1: Motivation and System Description. *Weather and Forecasting*.

Emmerson, S., 2022: *Observations and Simulations of a Multistatic Weather Radar Network*. Master's thesis, School of Meteorology.

Guerra, J. E., P. S. Skinner, A. Clark, M. Flora, B. Matilla, K. Knopfmeier, and A. E. Reinhart, 2022: Quantification of NSSL Warn-On-Forecast System Accuracy by Storm Age Using Object-Based Verification. *Weather and Forecasting*.

Hitchcock, S. M., M. C. Coniglio, and K. H. Knopfmeier, 2016: Impact of MPEX Upsonde Observations on Ensemble Analyses and Forecasts of the 31 May 2013 Convective Event Over Oklahoma. *Monthly Weather Review*, **144**, 2889–2913.

Houtekamer, P. L. and F. Zhang, 2016: Review of the Ensemble Kalman Filter for Atmospheric Data Assimilation. *Monthly Weather Review*, **144**, 4489–4532.

Jones, T. A., K. Knopfmeier, D. Wheatley, G. Creager, P. Minnis, and R. Palikonda, 2016: Storm-Scale Data Assimilation and Ensemble Forecasting with the NSSL Experimental Warn-on-Forecast System. Part II: Combined Radar and Satellite Data Experiments. *Weather and Forecasting*, **31**, 297–327.

Jones, T. A., P. Skinner, N. Yussouf, K. Knopfmeier, A. Reinhart, X. Wang, K. Bedka, W. Smith Jr, and R. Palikonda, 2020: Assimilation of GOES-16 Radiances and Retrievals into the Warn-on-Forecast System. *Monthly Weather Review*, **148**, 1829–1859.

Kain, J. S., S. J. Weiss, D. R. Bright, M. E. Baldwin, J. J. Levit, G. W. Carbin, C. S. Schwartz, M. L. Weisman, K. K. Droegemeier, D. B. Weber, et al., 2008: Some

Practical Considerations Regarding Horizontal Resolution in the First Generation of Operational Convection-Allowing NWP. *Weather and Forecasting*, **23**, 931–952.

Kerr, C. A., L. J. Wicker, and P. S. Skinner, 2021: Updraft-Based Adaptive Assimilation of Radial Velocity Observations in a Warn-on-Forecast System. *Weather and Forecasting*, **36**, 21–37.

Kleist, D. T., D. F. Parrish, J. C. Derber, R. Treadon, W.-S. Wu, and S. Lord, 2009: Introduction of the GSI into the NCEP Global Data Assimilation System. *Weather and Forecasting*, **24**, 1691–1705.

Potvin, C. K. and L. J. Wicker, 2013: Assessing Ensemble Forecasts of Low-Level Supercell Rotation within an OSSE Framework. *Weather and forecasting*, **28**, 940–960.

Potvin, C. K., L. J. Wicker, and A. Shapiro, 2012: Assessing Errors in Variational Dual-Doppler Wind Syntheses of Supercell Thunderstorms Observed by Storm-Scale Mobile Radars. *Journal of Atmospheric and Oceanic Technology*, **29**, 1009–1025.

Roberts, B., I. L. Jirak, A. J. Clark, S. J. Weiss, and J. S. Kain, 2019: PostProcessing and Visualization Techniques for Convection-Allowing Ensembles. *Bulletin of the American Meteorological Society*, **100**, 1245–1258.

Schwartz, C. S. and R. A. Sobash, 2017: Generating Probabilistic Forecasts from Convection-Allowing Ensembles Using Neighborhood Approaches: A Review and Recommendations. *Monthly Weather Review*, **145**, 3397–3418.

Skinner, P. S., D. M. Wheatley, K. H. Knopfmeier, A. E. Reinhart, J. J. Choate, T. A. Jones, G. J. Creager, D. C. Dowell, C. R. Alexander, T. T. Ladwig, et al., 2018: Object-Based Verification of a Prototype Warn-on-Forecast System. *Weather and forecasting*, **33**, 1225–1250.

Snyder, C. and F. Zhang, 2003: Assimilation of Simulated Doppler Radar Observations with an Ensemble Kalman Filter. *Monthly Weather Review*, **131**, 1663–1677.

Stensrud, D. J., L. J. Wicker, M. Xue, D. T. Dawson II, N. Yussouf, D. M. Wheatley, T. E. Thompson, N. A. Snook, T. M. Smith, A. D. Schenkman, et al., 2013: Progress and challenges with Warn-on-Forecast. *Atmospheric Research*, **123**, 2–16.

Stensrud, D. J., M. Xue, L. J. Wicker, K. E. Kelleher, M. P. Foster, J. T. Schaefer, R. S. Schneider, S. G. Benjamin, S. S. Weygandt, J. T. Ferree, et al., 2009: Convective-Scale Warn-on-Forecast System: A Vision for 2020. *Bulletin of the American Meteorological Society*, **90**, 1487–1500.

Stratman, D. R., N. Yussouf, Y. Jung, T. A. Supinie, M. Xue, P. S. Skinner, and B. J. Putnam, 2020: Optimal Temporal Frequency of NSSL Phased Array Radar Observations for an Experimental Warn-on-Forecast System. *Weather and Forecasting*, **35**, 193–214.

Tong, M. and M. Xue, 2005: Ensemble Kalman Filter Assimilation of Doppler Radar Data with a Compressible Nonhydrostatic Model: OSS Experiments. *Monthly Weather Review*, **133**, 1789–1807.

Wheatley, D. M., K. H. Knopfmeier, T. A. Jones, and G. J. Creager, 2015: Storm-Scale Data Assimilation and Ensemble Forecasting with the NSSL Experimental Warn-on-Forecast System. Part I: Radar Data Experiments. *Weather and Forecasting*, **30**, 1795–1817.

Wurman, J., 1994: Vector Winds from a Single-Transmitter Bistatic Dual-Doppler Radar Network. *Bulletin of the American Meteorological Society*, 983–994.

Wurman, J., S. Heckman, and D. Boccippio, 1993: A Bistatic Multiple-Doppler Radar Network. *Journal of Applied Meteorology and Climatology*, **32**, 1802–1814.

Yussouf, N. and D. J. Stensrud, 2010: Impact of Phased-Array Radar Observations over a Short Assimilation Period: Observing System Simulation Experiments Using an Ensemble Kalman Filter. *Monthly weather review*, **138**, 517–538.